TESIS

Para la obtención del grado de

DOCTOR DE LA UNIVERSIDAD DEL VALLE

Posgrados en Ciencias Química

Facultad de Ciencias Naturales y Exactas

Presentada por :

Cristian David Miranda Muñoz

****

Heterogeneous acid catalysts in the etherification of glycerol with *tert*-butyl alcohol and *iso*amyl alcohol

****

Directores de Tesis

Yannick POUILLOUX y Julian URRESTA

Santiago de Cali, 2019.

THESE

Pour l'obtention du grade de

DOCTEUR DE L'UNIVERSITE DE POITIERS

Faculté des Sciences Fondamentales et Appliquées
(Diplôme National - Arrêté du 7 août 2006)

Ecole Doctorale : Gay Lussac, Sciences pour l'environement

Secteur de Recherche : Chimie Organique, Minérale, Industrielle

Présentée par :

Cristian David Miranda Muñoz

****

Heterogeneous acid catalysts in the etherification of glycerol with *tert*-butyl alcohol and *iso*amyl alcohol

****

Directeur(s) de Thèse:

Yannick POUILLOUX et Julian URRESTA

Poitiers, 2019

Resumen

Se evaluaron diferentes sólidos ácidos heterogéneos basados en zeolitas y óxidos de grafeno sulfonados como catalizadores en la eterificación de glicerol con alcohol *terc*-butílico. Las zeolitas utilizadas en este estudio, tales como mordenita, faujasita, beta y H-ZSM5, se compararon para estudiar el efecto de la estructura y el tamaño de los poros, así como el tamaño del cristal en la conversión de glicerol y selectividad hacia di y tri *terc*-butil éteres de glicerol. Los resultados empleando zeolitas, mostraron que en una reacción en fase líquida sensible a las limitaciones de la difusión, la red porosa de la zeolita no es suficiente para predecir la actividad, selectividad y la estabilidad; se debe tener en cuenta la accesibilidad al poro de acuerdo a su volumen interno. Las zeolitas *BEA y MFI tienen volúmenes de poros similares, pero la diferencia en la apertura de poros (mayor que 1 Å), es suficiente para generar fuertes limitaciones de difusión en el caso de la zeolita de poros medios. La actividad de la zeolita *H-BEA es proporcional a la concentración del sitio ácido de Brønsted siempre que el tamaño de los cristales sea inferior a 100 nm (sin limitación de la difusión interna). En el caso de faujasita con supercajas, se prefiere la eterificación sucesiva.

En la segunda serie de catalizadores, el óxido de grafeno reducido, se obtuvo mediante el método Hummers modificado y su posterior reducción por tres vías diferentes: i) hidracina, ii) Zn/HCl y iii) ácido ascórbico. El óxido de grafeno reducido presenta una relación C/O diferente en la superficie. Finalmente, estos últimos sólidos se funcionalizaron utilizando ácido sulfanílico, generando nuevos sitios de ácido Brønsted. Las pruebas catalíticas han demostrado que, independientemente del óxido de grafeno, la conversión de glicerol es mayor que la obtenida con Amberlyst® (A-15), que es el catalizador de referencia para esta reacción. La selectividad después de 10 horas de reacción también es comparable a la de A-15. Este estudio ha demostrado que el control del equilibrio hidrofílico/lipofílico es muy importante porque depende de la cantidad de grupos oxigenados en la superficie.

Respecto al mecanismo de reacción, resultó ser diferente en ambos casos, favoreciendo a Eley-Rideal (ER) en la reacción con zeolitas, mientras que, en el caso de los óxidos de grafeno, un mecanismo de tipo Langmuir-Hinshelwood (LH) es predominante.

Finalmente, la zeolita Beta, Amberlyst® 15 y el óxido de grafeno sulfonado se han evaluado como catalizadores en la eterificación de glicerol con alcohol *iso*amílico. Los resultados muestran que la activación del alcohol primario es más difícil en las condiciones "moderadas" de la reacción estudiadas que con la del alcohol *terc*-butílico. Por otro lado, se ha encontrado que la auto-eterificación del alcohol *iso*amílico (para formar *iso*amil-éter) es favorecida sobre la eterificación del glicerol.

Résumé

Différents solides acides hétérogènes à base de zéolithes et d'oxydes de graphène sulfonés ont été évalués en tant que catalyseurs dans l'éthérification du glycérol avec de l'alcool *tert*-butylique. Les zeolites utilisés dans cette étude telle que la mordénite, la faujasite, le bêta et l'H-ZSM5, ont été comparés afin d'étudier l'effet de la structure et de la taille des pores ainsi que la taille des cristaux sur la conversion du glycérol et la sélectivité en di et tri-*tert*-butyle éthers du glycérol. Les résultats ont montré que, dans une réaction en phase liquide sensible aux limitations diffusionnelles, le réseau poreux de la zéolite n'est pas suffisant pour prédire l'activité, la sélectivité et la stabilité, l'accessibilité au volume interne doit être prise en compte. Les zéolithes *BEA et MFI présentent les volumes poreux similaires mais la différence d'ouverture de pores (supérieure à 1 Å) est suffisante pour générer de fortes limitations diffusionnelles dans le cas de la zéolite à pores moyens. L'activité de la zéolithe *HBEA est proportionnelle à la concentration en site acide de Brønsted à condition que la taille des cristaux soit inférieure à 100 nm (absence de limitation de diffusion interne). Dans le cas de la faujasite présentant des supercages, une éthérification successive est privilégiée.

Dans la deuxième série de catalyseurs, l'oxyde de graphène a été obtenu par la méthode d'Hummers modifiée puis grâce à une réduction ultérieure effectuée par trois voies différentes: i) hydrazine, ii) Zn/HCl et iii) acide ascorbique, l'oxyde de graphène présente un rapport C/O différent à la surface. Enfin, ces derniers solides ont été fonctionnalisés à l'aide d'acide sulfanilique, générant de nouveaux sites acides de Brønsted. Les tests catalytiques ont montré que, quel que soit l'oxyde de graphène, la conversion du glycérol est supérieure à celle obtenue avec l'Amberlyst® (A-15), qui est le catalyseur de référence pour cette réaction. La sélectivité après 10 heures de réaction est également comparable à celle de l'A-15. Cette étude a montré que le contrôle de la balance hydrophile/lipophile est très importante est qu'elle est dépendante du nombre de groupes oxygénés en surface.

En ce qui concerne le mécanisme réactionnel, il s'est avéré qu'il était différent dans les deux cas, Eley-Rideal (ER) étant celui qui est favorisé dans la réaction avec les zéolithes, alors que

dans le cas des oxydes de graphène, c'est un mécanisme de type Langmuir-Hinshelwood (LH) qui est prépondérant.

Enfin, la zéolite Beta, Amberlyst® 15 et l'oxyde de graphène sulfoné ont été évalués en tant que catalyseurs dans l'éthérification du glycérol avec de l'alcool isoamylique, mais les premiers résultats montrent que l'activation de l'alcool primaire est difficile dans les conditions "modérées" de la réaction. En revanche, il a été trouvé que l'auto-éthérification de l'alcool isoamylique (pour former de l'éther *iso*amylique) est favorisée par rapport à celle du glycérol.

Abstract

Different heterogeneous acid solids based on zeolites and sulfonated graphene oxides have been evaluated as catalysts in the etherification of glycerol with *tert*-butyl alcohol. The zeolites used in this study, such as mordenite, faujasite, beta and H-ZSM5, were compared to study the effect of pore structure and size, as well as the size of the crystal in the conversion of glycerol and the selectivity towards the di and tri-*tert*-butyl ether of glycerol. The results showed that, in a liquid phase reaction sensitive to diffusion limitations, the porous zeolite network is not sufficient to predict activity, selectivity and stability; The accessibility to the pore must be taken into account according to its internal volume. The zeolites *BEA and MFI have similar pore volumes, but the difference in the opening of the pores (more than 1 Å) is sufficient to generate strong diffusion limitations in the case of the medium pore zeolite. The activity of the zeolite * H-BEA is proportional to the concentration of the Brønsted acid site as long as the size of the crystals is less than 100 nm (without limitation of internal diffusion). In the case of faujasite with supercages, successive etherification is preferred.

In the second series of catalysts, the graphene oxide was obtained by the modified Hummers method and its subsequent reduction by three different routes: i) hydrazine, ii) Zn/HCl and iii) ascorbic acid. Graphene oxide has a different C/O ratio at the surface. Finally, these last solids were functionalized using sulfanilic acid, generating new Brønsted acid sites. Catalytic tests have shown that, regardless of the graphene oxide, the conversion of glycerol is greater than that obtained with Amberlyst® (A-15), which is the reference catalyst for this reaction. The selectivity after 10 hours of reaction is also comparable to that of A-15. This study has shown that the control of the hydrophilic/lipophilic balance is very important because it depends on the amount of oxygenated groups on the surface.

Regarding the mechanism of reaction, it turned out to be different in both cases, favoring Eley-Rideal (ER) in the reaction with zeolites, whereas, in the case of graphene oxides, a mechanism of type Langmuir-Hinshelwood (LH) predominates.

Finally, zeolite Beta, Amberlyst® 15 and sulfonated graphene oxide have been evaluated as catalysts in the etherification of glycerol with isoamyl alcohol. The results show that the activation of the primary alcohol is more difficult in the "moderate" conditions of the reaction studied than with that of *tert*-butyl alcohol. On the other hand, it has been found that the self-etherification of isoamyl alcohol (to form isoamyl ether) favors the etherification of glycerol.

Acknowledgements

Hellen Keller said: "I have been given so much that I do not have time to reflect on what has been denied me".

There are many wonderful people and events that in one way or another are related to the preparation of this document that is the result of many years of preparation. First of all, I would like to begin by thanking my directors Julian Urresta and Yannick Pouillox, who trusted me and allowed me to learn a little more about the scientific world from their great experience.

Those who do not appear on the paper as official directors, but who in fact consider them my other directors for all the academic help and the great admiration aroused by their professional and personal qualities, are Ludovic Pinard, Pierrick Gaudin and Alexander Sachse. Thanks to your help and advice I have managed to get here!

To all the technical-administrative staff of the University of Poitiers, thank you very much, especially to Jean-Do for your kindness and to Stéphane Pronier (Mr. Bravo) for the pleasant moments while doing the microscopy of the catalysts.

The acknowledgments of moral support are dedicated to my other director, the same person as always: Alfonso Ramírez, who encouraged me and motivated me to continue on this route. To Luis A. Vargas, who with his way of being and his advice has made me learn about the way of life.

A thank you to my colleagues of university education, who in one way or another gave me their friendship in Poitiers and Cali. You can all count on my friendship.

To my parents and my brothers, who are always with me and they are the ones who motivate me and encourage me to keep improving day after day. For you it is this achievement! To the rest of family and friends that are many.

Table of content

Chapter 1: Etherification of glycerol with alcohols

1. Glycerol 7

1.1. Importance of glycerol 7
1.2. Problem of glycerol over-production 8

2. Etherification of glycerol with alcohols 10

3. Catalytic etherification of glycerol with *tert*-butanol 13

4. Acid catalysts for the etherification of glycerol with *tert*-butyl alcohol 15

References 19

1. Fundamentals of the most common characterization techniques of zeolites and carbocatalysts 25

1.1. X-ray diffraction, XRD 26
1.2. Adsorption- desorption of N_2 27
1.2.1. Isotherm classification 28
1.2.2. Specific Surface – BET surface 29
1.2.3. Pore volume 30
1.3. Scanning electron microscopy, SEM 32
1.4. Transmission electron microscopy, TEM 32
1.5. X fluorescence spectrometry, XRF 32
1.6. Inductively coupled plasma, ICP 34
1.7. Solid state nuclear magnetic resonance ^{27}Al, NMR 34
1.8. IR (TOT band) infrared spectroscopy band structure 35
1.9. Thermodesorption of pyridine at 423 K followed by IR 37
1.10. Raman spectroscopy, RAMAN 37
1.11. X-ray photoelectron spectroscopy, XPS 38
1.12. Elemental analysis, EA 39
1.13. Boehm titration 40
1.14. Thermogravimetric analysis, TGA 40

References 41

1. Zeolites 45

1.1. Structure 46
1.2. Acidity 49
1.2.1. Nature of the acid sites 49
1.2.2. Acid sites density 50
1.2.3. Acid sites strength 51
1.2.3.1. Ionic exchange degree 51
1.2.3.2. [T-O-T] bond angle 51

1.2.3.3. Metallosilicates 52
1.2.3.4. Electrostatic environment 52
1.2.3.5. Interaction with Lewis sites 52
1.2.4. Location of the acid sites 53
1.3. Shape selectivity 53
1.3.1. Reactant shape selectivity 53
1.3.2. Transition state shape selectivity 54
1.3.3. Product shape selectivity 54
1.4. Synthesis of zeolites 55
1.4.1. Silicon source 56
1.4.2. Aluminum source 56
1.4.3. Mineralizing agent 56
1.4.4. Structure directing agents (SDA) 56
1.5. Synthesis of hierarchical zeolites 58
1.5.1. Dealumination 60
1.5.2. Desilication 61
1.6. Zeolites in nanocrystals and their synthesis 63
1.6.2. Synthesis from strongly alkaline gels 64
1.6.3. Alternative methods 65

2. Zeolites as catalysts in the etherification of glycerol with *tert*-butyl alcohol 65

5.1. Chemicals and catalysts 67
5.2. Characterization 69
5.2.1. Chemical composition 69
5.2.2. Composition of the surface 69
5.2.3. Determination of the Si/Al ratio of the zeolite framework 70
5.2.4. Determination of the framework formula 71
5.2.5. Structural analysis 72
5.2.6. Morphology 73
5.2.7. Textural properties 73
5.2.8. Acidity 73
5.3. Glycerol etherification with *tert*-butyl alcohol 75
5.3.1. Catalyst regeneration and catalytic recycling 76
6.1. Characterization of catalysts 77
6.1.1. Chemical composition and Si/Al ratio 77
6.1.2. Structural results of zeolites 78
6.1.3. Morphology of the zeolites 80
6.1.4. Textural results of zeolites 83
6.1.5. Acidity of the catalysts 86
6.2. Glycerol etherification with *tert*-butyl alcohol 89
6.2.1. Thermodynamic analysis of reaction equilibrium 89
6.2.2. Kinetic model 91

6.2.3. Activity and stability 93
6.2.4. Selectivity 98
6.2.5. Regeneration 101
7. Conclusion 103
References 104
1. The carbon 117
1.1. Allotropic forms of carbon 118
2. Graphene 120
2.1. Methods of obtaining graphene 123
2.1.1. Obtaining graphene from graphite oxide 125
2.1.2. Chemical reduction of graphene oxide 127
2.1.3. Functionalization of graphene oxide and reduced graphene oxide 128
3. Graphene oxide as a catalyst 129
4. Motivation of the study of graphene oxide in the etherification of glycerol with tert-butyl alcohol 131
5. Objective of the use of graphene oxide in the etherification of glycerol with *tert*-butyl alcohol 132
6. Experimental section 132
6.1. Chemical and catalysts 132
6.2. Characterization 135
6.2.1. Textural properties 135
6.2.2. Chemical composition 136
6.2.3. Acid properties 136
6.3. Etherification of glycerol with *tert*-butyl alcohol and analysis 137
7. Results and discussion 137
7.1. Characterization of catalysts 137
7.1.1. Textural properties 137
7.1.2. Elemental Analysis 143
7.1.3. Acid properties 147
7.2. Etherification of glycerol with *tert*-butyl alcohol 148
7.2.1. Kinetic model 148
7.2.2. Activity 149
7.2.3. Selectivity 152
7.2.4. Stability 153
8. Conclusion 156
References 157

1. Fusel oil 169
2. Etherification of glycerol with *iso*amyl alcohol 169
3. Etherification of *iso*amyl alcohol 170
References 173
General Conclusions 175
Perspectives 178
Annex A 179
Annex B 185
Annex C 188

List of Figures

Chapter 1

Figure I. 1. Glycerol molecule. 7
Figure I. 2. Percentage of glycerol uses. 8
Figure I. 3. Glycerin production and price of refined and crude glycerin.[5] 9
Figure I. 4. Routes of chemical transformation of glycerol [9]. 9
Figure I. 5. Reaction of etherification of glycerol with *tert*-butyl alcohol. 14
Figure I. 6. Proposed mechanism of glycerol etherification with *tert*-butyl alcohol in the Brønsted acid sites. 15

Chapter 2

Figure II. 1.Types of physisorption isotherms. [36] 28

Chapter 3

Figure III. 1 Negative charge induced by the AlO_4^- tetrahedron in the structure, neutralized by a compensating cation (M^+). 47
Figure III. 2 Tetrahedra arrangement, forming the sodalite (or β-cage) and, finally, the structure of some zeolites, showing the three-dimensional channel network.[19] 48
Figure III. 3 Brønsted acid formation in the zeolites. [29] 50
Figure III. 4 Representation of reactant shape selectivity. 54
Figure III. 5 Representation of the transition state shape selectivity. 54
Figure III. 6 Representation of the product shape selectivity 54
Figure III. 7 Diagram of the crystallization process of a zeolite. [56] 58
Figure III. 8 An overview of the various synthesis routes towards zeolite materials combining micro- and mesopores. [62] 59
Figure III. 9 Hierarchical classification and typical pore distribution of zeolites. [66] 60
Figure III. 10 Mechanism of dealumination hydrochloric acid. [2] 61
Figure III. 11 Hydrolysis of framework Si in alkaline medium. [72] 61
Figure III. 12 Diagram of the influence of the content of Al in the treatment of desilication by treatment with NaOH. [62] 62

Figure III. 13 Different properties of nanometric zeolites. [78] 64
Figure III. 14. Structures of the zeolites studied. 67
Figure III. 15 Structural bands of * BEA zeolite 71
Figure III. 16 Molar extinction coefficient of Brønsted acid sites (band at 1545 cm^{-1}) and Lewis acid sites (1455 cm^{-1}). 74
Figure III. 17 Reactor used for etherification of glycerol with *tert*-butyl alcohol reaction. .. 75
Figure III. 18 X-ray diffractograms for synthesized or modified zeolites. 79
Figure III. 19 Scanning electron microscopy and transmission electronic images of commercial, modified and synthesized zeolites. 82
Figure III. 20 Isotherms of adsorption and nitrogen desorption for the zeolites synthesized and/or modified: a. MOR; b. *BEA and c. MFI zeolites. 84
Figure III. 21 Micropore (a) and mesopore (b) volumes as a function of zeolite crystal size. 86
Figure III. 22 Proportion of theoretical Brønsted acid site probed by pyridine at 423 K as a function of zeolite crystal size. 88
Figure III. 23 Correlation between EFAL and the Lewis acidity 89
Figure III. 24 (a) Conversion normalized by the conversion achieved at 1200 rpm and (b) Selectivity of MTBG and DTBG as function of the stirring rate on (***BEA**)**NC12.5**. 91
Figure III. 25 Natural logarithm of initial rates ($\ln r_0$) as a function of natural logarithm of the initial concentration ($ln[X]_0$) of glycerol (full symbols) and TBA (open symbols). Kinetic study carried out on (***BEA**)**NC12.5** at 363 K (data is given as absolute values). 92
Figure III. 26 Glycerol conversion as a function of reaction time. Test carried out at 363 K, 1200 rpm, autogenous pressure, 7,5 % of catalyst (referred to glycerol mass) and glycerol/*tert*-butyl alcohol molar ratio of 0.25. 93
Figure III. 27 Initial activity of glycerol etherification with *tert*-butyl alcohol as a function of the concentration of protonic sites probed by pyridine at 423 K. (operating conditions: glycerol/*tert*-butyl alcohol molar ratio = 0.25, T = 363 K). 96

Figure III. 28 Effectiveness factor (***η***) in etherification of glycerol with *tert*-butyl alcohol as a function of the zeolite beta crystal size (operating conditions: glycerol/*tert*-butyl alcohol molar ratio = 0.25, T = 363 K). 98
Figure III. 29 Typical chromatogram for the etherification of glycerol with *tert*-butyl alcohol; M1: 3-*tert*-butoxy-1,2 propanediol, M2: 2-*tert*-butoxy-1,3 propanediol, D1: 1,3-di-*tert*-butoxy-2-propanol, D2: 2,3-di-*tert*-butoxy-1-propanol, T: tri-*tert*-butoxy-propane, IB: isobutylene. *n*-butanol as internal standard. 99
Figure III. 30 Molar yields into MTBG, DTBG and TTBG as a function of glycerol conversion. 99
Figure III. 31 Recovered activity after washing with ethanol and calcination (823 K/6 h) of the deactivated catalysts. 101
Figure III. 32 FT-IR spectra of: fresh and spent (after rinsing with ethanol) zeolite (**FAU**)**SC40**. 102

Chapter 4

Figure IV. 1 Hybridization of carbon orbitals. 118
Figure IV. 2 Allotropes of carbon with graphene as a building block for all other allotropes [10]. 121
Figure IV. 3 Classification grid for the categorization of different graphene types according to three fundamental properties: number of graphene layers, average lateral dimension, and atomic carbon/oxygen ratio. 123
Figure IV. 4 The oxidation of graphite and the exfoliation of graphite oxide to obtain graphene oxide [54]. 126
Figure IV. 5 A proposed schematic (Lerf–Klinowski model) of graphene oxide structure [56] 126
Figure IV. 6 Representation of obtaining graphene oxide from graphite. 132
Figure IV. 7 Representation of obtaining reduced graphene oxide. 133
Figure IV. 8 Representation of obtaining sulfonated reduced graphene oxide. 134

Figure IV. 9 XRD patterns of Graphite, preoxidated graphite, (GO), (GO)R_A, (GO)R_H and (GO)R_Z-S. 139
Figure IV. 10 Raman spectra of graphite, (GO), (GO)R_H and (GO)R_A. 141
Figure IV. 11 SEM images of: a) graphite; b) (GO), c) (GO)R_A; d) (GO)R_A-S..... 142
Figure IV. 12 Transmission electronic images of the samples and EDS mapping showing the spatial distribution of C and S of (GO)R_H-S and (GO)R_A-S. 143
Figure IV. 13 The C/O and S/C ratios of reduced and sulfonated graphene oxide, respectively. 144
Figure IV. 14 XPS spectra for: a) graphite; b) pre-oxidized graphite; c) (GO); d) (GO)R_H; e) (GO)R_A; f) (GO)R_Z-S..... 146
Figure IV. 15 Atomic concentration (%) determined by XPS of graphite, pre-oxidized graphite, (GO), (GO)R_H, (GO)R_A and (GO)R_Z-S. 146
Figure IV. 16 Kinetical study of (AC)-S, a) and (GO)R_A-S, b)..... 149
Figure IV. 17 Glycerol conversion as a function of reaction time. (AC)-S, (AC)R_H-S and Amberlyst®15, a); Catalysts based on (GO), b). Test carried out at 363 K, 1200 rpm, autogenous pressure, 7,5 % of catalyst (referred to glycerol mass) and glycerol/*tert*-butyl alcohol molar ratio of 0.25..... 151
Figure IV. 18 Molar yields into MTBG, DTBG and TTBG as a function of glycerol conversion for catalyst based on sulfonated reduced (GO), compared to A-15 and (AC)-S. 153
Figure IV. 19 Results of recycling experiments for (GO)R_A-S, a) and (CA)-S, b). 154
Figure IV. 20 TGA pattern of (GO)R_A-S, (GO) and A-15. 155

List of Tables

Chapter 1

Table I. 1. Etherification of glycerol with *tert*-butyl alcohol using Amberlyst® 15 as a catalyst..... 16

Chapter 2

Table II. 1.Information obtained from each characterization technique useful for zeolites and carbocatalysts. 25

Chapter 3

Table III. 1 Summary of the advantages and disadvantages of the destructive and constructive synthesis approaches for mesoporous zeolite materials [62]. 63
Table III. 2 Catalysts used and their origin where C: commercial, S: synthetized, M: modified. 68
Table III. 3 Analysis conditions of NMR spectra[107]. 70
Table III. 4 Si/Al ratio, frame and aluminum Extra-framework..... 77
Table III. 5 Crystal sizes of the zeolites. 81
Table III. 6 Textural properties of Amberlyst® 15, alumina, silica, alumina-silica and zeolites (commercial, modified and synthetized): MOR, FAU, *BEA and MFI..... 85
Table III. 7 Acidic properties of Amberlyst® 15, alumina, silica, alumina-silica and zeolites (commercial, modified and synthetized): MOR, FAU, *BEA and MFI. 87
Table III. 8 Thermodynamic data. 90
Table III. 9 Glycerol etherification with *tert*-butyl alcohol: conversion and selectivity after 10 h, initial activity (A_0) and TOF obtained on Amberlyst® 15, silica, alumina, silica-alumina and zeolites (commercial and synthetized): MOR, FAU, *BEA and MFI..... 95
Table III. 10 Selectivity of glycerol monoethers (MTBG), glycerol diethers (DTBG) and glycerol triether (TTBG) at isoconversion. ($X \approx 20$ %) obtained on MOR, FAU, *BEA and MFI catalysts. 100

Chapter 4

Table IV. 1 Reducing agents for graphene oxide towards chemically reduced graphene oxide 127
Table IV. 2 Textural properties of Amberlyst® 15 (A-15), graphene oxide and sulfonated reduced graphene oxide. 137
Table IV. 3 Elemental analysis of activated carbon, graphene oxide and sulfonated reduced graphene oxide. 143
Table IV. 4 Acidic properties of activated carbon, Amberlyst® 15 (A-15), graphene oxide and sulfonated reduced graphene oxide. 148
Table IV. 5 Glycerol etherification with *tert*-butyl alcohol: conversion and selectivity after 10 h, initial activity (A^0) and TOF obtained on Amberlyst-15, activated carbon, graphene oxide and sulfonated reduced graphene oxide. 151

Chapter 5

Table V. 1 Identification of GIAE in the reactions with Amberlyst® 15, sulfonated reduced graphene oxide and beta zeolite as catalysts 170
Table V. 2 Isoamyl alcohol conversion using Amberlyst® 15, sulfonated reduced graphene oxide and beta zeolite as catalysts 171

General Introduction

Given the imminent need to look for alternative fuels to fossil fuels, the interest and use of methyl ethers of fatty acids (biodiesel) has increased exponentially in recent years. The increase in the production of biodiesel, has resulted in an increase also in the production of glycerol, which is a byproduct of the process, by carrying out the transesterification of vegetable oils with methanol. Although glycerol is a molecule with a wide range of different uses, and which in turn can be the precursor of other molecules of industrial and pharmaceutical importance, this market is constant and there is more and more glycerol than its global demand. For this reason, glycerol has practically become a waste. In this sense, different alternatives of new uses have been proposed, among them the obtaining of glycerol alkyl ethers, which have found their main application as fuel octane potentializers, better known as oxygenated additives. These glycerol alkyl ethers can be obtained by the reaction of etherification of glycerol with short chain aliphatic alcohols in the presence of acid catalysts. The valorization of glycerol towards these additives has been studied for less than a decade, which is why it is considered a potential field for exploration by catalysis.

Within the studies on the subject, heterogeneous type acid catalysts can be found, such as sulphonic resins and zeolites, standing out mainly Amberlyst® 15 and zeolite beta respectively. In this sense, it was considered appropriate to focus this study on three main aspects: i) the valorization of glycerol through the etherification of glycerol with tert-butyl alcohol and with isoamyl alcohol, ii) extend the study of zeolites, through the evaluation of Mordenite, Faujasite, Beta and H-ZSM-5 in different crystal sizes and iii) explore for the first time the use of sulfonated graphene oxide as a catalyst in this reaction.

This document is structured in 5 chapters, where the first includes the generalities of glycerol and the most important aspects of the etherification reaction with alcohols. The second chapter compiles the most important characterization techniques for the heterogeneous acid catalysts used in this study. Chapter 3 presents the results of the use of zeolites in the etherification of glycerol with tert-butyl alcohol, while chapter 4 shows the

results of the same reaction using the sulfonated graphene oxides. Finally, Chapter 5 shows the preliminary results of the etherification of glycerol with isoamyl alcohol.

Chapter 1:

Etherification of glycerol with alcohols

1. Glycerol

Glycerol, also known as glycerin or 1,2,3-propanetriol, is an alcoholic compound with three hydroxyl groups, Figure I.1. The word glycerol comes from the Greek *Glykos*, which means sweet. It has a viscous liquid appearance, has no color, but has a characteristic smell, as well as a sugary taste. In addition, glycerol is a hygroscopic compound and is in the liquid state at room temperature (273 K).

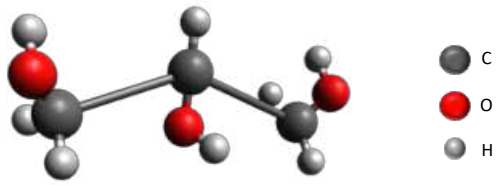


Figure I. 1. Glycerol molecule.

1.1. Importance of glycerol

Currently, it is estimated that the uses of glycerol are more than 1500 [1, 2], highlighting its participation in the production of pharmaceuticals, cosmetics, personal hygiene, in the manufacture of tobacco, food, in the production of resins, among others [3], Figure I. 2. Due to this wide variety of potential uses, glycerol is considered one of the most versatile chemicals that exist, thanks to its three hydroxyl groups, glycerol is completely soluble in water and other alcohols and in turn is insoluble in hydrocarbons. The high boiling point of glycerol (563 K at atmospheric pressure) and the high viscosity, originate from the formation of intra and inter-molecular hydrogen bonds. These properties are used to use glycerol as a softener or lubricant in resins and plastics. On the other hand, since glycerol is a non-toxic substance with a sweet taste, it can find pharmaceutical and/or food applications.

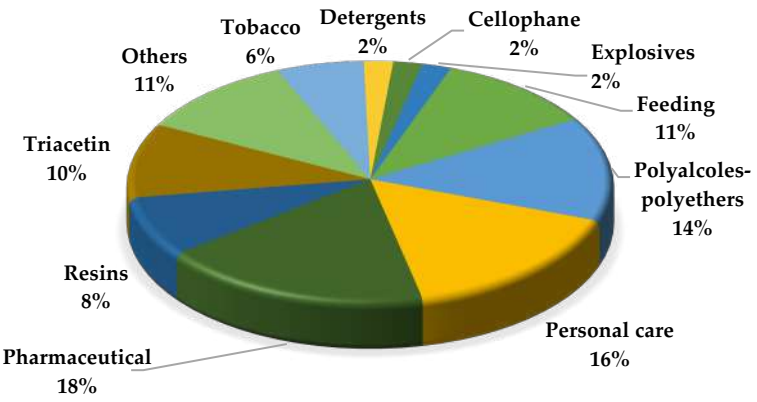


Figure I. 2. Percentage of glycerol uses.

For the year 2012, the amount of glycerol used in all its applications was close to 160,000 tons and according to the projection made for that then of a growth of 2.8% [1], the current use should be around 185,000 tons.

Although glycerol has great versatility, the progressive increase in the production of biodiesel (whose by-product is glycerol), has considerably increased glycerol to such an extent that by 2020 the production of glycerol will be six times the demand.[4]

1.2. Problem of glycerol over-production

While the outlook is good economically for the industry that directly consumes glycerol in its processes due to the imminent over-production, the outlook is contrary to the environment who has seen that biodiesel producers have chosen not to refine glycerin obtained and instead, burn it [2], since it is more profitable to make this process with the by-product than to invest in the purification and subsequent sale, Figure I. 3.

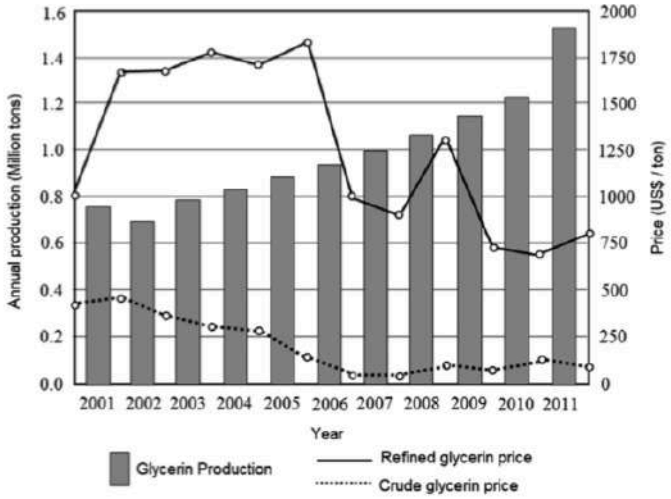


Figure I. 3. Glycerin production and price of refined and crude glycerin. *Taken from* [5]

The direct combustion of glycerin produces relatively small amounts of acrolein (~ 15 ppb) and other volatile organic compounds [6] and its emissions are comparable to those of natural gas combustion, but the opportunity to obtain other molecules could be carried out by means of the chemical transformation of glycerol. In this sense, the literature reports a large number of reactions that can be generated with glycerol as the main actor [7-9], Figure I. 4.

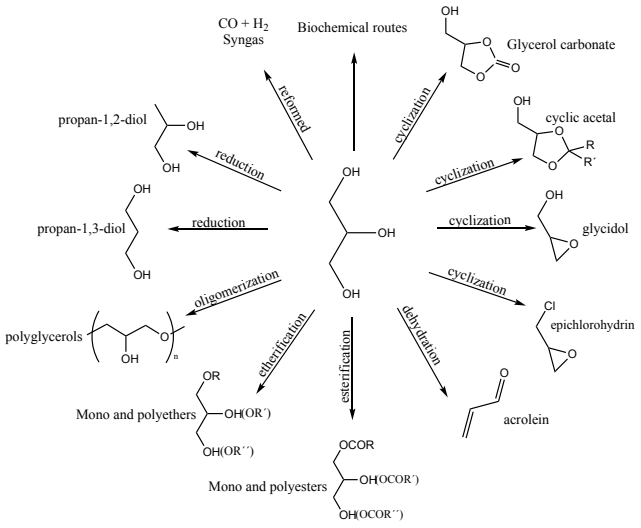


Figure I. 4. Routes of chemical transformation of glycerol. *Taken from* [9]

Among many of the possible reactions of glycerol, the etherification of glycerol is of great interest, which can be chemically carried through three different routes [10]:

1) Reaction of sodium glycerate with alkyl halides by the Williamson synthesis process;
2) Reaction of glycerol with active alkenes;
3) Reaction of glycerol with aliphatic alcohols by a condensation reaction.

Of these syntheses, the last two are used industrially, where the most common alkene is isobutene and the alcohols are generally short chain. Although it is possible to obtain these ethers with the use of isobutene as an etherifying agent of glycerol, the major drawback is the need for high reaction pressures to guarantee the solubility of the reactants. With the use of alcohols in the same phase of glycerol (liquid phase), the use of these high pressures is suppressed. In this context, the present document focuses on the use of the etherification of glycerol with alcohols in liquid phase.

The main application of these ethers is as fuel additives, becoming an alternative to the typical methyl *tert*-butyl ether (MTBE), that is widely used throughout the world despite its high toxicity to the environment. With respect to the market for these ethers, historically its use has been increasing considerably in the last three decades, where at the end of the 90s the global consumption of fuel additives was approximately 600,000 tons, with petrol additives being the most desired. with more than 50% of the total. For the year 2000, the global demand was estimated at 200,000 metric tons.[11] This increase shows that the production of fuel additives can be a good alternative to transform glycerol into ethers.

2. Etherification of glycerol with alcohols

Activated alcohols such as *tert*-butyl alcohol or benzyl alcohol have been mostly studied in the etherification of glycerol. The catalytic etherification of glycerol with less activated alcohols, such as aliphatic alcohols, is thermodynamically much more difficult.[12] In recent

years, some research has focused on this type of reactions obtaining low reaction yields. Pariente and co-workers reported the catalytic etherification of glycerol with ethanol over various solid acid catalysts.[13] A maximum yield of 40 % of mono-ethoxy glyceryl ethers was obtained at 433 K by using sulfonated polystyrene resins and zeolites with a Si/Al ratio of ca. 25. Melero and co-workers also studied the etherification of glycerol with ethanol using mesostructured functionalized silicas, where the best reaction conditions with the highest conversion and yield found were: T = 473 K, ethanol/glycerol molar ratio = 15/1, and catalyst loading = 19 wt%. Under these reaction conditions, 74% glycerol conversion and 42% yield to ethyl ethers have been achieved after 4 h of reaction but with a significant presence of glycerol by-products. In contrast, lower reaction temperatures (T = 433 K) and moderate catalyst loading (14 wt%) in presence of a high ethanol concentration (ethanol/glycerol molar ratio = 15/1) are necessary to avoid the formation of glycerol by-products and maximize ethyl-glycerols selectivity.[14]

Yadav *et al*. [15], also studied the reaction between glycerol and ethanol using zeolites (H-beta, NaX, and NaY) and SRC-120 (strongly acidic cation exchange resin), where the SRC-120 catalyst, showed highest catalytic activity followed by H-beta. These results were related in terms of the Brønsted acidity difference (0.936 of the zeolite vs 4.5 mmol H^+/g of SRC-120). The NaX and NaY zeolites showed no activity after 480 min. Based on these results, the authors conclude that there is an influence of the degree of acidity in the etherification of glycerol with ethanol. In this same work, the kinetics of the reaction was studied. The apparent activation energies of glycerol and ethanol were found to be 25.1 and 26.6 kcal/mol respectively. The high value of activation energy further confirms that the reaction is kinetically controlled.

Another short chain alcohol historically employed is *n*-butanol. Nandiwale Y. and co-workers presented for the first time in 2014 the etherification of glycerol with *n*-butanol.[16] In this study, they used several acid solids, among which are the H-beta zeolite, ZSM-5 and

K10. H-beta zeolite was found to be the most promising for the etherification reaction with glycerol conversion of 55% and a 98% selectivity towards *mono*-butyl-glycerol ether formation. The optimized process parameters were: catalyst loading of 15% (w/w) of glycerol, molar ratio of 1:9, reaction time of 4 h, reaction temperature of 433 K, and speed of agitation of 200 rpm. The optimized results were also used to develop a kinetic model for the etherification of glycerol. The activation energy and pre-exponential factor for etherification were 48.89 kJ mol^{-1} and 75.31 L h^{-1} mol^{-1}, respectively.

One year later, Fang W. and co-workers reported for the first time an experimental result to prepare silica-immobilized Aquivion PFSA (copolymer based on tetrafluoroethylene and the sulfonyl fluoride vinyl ether produced by Solvay Specialty Polymers) as heterogeneous catalyst for the acid-catalyzed direct etherification of glycerol with *n*-butanol.[17] The *n*-butanol conversion and yield to butyl glyceryl monoether reached values of 91% and 45%, respectively, at 423 K with a catalyst loading of 3 mol% H^+, while the yield to by-product of dibutyl ether was discouraged (6%).

On the other hand, Canilla and his colleagues also studied the etherification of glycerol with *n*-butanol, using Amberlyst® 15 (A-15) with temperature variations of 343–433 K.[18] The water produced in the reaction was continuously removed with the help of a permeable membrane. The results suggest a dependence of the reaction temperature with the conversion of glycerol. At 433 K, a conversion of 85.1% was obtained, with a yield of di and tri ethers of only 0.6%. The use of permeable membrane significantly increases glycerol conversion in A-15.

The etherification of glycerol with *n*-butanol at 413 K in the presence of sulfonated cation-exchange resins and zeolite catalysts in an autoclave reactor was studied by Samoilov and co-workers.[19] It was demonstrated that the styrene-divinylbenzene ion exchange resins are effective catalysts for the production of glycerol *n*-butyl ethers: the conversion of glycerol

was about 98% with a selectivity of *n*-butyl ether of about 88 % (413 K, 5 h, 5% by weight of Amberlyst 36 catalyst and 10% by weight of glycerol in *n*-butanol). The Y and β zeolites in the H^+ form exhibited a comparable specific activity (conversion of glycerol of no more than 25% under similar conditions) in combination with a high selectivity for glycerol di-*n*-butyl ethers (up to 28%).

In the study published by Gaudin and co-workers, the catalytic etherification of glycerol with various alkyl alcohols on Amberlyst® 70 (10 wt %): 1-butanol, 1-pentanol, 1-hexanol, 1-octanol and 1-decanol was evaluated.[12] When starting from 1-hexanol the reaction medium became turbid. The conversion rate of 1-hexanol was two times lower than that of 1-butanol and 1-pentanol. After 24 h, 13 % 1-hexanol was consumed compared to 25 % when starting from 1-butanol and 1-pentanol, indicating that the catalyst activity dropped significantly with an increase of the alkyl alcohol chain length. The reaction medium was biphasic when starting from 1-octanol and 1-dodecanol inducing mass transfer problems. Conversion of the alkyl alcohol was very low while the glycerol conversion was increased.

According to the reports on the etherification of glycerol with short-chain alcohols, the results depend on the acid strength and the nature of the alkylating alcohol, that is, with activated alcohols such as *tert*-butyl alcohol, it is possible to generate more percentages high conversion and selectivity towards the di and tri-ethers, while with the C4-C6 primary alcohols, poor glycerol conversion results are achieved and the selectivity towards di and tri-ethers is very low.

3. Catalytic etherification of glycerol with *tert*-butanol

The obtaining of di- and tri-*tert*-butyl ethers of glycerol (DTBG, TTBG respectively) from the etherification of glycerol with *tert*-butyl alcohol and with potential use as additives for fuels,[20] is a reaction whose first reports appear in 1994, [21] although the etherification reaction

in the presence of acid catalysts dates back to 1934 with the main production of glycerol mono-*tert*-butyl ether (MTBG).[22]

Figure I. 5, represents the etherification reaction of glycerol (G) with *tert*-butyl alcohol (TBA).

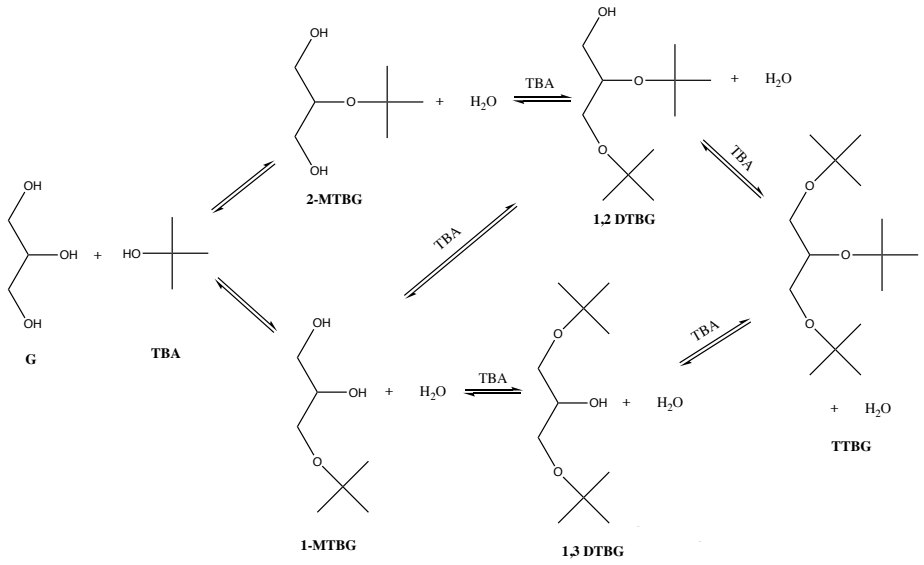


Figure I. 5. Reaction of etherification of glycerol with *tert*-butyl alcohol.

Previous studies described in the literature concerning the mechanism for this reaction, propose a rapid protonation of *tert*-butyl alcohol in acidic sites, thus generating a tertiary carbocation capable of reacting with glycerol. Additionally, etherification with *tert*-butyl alcohol produces isobutene and di-isobutene as byproducts by the dehydration of alcohol. The formation of these products is clear evidence of the competition between glycerol and *tert*-butyl alcohol for acid sites on the catalytic surface, [23] Figure I. 6.

These ethers can improve the detonation and the octane level of gasoline [24, 25] since they present values of 112-128 and 91-99 in BRON and BMON respectively (where these values indicate that they are suitable to be used as gasoline components),[4] and in particular, the di- and tri-*tert*-butyl glycerol ethers, reduce the emission of particulate matter, hydrocarbons,

carbon monoxide and aldehydes. As these ethers at room temperature are completely soluble in diesel, they can reduce the viscosity of this, [20, 26] for this reason, they are the desired products for this reaction. The mono-*tert*-butyl ether of glycerol becomes the least desired product for this application due to its low solubility in diesel.[27]

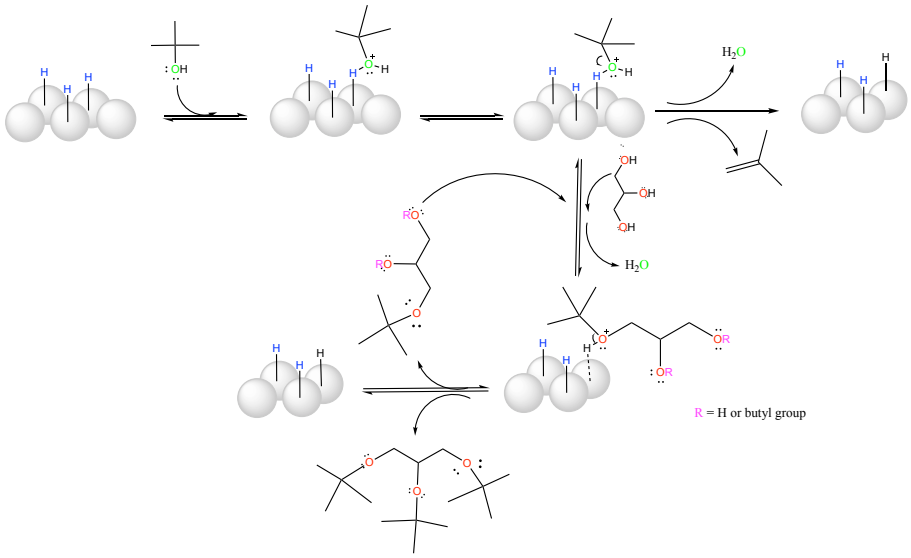


Figure I. 6. Proposed mechanism of glycerol etherification with *tert*-butyl alcohol in the Brønsted acid sites.

Since the idea of transforming glycerol into ethers by etherification with *tert*-butyl alcohol arose, numerous catalysts have been employed. The most relevant studies for this reaction are listed below.

4. Acid catalysts for the etherification of glycerol with *tert*-butyl alcohol

According to the mechanism described above (Figure I. 6), the presence of Brønsted-type acid catalysts is vital to promote the formation of the carbocation *tert*-butyl active species to carry out the etherification. In this sense, the first reports relate the use of H_2SO_4, [22] as a homogeneous acid catalyst in this reaction, although the selectivity that was obtained was mostly towards mono-*tert*-butyl ether and low for di-*tert*-butyl ether. On the other hand, it is possible to use heterogeneous type acid catalysts, with which an increase in the amount of di and tri-*tert*-butyl ethers has been evidenced, compared with their homogeneous

similar. One of the first reports in the literature on the use of heterogeneous acid catalysts is that presented by Klepáčová *et al*., [28] where Amberlyst® 15 (acidic ion exchange resin) was compared with acid zeolites of large pores, H-Y and H-BEA. The results suggest a high conversion of glycerol using Amberlyst® 15, while the selectivity towards di-*tert*-butyl ether was favored by the presence of the micropores of the zeolite. Acid resins have been shown to be efficient in the etherification reaction of glycerol with *tert*-butyl alcohol. The work published by Pico *et al*., [29] is specific in the use of resins as catalysts in the etherification of glycerol with *tert*-butyl alcohol. In this work, the authors conducted a detailed study of Amberlyst® 15, Amberlite® 200 and Amberlite® IRC-50 in terms of conversion, selectivity and stability. The best results were obtained with the Amberlyst® 15 and were attributed to the high acidity and better texture properties over the other resins. With the Amberlyst® 15, a higher selectivity towards the production of *di*-ethers was also obtained. Regarding the stability study, this catalyst can be reused without significantly losing the catalytic activity. The studies in which Amberlyst® 15 is used as catalyst in the etherification of glycerol with *tert*-butyl alcohol are numerous and practically thanks to their good results, it has become the reference catalyst for this reaction; Table I. 1, summarizes some other studies that use this type of acid resin.

Table I. 1. Etherification of glycerol with *tert*-butyl alcohol using Amberlyst® 15 as a catalyst.

Molar ratio	T (K)	Reaction time (h)	Catalyst concentration (% of total glycerol weight)	Conversion (%)	Selectivity toward h-GTBG	Ref.
4	343	6	5	68.4	25	[30]
4	353	6	5	70	10	[31]
4	362.4	8	7,3	72,3	28,3	[32]
4	363	8	7,5	50,2	28,5	[33]

Other important studies of heterogeneous acid catalysts in the etherification of glycerol with *tert*-butyl alcohol are using porous materials, such as zeolites. This type of solids has proved to be a potential substitute for ion exchange resins due to its already known properties, such

as the negative charge in the tetrahedral network, high thermal stability and tunable properties, such as porosity and acidity. However, not all zeolites are suitable for this reaction since, for example, zeolites with narrow pores could cause diffusion problems due to the large molecules that must circulate along the catalyst. In this sense, different zeolites have been tested in different studies on the etherification of glycerol with *tert*-butyl alcohol, although they have limited themselves to inferring the relationship of pore size with the increase of selectivity towards h-GTBG. For this reason, chapter 3 of this document focuses on the study of this type of catalysts in the glycerol etherification reaction with *tert*-butyl alcohol.

Carbocatalysts are a type of heterogeneous acid catalysts that are candidates for the etherification of glycerol with *tert*-butyl alcohol, although there are currently very few studies on the subject. This type of solids will be detailed in chapter 4. The advantage achieved with this type of material is the high acidity of Brønsted and the high surface areas, which could generate a good activity in this type of reactions.

Frusteri *et al.*, [34] used heteropolyacids in his study, particularly phosphotungstic acid and phosphotungstic acid exchanged with cesium, both supported in SiO_2, which were shown to be active in the etherification of glycerol with *tert*-butyl alcohol, although in terms of glycerol conversion, they were much lower than those obtained with Amberlyst® 15.

Finally, Estévez *et al.*, [35] successfully used different hybrid materials based on silica and based on organosilica in the catalytic etherification of glycerol with *tert*-butyl alcohol, where they managed to obtain glycerol conversions superior to those obtained with commercial resin Amberlyst® 15 after 24 hours of reaction at 348 K. These results were related to the textural and chemical properties of these materials, in addition, the presence of water generated during the reaction did not cause an inhibition of the catalytic activity thanks to the silanol groups.

This document reports the use of different acid zeolites (Chapter 3) and carbocatalysts (Chapter 4) in the etherification of glycerol with alcohols, for this reason, it is pertinent to show in the following chapter the most useful characterization techniques to understand the behavior of this type of catalysts in the reaction.

References

1. Katryniok, B.; Paul, S.; Dumeignil, F., The Future of Glycerol: 2nd Edition. By Mario Pagliaro and Michele Rossi. *ChemSusChem* **2011,** *4* (5), 665-665.

2. Katryniok, B.; Paul, S.; Bellière-Baca, V.; Rey, P.; Dumeignil, F., Glycerol dehydration to acrolein in the context of new uses of glycerol. *Green Chem.* **2010,** *12* (12), 2079-2098.

3. Fairbourne, A.; Gibson, G. P.; Stephens, D. W., The preparation, properties, and uses of glycerol derivatives. Part I. Glycerol ethers. *J. Taiwan Inst. Chem. Eng.* **1930,** *49* (49), 1021-1023.

4. Christoph, R.; Schmidt, B.; Steinberner, U.; Dilla, W.; Karinen, R., Glycerol. In *Ullmann's Encyclopedia of Industrial Chemistry*, Wiley-VCH Verlag GmbH & Co. KGaA: 2006.

5. Quispe, C. A. G.; Coronado, C. J. R.; Carvalho Jr, J. A., Glycerol: Production, consumption, prices, characterization and new trends in combustion. *Renew. Sust. Energ. Rev.* **2013,** *27*, 475-493.

6. Steinmetz, S. A.; Herrington, J. S.; Winterrowd, C. K.; Roberts, W. L.; Wendt, J. O. L.; Linak, W. P., Crude glycerol combustion: Particulate, acrolein, and other volatile organic emissions. *Proc. Combust. Inst.* **2013,** *34* (2), 2749-2757.

7. Gu, Y.; Azzouzi, A.; Pouilloux, Y.; Jérôme, F.; Barrault, J., Heterogeneously catalyzed etherification of glycerol: new pathways for transformation of glycerol to more valuable chemicals. *Green Chem.* **2008,** *10* (2), 164-167.

8. Zhou, C. H.; Beltramini, J. N.; Fan, Y. X.; Lu, G. Q., Chemoselective catalytic conversion of glycerol as a biorenewable source to valuable commodity chemicals. *Chem. Soc. Rev.* **2008,** *37* (3), 527-549.

9. Len, C.; Luque, R., Continuous flow transformations of glycerol to valuable products: an overview. *Sustain. chem. process.* **2014,** *2* (1), 1-10.

10. Behr, A.; Eilting, J.; Irawadi, K.; Leschinski, J.; Lindner, F., Improved utilisation of renewable resources: New important derivatives of glycerol. *Green Chem.* **2008,** *10* (1), 13-30.

11. Srivastava, S. P.; Hancsók, J., Fuel Additives. In *Fuels and Fuel-Additives*, John Wiley & Sons, Inc: 2014; pp 177-269.

12. Gaudin, P.; Jacquot, R.; Marion, P.; Pouilloux, Y.; Jerome, F., Acid-catalyzed etherification of glycerol with long-alkyl-chain alcohols. *ChemSusChem* **2011,** *4* (6), 719-722.

13. Pariente, S.; Tanchoux, N.; Fajula, F., Etherification of glycerol with ethanol over solid acid catalysts. *Green Chem.* **2009,** *11* (8), 1256-1261.

14. Melero, J. A.; Vicente, G.; Paniagua, M.; Morales, G.; Munoz, P., Etherification of biodiesel-derived glycerol with ethanol for fuel formulation over sulfonic modified catalysts. *Bioresour. Technol.* **2012,** *103* (1), 142-151.

15. Yadav, V. P.; Maity, S. K.; Shee, D., Etherification of Glycerol with Ethanol over Solid Acid Catalysts: Kinetic Study Using Cation Exchange Resin. *Indian Chem. Eng.* **2016,** *59* (2), 117-135.

16. Nandiwale, K. Y.; Patil, S. E.; Bokade, V. V., Glycerol Etherification using n -Butanol to Produce Oxygenated Additives for Biodiesel Fuel over H-Beta Zeolite Catalysts. *Energy Technol.* **2014,** *2* (5), 446-452.

17. Fang, W.; Wang, S.; Liebens, A.; De Campo, F.; Xu, H.; Shen, W.; Pera-Titus, M.; Clacens, J.-M., Silica-immobilized Aquivion PFSA superacid: application to heterogeneous direct etherification of glycerol with n-butanol. *Catal. Sci. Technol.* **2015,** *5* (8), 3980-3990.

18. Cannilla, C.; Bonura, G.; Frusteri, L.; Frusteri, F., Batch reactor coupled with water permselective membrane: Study of glycerol etherification reaction with butanol. *Chem. Eng. J.* **2015,** *282*, 187-193.

19. Samoilov, V. O.; Ramazanov, D. N.; Nekhaev, A. I.; Maksimov, A. L., Heterogeneous catalytic conversion of glycerol with n-butyl alcohol. *Petrol. Chem.* **2016,** *56* (2), 125-130.

20. Izquierdo, J. F.; Montiel, M.; Palés, I.; Outón, P. R.; Galán, M.; Jutglar, L.; Villarrubia, M.; Izquierdo, M.; Hermo, M. P.; Ariza, X., Fuel additives from glycerol etherification with light olefins: State of the art. *Renew. Sust. Energ. Rev.* **2012,** *16* (9), 6717-6724.

21. Kesling, H. S.; Karas, L. J.; Liotta, F. J. Diesel fuel. US5308365A, 1994.

22. Theodore, E.; Edlund, K. R. Process and product relating to tertiary ethers. US1968033A, 1934.

23. Gonçalves, M.; Mantovani, M.; Carvalho, W. A.; Rodrigues, R.; Mandelli, D.; Silvestre Albero, J., Biodiesel wastes: An abundant and promising source for the preparation of acidic catalysts for utilization in etherification reaction. *Chem. Eng. J.* **2014,** *256* (0), 468-474.

24. Demirbas, A., Glycerol-Based Fuel Oxygenates for Biodiesel and Diesel Fuel Blends. *Energ. Source. Part A* **2009,** *31* (19), 1770-1776.

25. Di Serio, M.; Casale, L.; Tesser, R.; Santacesaria, E., New Process for the Production of Glyceroltert-Butyl Ethers†. *Energy Fuels* **2010,** *24* (9), 4668-4672.

26. Vlad, E.; Bildea, C. S.; Bozga, G., Design and control of glycerol-tert-butyl alcohol etherification process. *ScientificWorldJournal* **2012,** *2012*, 1-11.

27. Saxena, S. K.; Al-Muhtaseb, A. a. H.; Viswanadham, N., Enhanced production of high octane oxygenates from glycerol etherification using the desilicated BEA zeolite. *Fuel* **2015,** *159*, 837-844.

28. Klepáþová K. , M. D., Etherification of Glycerol. *Pet. Coal* **2003,** *45* (1-2), 54-57.

29. Pico, M. P.; Rosas, J. M.; Rodríguez, S.; Santos, A.; Romero, A., Glycerol etherification over acid ion exchange resins: effect of catalyst concentration and reusability. *J. Chem. Technol. Biotechnol.* **2013,** *88* (11), 2027-2038.

30. Klepáčová, K.; Mravec, D.; Bajus, M., Etherification of glycerol with tert-butyl alcohol catalysed by ion-exchange resins. *Chem. Pap.* **2006,** *60* (3), 224-230.

31. Yusof, Y. A. B.; Bakar, R. B. A.; Lye, O. T.; Ahmad, S. B., Process for producing etherified compounds from alcohols. Google Patents: 2008.

32. Chang, J.-S.; Chen, D.-H., Optimization on the etherification of glycerol with tert-butyl alcohol. *J. Taiwan Inst. Chem. Eng.* **2011,** *42* (5), 760-767.

33. Klepáčová, K.; Mravec, D.; Bajus, M., tert-Butylation of glycerol catalysed by ion-exchange resins. *Appl. Catal., A* **2005,** *294* (2), 141-147.

34. Frusteri, F.; Arena, F.; Bonura, G.; Cannilla, C.; Spadaro, L.; Di Blasi, O., Catalytic etherification of glycerol by tert-butyl alcohol to produce oxygenated additives for diesel fuel. *Appl. Catal., A* **2009,** *367* (1-2), 77-83.

35. Estevez, R.; López, M. I.; Jiménez-Sanchidrián, C.; Luna, D.; Romero-Salguero, F. J.; Bautista, F. M., Etherification of glycerol with tert -butyl alcohol over sulfonated hybrid silicas. *Appl. Catal., A* **2016,** *526*, 155-163.

Chapter 2:

Fundamentals of the characterization techniques of zeolites and carbocatalysts

1. Fundamentals of the most common characterization techniques of zeolites and carbocatalysts

In heterogeneous catalysis it is important to know the physicochemical properties (structural, textural, morphological and chemical properties) of the catalysts to understand their performance in the reactions in which these materials act. Table II.1 summarizes the information obtained from each characterization technique useful for zeolites and carbocatalysts (particularly graphene oxide).

Table II. 1 Information obtained from each characterization technique useful for zeolites and carbocatalysts.

Catalyst	Information	Techniques
Zeolites	Structure- crystallinity	X-ray diffraction, XRD
	Porosity	Adsorption- desorption of N_2
	Morphology	Scanning electron microscopy, SEM
		Transmission electron microscopy, TEM
	Chemical composition	X fluorescence spectrometry, XRF
		Inductively coupled plasma, ICP
	Composition of the frame	Solid state nuclear magnetic resonance ^{27}Al, NMR
		IR (TOT band) infrared spectroscopy band structure
	Acidity	Thermodesorption of pyridine at 423 K followed by IR
	Particle size	Transmission electron microscopy, TEM
Carbocatalysts	Structure- formation of graphene oxide	X-ray diffraction, XRD
		Raman spectroscopy, RAMAN
	Morphology	Scanning electron microscopy, SEM
		Transmission electron microscopy, TEM
	Surface composition	X-ray photoelectron spectroscopy, XPS
	Size of graphene sheets	Transmission electron microscopy, TEM
	Sulfur dispersion	Energy-dispersive X-ray spectroscopy, EDS
	Superficial area	Adsorption- desorption of N_2- BET method

	Acidity	Elemental analysis, EA Boehm titration
	Thermal stability	Thermogravimetric analysis, TGA

In this sense, the information reported after this section contains the principle of each technique of interest in this study.

1.1. X-ray diffraction, XRD

The X-ray diffraction technique allows to determine the crystallographic properties of solids. Additionally, it is possible to determine from the X-ray diffractograms, the crystallite size, the lattice parameters or the presence of micro distortions. This technique is based on the incidence of X-rays on a surface of a crystal with a certain angle, where only a part is reflected by the layer of atoms on the surface. The part that is not reflected penetrates the second layer of atoms where, again, only a part is reflected. The cumulative effect of these reflections on the crystal centers causes interference, both constructive and destructive. When the following two conditions occur simultaneously, the diffraction of the incident beam occurs:

- The distance between the layers of atoms must coincide with the wavelength of the incident radiation.
- The centers that provoke reflections should be distributed evenly. From these two conditions and geometric considerations, the Bragg equation allows us to predict the angle of incidence of the beam required for the constructive interference of X-rays to occur:

$$2d_{hkl} \text{ x } \text{sen}\theta = n \text{ x } \lambda \qquad \text{(Eq. 1)}$$

Where:

- d: is the distance between two Miller index planes;
- θ: is the angle of incidence of X-ray beam (Bragg angle);

- n: is the order of diffraction;
- λ : is the wavelength of X-rays.

Destructive interference occurs with any other angle of incidence. The identification of the crystalline phases present is done by comparison of the experimental diffractogram with those of reference contained in the International Center for Diffraction Data (ICDD) database.

The information obtained from the X-ray diffraction for zeolites allows to recognize its structure efficiently. For graphene oxide, X-ray diffraction is a useful tool to know the distance (d_{hkl}) between the sheets after performing the oxidation processes in the graphite (this will be detailed in Chapter 4).

1.2. Adsorption- desorption of N_2

The process to determine the surface area of a porous structure is through the adsorption-desorption of a molecular species, a gas or a liquid, on the surface to be determined. The measurement of the total surface area of a sample requires non-selective physical absorption. The isotherms obtained from the adsorption- desorption of nitrogen gas represent the volume of gas adsorbed as a function of the relative pressure of nitrogen. The curve $V = f(p/p_0)$ is obtained with V that corresponds to the volume of nitrogen adsorbed per gram of sample under standard conditions of temperature and pressure, p the system pressure and p_0 is the saturation vapor pressure. The graph of the adsorption isotherm consists in measuring the adsorbed nitrogen volumes for different increasing values of p/p_0 between 1.0 $x10^{-7}$ and 1 bar. The desorption isotherm is obtained by determining the quantities that remain adsorbed in the solid for decreasing values of p/p_0.

1.2.1. Isotherm classification

One of the advantages of isotherms is to be able to classify the type of material studied by the shape that it acquires after absorption-desorption of nitrogen. Most physisorption isotherms are included in six defined types, as shown in Figure II. 1.

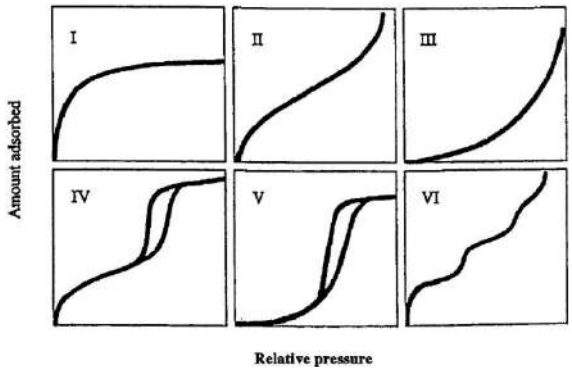


Figure II. 1. Types of physisorption isotherms. *Taken from* [36]

Type I

Pores are typically microporous with the exposed surface residing almost exclusively inside the micropores, which once filled with adsorbate, leave little or no external surface for further adsorption. This is the most frequent case encountered for zeolites and activated carbons.

Type II

Most frequently found when adsorption occurs on nonporous powders or powders with diameters exceeding micropores. Inflection point occurs near the completion of the first adsorbed monolayer.

Type III

Characterized by heats of adsorption less than the adsorbate heat of liquification, adsorption proceeds as the adsorbate interaction with an adsorbed layer is greater than the interaction with the adsorbent surface.

Type IV

Occur on porous adsorbents with pores in the range of 1.5 – 100 nm. At higher pressures the slope shows increased uptake of adsorbate as pores become filled, inflection point typically occurs near completion of the first monolayer.

Type V

Are observed where there is small adsorbate- absorbent interaction potentials (similar to type III), and are also associated with pores in the 1.5 – 100 nm range.

Type VI

These types are due to a multi-layer adsorption process on materials with orientation on a particular crystal face (multilayer adsorption on a homogeneous non-porous surface). Argon or krypton on graphitized carbon blacks are the most popular examples of this type of isotherm obtained at liquid nitrogen temperature.

1.2.2. Specific Surface – BET surface

The specific surface area (S_{BET}) of the samples can be calculated using the BET method, proposed by Brunauer, Emmet and Teller. [37] This method is the most used for the analysis of the adsorption data, which introduces a series of simplifications for its application. The BET equation can be described as:

$$\frac{\frac{p}{p_0}}{V\left(1-\frac{p}{p_0}\right)} = \frac{1}{V_{mono}.C} + \frac{C-1}{V_{mono}.C}\ x\ \frac{p}{p_0} \qquad \text{(Eq. 2)}$$

Where:

- V: is the volume of nitrogen adsorbed at the equilibrium pressure p (cm^3g^{-1});
- V_{mono}: is the volume of the nitrogen monolayer adsorbed on the solid (cm^3g^{-1});
- P_0: is the saturation pressure of the nitrogen vapor;
- C: is the constant that depends on the molar heat of adsorption of the first layer on the surface of the material (E_1) and the molar heat of nitrogen liquefaction (E_L). The

strong adsorbent-adsorbate interactions are characterized by a high value of constant C.

$$C = \exp\left(\frac{E_1 - E_L}{RT}\right) \qquad \text{(Eq. 3)}$$

Where:

- R: is the perfect gas constant, R = 8.314 J.mol^{-1} K^{-1};
- T: is the temperature in K.

Once the V_{mono} value is calculated, the specific surface area of the material (S_{BET}) is obtained from the equation:

$$S_{BET} = n \times N_A \times \sigma(N_2) = \frac{V_{mono} \times N_A \times \sigma(N_2)}{V_m} = 4{,}35 \times V_{mono} \qquad \text{(Eq. 4)}$$

Where:

- n: is the number of moles of gas contained in a monolayer and equal to V_{mono}/V_m (Vm = is the molar volume of the gas under standard temperature and pressure conditions = 22.4 L mol^{-1});
- N: is the number of Avogadro (6,023 x 10^{23} mol^{-1});
- σ: is the area occupied by an adsorbed nitrogen molecule (16.2 Å^2).

1.2.3. Pore volume

The total pore volume is considered equal to the volume of the adsorbed nitrogen in the pores in the liquid state, at the relative pressure $p/p_0 = 1$. It can be expressed by the equation:

$$V_{porous} = \frac{\rho_{gas} \, x \, V}{\rho_{liquid}} = 1{,}547 \; x \; 10^{-3} \; x \; V \qquad \text{(Eq. 5)}$$

Where:

- V_{porous}: it is the total pore volume (cm^{3}g^{-1});
- ϱ_{gas}: is the density of the nitrogen in gaseous state;
- ϱ_{liquid}: is the density of liquid nitrogen;

- V: is the volume of gaseous nitrogen adsorbed in the pores of the material at p/p_0 = 1 (cm^3g^{-1}).

The volume is estimated using the *t*-plot method, based on the relationship:

$$V_{ads} = V_{micro} + S_{ext} + t \quad \text{(Eq. 6)}$$

Where:

- V_{ads}: is the volume of nitrogen adsorbed at the relative pressure p/p_0 (cm^3g^{-1});
- S_{ext}: is the specific surface not related to the micropores (external surface);
- *t*: is the thickness of the nitrogen layer adsorbed on the material at the relative pressure p/p_0.

The thickness "*t*" can be determined using the Harkins-Jura equation:

$$t = \sqrt{\frac{13,99}{0,034 - log\frac{p}{p_0}}} \quad \text{(Eq. 7)}$$

The determination of the micropore size distribution was performed by the Horvath-Kawazoe method and the Saito-Foley method adapted to cylindrical pores. This method is based on the fact that the pressure p/p_0 required to fill a pore of given size and shape is directly related to the adsorbate- adsorbent interaction energy:

$$RTLn\left(\frac{p}{p_0}\right) = f\left(\emptyset(r)_{pore}\right) \quad \text{(Eq. 8)}$$

$\emptyset(r)_{pore}$: is the Lennard-Jones type interaction potential of a molecule of gas adsorbed at a distance r from the solid surface, depending on the characteristics of the solid and the gas.

The porous materials can be characterized by the size distribution of its pores. In this case, it is assumed that the pores of each size independently contribute to the adsorption isotherm in a proportion relative to the total area of the sample.

1.3. Scanning electron microscopy, SEM

The scanning electron microscopy technique allows to obtain two-dimensional images of the secondary electrons emitted by the analyzed sample after being bombarded with an electron beam. The secondary electrons are of low energy (less than 50 eV), for this reason the electrons closest to the surface are detected. As a result, bright areas and shadows are obtained depending on the topography of the sample, which is used for the physical characterization of particles, size, shape, characteristics of particle aggregates, etc.

A possible additional analysis of the electron microscope is the X-rays produced when bombarding the sample with the electron beam. The electronic microprobe (EDS) analysis allows obtaining chemical information of most of the elements present in the sample and, by selecting a characteristic wavelength, it is possible to obtain a mapping of the different elements.

1.4. Transmission electron microscopy, TEM

In TEM analysis, an electron beam generated by a hot filament (electronic cannon) is used, which passes through two electrodes and a condenser lens. Parallel rays create an impact on the sample, where they are scattered as a result of the variable spatial refractive index. The scattered rays from the point of incidence in the sample are directed to the same point in the image formed by the objective lens. The total effect is equivalent to the transmission of primary electrons through the sample.

1.5. X fluorescence spectrometry, XRF

The technique of X-ray fluorescence spectrometry (XRF) consists in the bombardment of a sample with an electron beam or with X-ray photons, where a small part of the energy is inverted in the production of the characteristic X-ray spectrum of the elements that they form the bombed sample. The production process of this characteristic spectrum is

summarized in two processes, one of excitation and the other of emission. The excitation process with another X radiation is called secondary excitation, and the X radiation produced by the excitation of another X radiation is called secondary X radiation or fluorescence radiation. It is the secondary radiation X characteristic that is used for the chemical analysis in the X-ray fluorescence spectrometers. Being, the energies of the different electronic levels characteristic for each type of atoms, the X radiation emitted will be characteristic for each element. and, in principle, it will not depend on the chemical substance in which it is found, since, in general, these radiations are caused by transitions between the internal electronic levels, whose energies are not affected by the type of existing link.

When the energy of electrons that impact on an atom is equal to greater than the energy of level K, the ejection of an electron from said K layer can occur, transitions from higher levels give rise to a series of characteristic radiations of lengths of similar waves that constitute the K series (they are called Kα, Kβ, ...). It is the highest energy series (shortest wavelength).

If the vacancy occurs in one of the sublevels of the L layer, transitions from higher levels result in the characteristic radiations of the L series (Lα, Lβ, ...). The same can be said for layer M.

Although the number of possible characteristic radiations for each element is large, in practice the intensity of many of them is very small (very small probability of the electronic transition that originates them), and can not be registered with the measuring equipment; In addition, the number of recorded radiations is even more limited, because the energy difference between some of them is so small that they appear together. This means that, in practice, the characteristic spectrum of an element can be deduced from two or three radiations of the K series, and from four to ten of the L series. The radiations of the M series in the normal work area only they appear normally for the heavier elements.

X-ray fluorescence spectrometry (XRF) is a very useful technique for determining the concentration of silicon and aluminum elements present in zeolites and determining the Si/Al ratio.

1.6. Inductively coupled plasma, ICP

Inductive coupling plasma (ICP) is a source of ionization that, together with an optical emission spectrophotometer (OES), constitutes the ICP-OES equipment. In this technique, the continuous introduction of the liquid sample and a nebulization system form an aerosol that is transported by the argon to the plasma torch, coupled inductively by radiofrequency. In the plasma, due to the high temperatures generated, the analytes are atomized and ionized generating the atomic emission spectra of the characteristic lines. The spectra are dispersed by the diffraction grating and the light sensitive detector is responsible for measuring the intensities of the lines. The information is processed by a computer system.

This technique is useful to know the percentage of Si and Al present in the zeolite and, in this way, the results obtained by XRF can be complemented.

1.7. Solid state nuclear magnetic resonance ^{27}Al, NMR

Nuclear Magnetic Resonance (NMR) of solids is a non-destructive technique that provides qualitative and quantitative information of solid materials. The only drawback of this technique is that it requires for the analysis of large amounts of sample due to its low sensitivity.

In solid NMR, a system of nuclear spins in the presence of a static magnetic field is capable of absorbing radio frequency (RF) energy when irradiated with an RF source. Due to the low mobility of atoms and molecules, the spectra obtained show wide signals as a consequence of the different orientations of the spins in space. In addition, each nucleus is

affected, according to the relative orientation of the molecule, its electronic distribution, the external magnetic field and the fields created in nearby nuclei. The main interactions responsible for the amplification of the signals are the anisotropy of the chemical change, the dipolar couplings (homo and heteronuclear) and the quadrupole coupling.

For atomic nuclei with a magnetic moment (nonzero spin), the magnetic field B_0 removes the degeneration of energy levels. This Zeeman effect is translated by a Hamiltonian:

$$H_Z = -\gamma B_0 I_z \qquad \text{(Eq. 9)}$$

Where I_Z is the spin operator in projection on the z-axis, by definition confused with the axis of the magnetic field. All the other interactions that the nucleus can undergo result in a Hamiltonian which is a first-order disturbance of the Hamiltonian Zeeman. These interactions are interesting since they explain the shape of the absorption lines, their displacement, their resolution or their enlargement. They are translated locally by fluctuations in the magnetic field felt by the nucleus.

Due to the anisotropy of chemical displacement and the existence of di- or quadrupole interactions (nuclei with a spin greater than 1/2), the signals obtained are relatively wide compared to those observed in the liquid phase.

The chemical shift of aluminum depends on its coordination: from 0 to 22 ppm for coordination 6 (Al^{VI}) and from 50 to 80 ppm for coordination 4 (Al^{IV}). The presence of extra-lattice aluminum can thus be detected from the ^{27}Al NMR spectra.

1.8. IR (TOT band) infrared spectroscopy band structure

Infrared spectroscopy is based on the interaction of the molecules with the electromagnetic radiation in the infrared zone, which leads to the absorption of this radiation and,

subsequently, the incident molecules will be excited and will be reflected in the form of changes in the intensities of the vibrations. These vibrations in turn depend on the atoms that form the bond in the molecule. The interferogram is the name of the format of the signal acquired by an infrared spectrometer and is a complex signal that must be analyzed; however, this format can be transferred to what we know as infrared spectrum, by means of an algorithm called Fourier transform which was developed in 1965. Practically all current infrared equipment comes with the Fourier transform included.

This technique is very useful for the study mainly of zeolites because it allows to study the hydroxyl (OH) stretching vibrations bands in the range of 3500 – 3800 cm^{-1} (associated to the Brønsted acidity), to use the probe molecules pyridine for the quantification of the samples acid sites density and to determine the framework Si/Al ratio of the zeolites through the use of the zeolite structure bands.

The zeolite network vibrations, observed between 300 and 1300 cm^{-1}, can be classified in two categories according to whether they are insensitive to the zeolite structure (vibrations internal to the TO_4 tetrahedra) or sensitive to the topology of the framework (vibration of the external links between tetrahedra). The position of the bands depends significantly on the composition of the zeolitic framework; a decreasing linear relationship is generally found between the wave number and the mol fraction of Al in the x_{Al} framework (or the number of Al per elementary mesh N_{Al}). The decrease of the vibration frequencies with the increase of the Al content is explained by the decrease of the average force constant of the TO bonds: the Al-O bond is longer than the Si-O bond and the aluminum less electronegative than silicon. Determining x_{Al}, therefore the Si/Al ratio of any zeolite by the position of IR bands insensitive to the structure, seems immediate and otherwise inexpensive in sample (the measurement is done on the sample diluted in KBr). Unfortunately, even for these so-called structure-insensitive bands, a large dispersion is obtained in the frequency vs relation x_{Al} if samples of various zeolites are used. Therefore,

an accurate determination of the Si/Al ratio requires the prior drawing of a standard duty for the zeolite considered.

1.9. Thermodesorption of pyridine at 423 K followed by IR

Pyridine adsorption and subsequent IR analysis is a way to easily measure the type, quantity and strength of acidic sites on a surface. [38] To distinguish between an acid Lewis site and acid Brønsted site, pyridine is coordinated with the first and protonated with the second, which is reflected in different modes of infrared vibration. [39]

The limitation of this technique is that it is not applicable to all solids. For the analysis, the material is compressed forming a block of this and then to be placed in the analysis cell, samples that are completely dark (such as coals) do not allow the passage of radiation to the detector.

1.10. Raman spectroscopy, RAMAN

The Raman spectroscopy analysis consists in making a monochromatic light beam of frequency ν_0 impinged on a sample where a part of the light will be dispersed. Most of the scattered light has the same frequency as the incident light, but a very small fraction has a frequency change as a result of the interaction of light with matter. The light that maintains the same frequency ν_0 as the incident light is known as Rayleigh scattering and does not provide any information on the composition of the sample analyzed. The scattered light that presents different frequencies of the incident radiation, is the one that provides information about the molecular composition of the sample and is what is known as Raman scattering. The new frequencies, $+\nu_r$ and $-\nu_r$, are the Raman frequencies, characteristic of the chemical nature and physical state of the sample and independent of the incident radiation.

Raman is an analysis technique that is carried out directly on the material to be analyzed without the need of a special preparation and that does not involve any alteration of the surface on which the analysis is carried out, that is, it is not destructive.

This technique is very useful in graphene oxide-based solids because it allows to recognize the presence of sp^3 type carbons, as a product of graphite oxidation processes, which indicates the degree of oxidation of the material. [40]

1.11. X-ray photoelectron spectroscopy, XPS

A sample irradiated with X-rays of a certain energy is capable of emitting a photoelectron. The principle of electronic X-ray spectroscopy is given by:

$$h\nu = E_b + E_k \qquad \text{(Eq. 10)}$$

Where:

- $h\nu$: is the energy of the incident photon
- E_b: is the electron bonding energy (photoionization energy)
- E_K: is the kinetic energy (measured in the spectrometer) of the electrons that escape from the atoms of the solid.

By means of this technique it is possible to examine the chemical nature and the binding energy of the atoms through the analysis of the photoemission peaks of the electrons.

Because the free inelastic free path of photoelectrons is in the range of 0.5-5 nm, this technique provides information on the first surface layers of the solid.

As a qualitative analysis, it provides information about the elements present in the sample and their respective oxidation state, but also allows a quantitative analysis, since the intensity of the peaks is a function of the number of atoms present on the surface of the

sample. In general, the relative amounts of the different elements on the surface are calculated according to:

$$\frac{I_a}{I_b} = \frac{\sigma_a \lambda_a S_a}{\sigma_b \lambda_b S_b} \qquad \text{(Eq. 11)}$$

Where:

- σ: is the photoionization section, which indicates the efficiency of the photoionization and depends on the element analyzed, the incident X-rays and the atomic orbital. The values that have been calculated mainly by Scofield are tabulated;
- λ: is the average free electron path (calculated by Penn and tabulated);
- S: it is an instrumental function that depends on the spectrometer and calculated through a connection provided by each XPS apparatus.

This technique is also very useful to know in carbocatalysts (particularly in graphene oxide) the degree of oxidation to be able to observe and quantify the C-O band.

1.12. Elemental analysis, EA

The elemental analysis technique allows to determine the total content of carbon, hydrogen, nitrogen and sulfur (C, H, N and S) present in organic and inorganic samples, which can be solid or liquid and have no calcium or phosphorus. The elemental analysis of C, H, N and S is based on the volatilization of a sample by total combustion (approximately 1173 K) in a pure oxygen atmosphere, releasing the elements to be measured in the form of CO_2, H_2O, NOx and SOx, respectively. A subsequent reduction process transforms the NOx and SOx into N_2 and SO_2, respectively. All gases thus formed (CO_2, H_2O, N_2 and SO_2) are analyzed quantitatively in a detector.

The elemental analysis allows to know the C/O radius of the graphene oxide-based catalysts. In addition, the quantification of sulfur by elemental analysis in carbocatalysts

functionalized with this element to confer acidity, is a good approximation that complements the acidity measurements carried out by the titration processes. [41]

1.13. Boehm titration

This technique allows to determine the amount of acid functional groups present on the surface of carbocatalysts, which is based on selective neutralization by equilibrium. It consists of neutralizing the surface acid groups present in the sample, knowing the pKa of a given acidic functional group, this can be neutralized by a base with a higher pKa value such as NaOH. [42]

1.14. Thermogravimetric analysis, TGA

Thermogravimetric analysis (TGA) provides a quantitative measure of any weight change associated with thermally induced transitions. A continuous and accurate record of the weight shows the changes in a substance under certain environmental conditions. Using a suitable temperature program, it is possible to obtain qualitative and quantitative information about the composition and structure of the phases of a given catalytic system. By means of this technique it is possible to know the thermal stability of the catalysts based on graphene oxide.

References

1. Leddy, N., Surface area and porosity. *CMA Analytical Workshop* **2012**, 1-28.

2. Brunauer, S.; Emmett, P. H.; Teller, E., Adsorption of Gases in Multimolecular Layers. *J. Am. Chem. Soc.* **1938,** *60* (2), 309-319.

3. Acidic sites on catalyst surfaces and their determination. *Catal. Today* **1989,** *5* (1), 1-120.

4. Miranda M, C. D.; Ramírez S, A. E.; Jurado, S. G.; Vera, C. R., Superficial effects and catalytic activity of ZrO2–SO42− as a function of the crystal structure. *J. Mol. Catal. A: Chem.* **2015,** *398*, 325-335.

5. Yang, D.; Velamakanni, A.; Bozoklu, G.; Park, S.; Stoller, M.; Piner, R. D.; Stankovich, S.; Jung, I.; Field, D. A.; Ventrice, C. A.; Ruoff, R. S., Chemical analysis of graphene oxide films after heat and chemical treatments by X-ray photoelectron and Micro-Raman spectroscopy. *Carbon* **2009,** *47* (1), 145-152.

6. Oger, N.; Lin, Y. F.; Labrugère, C.; Le Grognec, E.; Rataboul, F.; Felpin, F.-X., Practical and scalable synthesis of sulfonated graphene. *Carbon* **2016,** *96*, 342-350.

7. Boehm, H. P.; Diehl, E.; Heck, W.; Sappok, R., Surface Oxides of Carbon. *Angew. Chem. Int. Ed.* **1964,** *3* (10), 669-677.

Chapter 3:

Zeolites in the etherification of glycerol with *tert*-butyl alcohol

(Based on the publication: C. Miranda *et al.* / Journal of Catalysis 365 (2018) 249–260)

1. Zeolites

Although the systematic use of zeolites began in the mid-twentieth century, its discovery dates back to the eighteenth century. It was in 1756 when the Swedish geologist and Baron Axel Fredrick Cronstedt discovered that styrbite, a natural mineral, lost water by heating it with a torch flame (intumescence), and called this class of zeolite materials, from the Greek *zeo* means boiling *lithos* which refers to stone, since many zeolites seem to boil when heated.[1-3]

After the discovery of this type of material, new different structures of natural zeolites were also discovered but remained only as scientific findings for about 150 years. It was not until the late nineteenth and early twentieth century that some references began to appear to the applicability of these materials to ion exchange and the adsorption of a variety of molecules.

Wiegel and Steinhoff [4] published in 1924 the first effect of selectivity of the form with dehydrated chabazite. They observed that this zeolite had the property of quickly and selectively adsorbing water and ethanol, but neither acetone nor benzene. Due to this fact, in 1932, McBain [5] designated these materials as molecular sieves.

The first attempts to obtain zeolitic materials, tried to imitate nature, that is, syntheses were made at temperatures close to 773 K and high pressures using volcanic glasses or natural silicates. Milton and Barrer were the pioneers in the hydrothermal synthesis at the beginning of the 40s; Barrer studied the conversion of known phases, under the action of concentrated solutions of salts at high temperatures (443- 543 K), synthesizing a zeolite without natural analogue known as KFI (ZK-5). [6] Milton for his part introduced in his synthesis the use of more reactive starting materials (silicate and sodium aluminate) and using softer synthesis conditions of crystallization, which generated the discovery of new zeolitic structures, and together with Breck had already synthesized 20 zeolites in the early 50's, among them, the zeolites A and X, [7] whose properties and commercial uses greatly boosted the research in zeolites.

In the following decade there were numerous events both in new discoveries of structures and in the techniques of synthesis of zeolites. For example, in the 60s, quaternary ammonium cations began to be introduced, which had a great impact, giving rise to the first zeolites synthesized in the laboratory with a high content of silica (5 < Si/Al <100), such as Beta zeolite using the tetraethylammonium cation, [8] and later, in 1972, the zeolite ZSM-5. [9]

The first report on industrial application in catalysis appeared in the 1960s, where zeolites began to replace amorphous silica and alumina catalysts in catalytic cracking processes. The use of zeolites as catalysts grew rapidly due to their properties of ion exchange, internal acidity, high activity, thermal stability and, mainly, selectivity of forms. [3, 10, 11]

The use of fluoride anions in the synthesis of zeolites, in the 70s, was first introduced by Flanigen and Patton. [12] In the 1980s, it was discovered a completely new family of crystalline microporous materials, the aluminophosphates (AlPOs). [13]

Nearly 200 unique structures of natural and synthetic zeolite structures have been identified and more than 40 zeolite structures of natural origin are known. [14-16]

Each topology of the zeolite framework is identified by a capital code of three letters, established by the Structure Commission of the International Zeolite Association (IZA), following the rules set up by the International Union of Pure and Applied Chemistry (IUPAC) Commission on Zeolite Nomenclature in 1978. [17]

1.1. Structure

From a structural point of view, a zeolite could be defined as a crystalline aluminosilicate, within the family of tectosilicates, three-dimensional silicates or silicates of structure in the framework constituted by a main structure of tetrahedrons [TO_4], where T usually represents a tetravalent ion as Si^{4+} and/or trivalents such as Al^{3+}. While the former results in as electrically balanced environment, the aluminum T-site results in a negative charge in the structure and must be compensated by the presence of a cation (M, alkali or alkaline earth

metals) in the framework (Figure III.1). These compensating cations can be easily exchanged by other ones, particularly by protons (H^+), introducing then acidic properties. [18]



Figure III. 1 Negative charge induced by the AlO_4^- tetrahedron in the structure, neutralized by a compensating cation (M^+).

The structural formula of a zeolite is based on the crystallographic unit cell, the smallest unit of the structure, represented by:

$$M^{n+}_{x/n}[(AlO_2)_x(SiO_2)_y].zH_2O$$

Where n is the valence of the counter cation M, z is the number of water molecules per unit cell, (x+y) is the total number of SiO_4 or AlO_4^- tetrahedra per unit cell and y/x the atomic Si/Al ratio. According to the Lowenstein rule, an oxygen atom can not be covalently bound to more than one aluminum atom in the framework, i.e., Al-O-Al groups do not exist in zeolite networks. Consequently, the atomic Si/Al ratio varies from a minimal value of 1 to infinite. [3, 10]

Structurally, the oxygen atoms which form two distinct covalent bonds, act as connecting bridges between close T-atoms, then forming the three-dimensional framework. Hence, neighboring T-sites join together to form more complex structures with well-defined shapes, such as rings and cages known as secondary building units (SBU). These SBU can then bond with each other to form larger structures as channels, pores and cavities from 0.2 to 1 nm, where only small molecules can penetrate and circulate. The enormous variety of paths and sizes arranged by these structures is the origin of all the diversity of zeolites (Figure III.2).

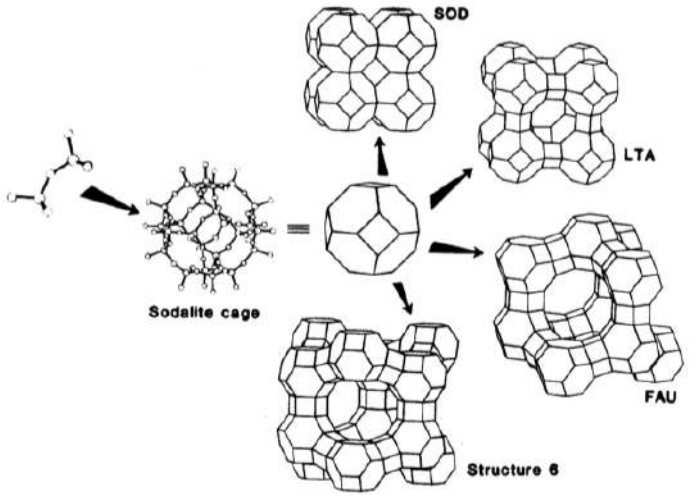


Figure III. 2 Tetrahedra arrangement, forming the sodalite (or β-cage) and, finally, the structure of some zeolites, showing the three-dimensional channel network. *Taken from* [19]

The size and shape of the pores are of fundamental importance since they are the major responsible for the molecular sieve properties and catalytic shape selectivity. The diameter of the channels of angstrom scale, prevents bulky molecules from entering the pores and, at the same time, hinders larger molecules formed in their interior to diffuse around or out freely. The acidity may also be adjusted from weak to very strong or even superacid, by the variation of the Si/Al ratio, the calcination conditions or cations exchange.

Considering the pore size, the zeolites can be classified into three major categories [3]:

- small-pore zeolites, with 8 membered-ring pore apertures (8 T-atoms and 8 oxygen atoms) having free diameters of 0.30 – 0.45 nm (e.g. zeolite A);
- medium-pore zeolites, with 10 membered-ring apertures, 0.45–0.60 nm in free diameter (e.g. zeolites ZSM-5 and MCM-22);
- large- pore zeolites, with 12 membered-ring apertures, 0.60–0.80 nm (e.g. zeolites Y and Beta).

Besides the pore sizes presented above, there are also zeolites with 6-membered ring pore apertures (e.g. sodalite, ZSM-39), which have no catalytic significance, since their pore apertures are too small, even for molecules like methane. [20] On the other hand, zeolite-like

materials with ultra-large pores such as VPI-5 (aluminophosphate 18 T-atoms, 1.27 nm), [21] $AlPO_4$-8 (aluminophosphate 14 T-atoms, 0.79 × 0.87 nm) [22] and Cloverite (gallophosphate 20 T-atoms, 0.60 × 1.32 nm) [23] were discovered in the early nineties of the previous century. Zeolites can also be distinguished by their dimensionality, which determines the modes of diffusion of molecules in the pores. They may then be mono-, bi- or three-dimensional, in which the molecules can diffuse in only one, two directions in a plane or three directions in space, respectively.

1.2. Acidity

The concept of solid acids is of major importance in many aspects related to the applications of solid surfaces and, in particular, for catalytic purposes. [24] The concept of acid of solids was originally proposed by Walling, in the 1950's, as the "ability (of a surface) to convert an adsorbed neutral base to its conjugate acid", [25] as evidenced in zeolites by the higher heats of adsorption of nitrogen bases. [26]

To describe the acidity of the zeolites, it is pertinent to distinguish between the nature of the acid sites, their density and/or concentration, the strength of the acid sites and the distribution of the force and the location of these sites in the zeolite lattice.

1.2.1. Nature of the acid sites

The acidity of the zeolites is defined by two different types: Brønsted and Lewis acid sites. In the Brønsted theory, an acid is defined as a proton donor and a base as a proton acceptor (a base must have a pair of electrons available to share with the proton).[27] For its part, a Lewis acid corresponds to a broader theory in which an acid is any species with a vacant orbital that can accept a pair of electrons, while a base is a species that has a pair of electrons not shared.[28] The first type of acidity occurs when aluminum replaces silicon in the tetrahedral T-sites of the framework (Figure III.1). In this way, a cation is required to satisfy the Al tetrahedron. If this cation is a proton (which is usually the case), the proton is a strong Brønsted acid, Figure III.3.

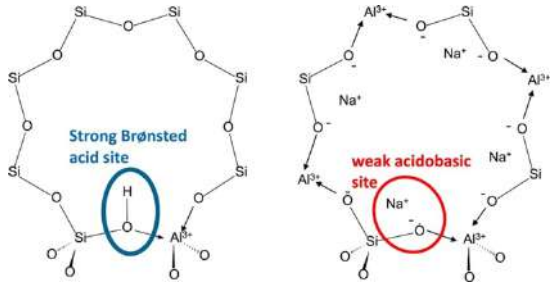


Figure III. 3 Brønsted acid formation in the zeolites. *Taken from* [29]

Lewis acidity can arise from different situations such as the presence of different metal species located within the framework of zeolite and the compensating cations that surround the aluminum atoms. Furthermore, the presence of extra-framework aluminum species (EFAl), formed during the crystallization procedure or caused by dealumination processes, also contribute to this type of acidity. This type of Aluminum often dispersed in the zeolite pore structure, but it can also appear on the exterior of the zeolite crystals or even at the pore mouths. Different aluminum oxides and hydroxides present Lewis acidity, such as Al^{3+}, AlO^{+}, $Al(OH)_2^{+}$, $Al(OH)^{2+}$, $AlO(OH)$, $Al(OH)_3$, $[Al_2O_2OH]^{+}$ or $[Al_2O]$.[30-32] The framework aluminum atoms can also behave as Lewis sites after the partial damage of the structure, caused by dehydroxylation reactions occurring at high temperatures (usually above 773 K) and which removes one of the oxygen atoms bonded to the aluminum. [33]

1.2.2. Acid sites density

The density of the acid sites is the number of Brønsted and/or Lewis acid sites per catalyst unit. In zeolites, this density is represented as a function of the concentration of aluminum atoms, expressed by the silicon-aluminum ratio (Si/Al). The Brønsted density is relatively equal to the number of aluminum atoms in the frame balanced by the presence of protons, while the number of Lewis acid sites can be considered approximately equal to the sum of the extra-frame aluminum atoms and those that they are in the frame but present a free valance or are electrically compensated for the existence of a neighboring cation. In addition, in cases where other metals are incorporated in the framework structure and when they act as Lewis sites, the acid density even increases.

However, the information of the density is insufficient to characterize the acidity of the zeolites or to make any previous assumptions on their catalytic behavior. For example, for some acid catalyzed reactions, a zeolite with fewer but stronger sites can have a better performance and activity then other with larger densities of weaker sites.

1.2.3. Acid sites strength

It is well known that not all acid sites in zeolites have the same strength. The qualitative evaluation of the strength of the acid sites is not a difficult task, especially if one simply tries to compare the relative acidity between two or more sites. A quantitative analysis of the strength of acidic sites turns out to be a more complex task that requires the establishment of a reasonable and logical universal acidity scale. In this sense, some scales have been proposed and vary from the most theoretical principles, such as the energy of deprotonation of the Brønsted sites, to the most accessible methods from the experimental point of view, such as the energy of adsorption (or desorption) of gaseous bases, in particular ammonia.

Below are the factors that can influence the strength of the Brønsted acid sites.

1.2.3.1. Ionic exchange degree

The strength of the Brønsted acid sites depends on the degree of exchange of sodium cations by the protons in the zeolite. In this sense, the higher the level of exchange, the stronger the protonic sites will be. However, in a high degree of exchange, there is not only a strong site formation, but also an increase in the strength of the protonic sites already present in the zeolite. [34]

1.2.3.2. [T-O-T] bond angle

For the Brønsted sites, the local constrains and distortions in the structure can induce vital changes in the bond strength between the proton and the bridging oxygen, and therefore in the acidity of the site. As an example, there is a relation between the acid strength and the angle of the [T-O-T] bonds. As presented by Rabo and Gadja, [26] with the increase of this angle, the sites tend to be stronger, as in the case of MOR (143–180°) and ZSM-5 (133–177°),

having stronger sites than FAU (zeolites X and Y: 138–147°) and, consequently, being more active in reactions that depend on the acidic strength of the catalyst, such as the isomerization of light alkanes.

1.2.3.3. Metallosilicates

The synthesis of metallosilicates containing trivalent elements in the framework other than aluminum, such as boron, gallium, indium, iron, can also generate very variable Bronsted acid strengths. [35, 36]

1.2.3.4. Electrostatic environment

Chaouati and co-workers, showed that an alkaline treatment of desilication on mordenite (Si/Al =10) allows the generation of extraframework aluminum (EFAl) and that this, together with silicon, induced the formation of a weak OH bridge.[37] This is related to the low presence of aluminum T- atoms adjacent to a specific acid site (Next Nearest Neighbors, NNN), increasing the number of surrounding highly electronegative silicon atoms, which weakens the OH bond, although this usually translates in an increase in acidity.

1.2.3.5. Interaction with Lewis sites

In the same study conducted by Chaouati *et al.*, it was determined that the presence of EFAl (Lewis acid sites) led to the reduction of the space close to the acid sites, and also increased the strength of Brønsted acid sites. [37] However, EFAl species may also have disadvantageous effects, as they may block the access to the active acid sites or the cations could neutralize the charge in the framework, causing a decrease in the number of Brønsted acid sites.

For Lewis acid sites, the fact that they may have numerous origins, such as extraframework aluminum species, compensating cations or other framework metal species, may contribute to the variety of acid concentrations.

1.2.4. Location of the acid sites

The location of the sites in the zeolitic lattice is also a significant factor, especially in terms of shape selectivity. In fact, if for instance a site is located in the external surface of the zeolite, it then presents smaller spatial hindrance than if that same site stands in one of the inner channels or cages. In some cases, if the reactant molecules are bulkier enough, they may not reach the vicinities of the sites, then the reaction is prevented.

A typical example is the Y zeolite that presents two very distinct types of cages: the supercages that are accessible to very bulky molecules and the sodalite cages located in the hexagonal prisms that are inaccessible to all the organic molecules.

1.3. Shape selectivity

Shape selectivity is a simple concept: the transformation of reactants into products depends on how the processed molecules fit the active site of the catalyst. [38] In zeolites, most of the active sites are located in the intracrystalline pore structure, where spatial restrictions may exist in the formation of transition or intermediate reaction states, and in the diffusion of the molecules. This diffusion in the pores depends on the size and shape of the molecules and the structure of the zeolitic pore. Consequently, zeolites can allow or reject the entry of molecules into their porosity, may hinder the formation of some intermediate molecules within them, or prevent their diffusion out.

Three types of selectivity of molecular forms are proposed, which are based on the principle of size exclusion. [39-41]

1.3.1. Reactant shape selectivity

Is encountered when bulkier molecules in a reactant mixture are prevented from reaching the active sites within the zeolite crystal. Only molecules that are small enough to enter the pore openings of the zeolite can be converted at the active sites. [42, 43] Figure III.4. represents the reactant shape selectivity.

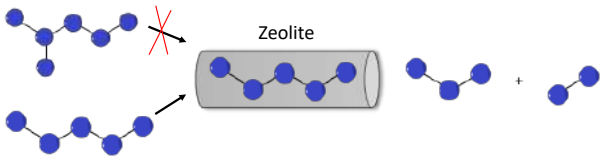


Figure III. 4 Representation of reactant shape selectivity.

1.3.2. Transition state shape selectivity

it occurs in chemical reactions that involve transition states which are too bulky to be accommodated inside the zeolite pores. In this case, products are formed only from reactions with intermediates small enough to fit inside the pores of the zeolite. In restricted transition state selectivity, neither reactants nor potential products are hindered from diffusing in or out of the zeolite crystal. [43, 44] Figure III.5. represents the transition state shape selectivity.

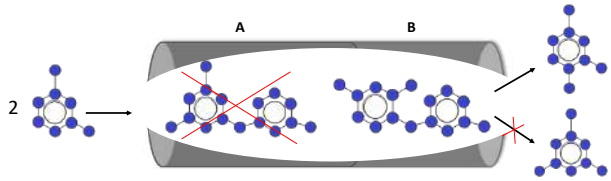


Figure III. 5 Representation of the transition state shape selectivity.

1.3.3. Product shape selectivity

It occurs when certain product molecules are too big to diffuse out of the zeolite pores (from the cages or in the larger intersections of the channels). Some zeolite structures have cavities which allow formation of both small and bulky products. However, the apertures are small, and the bulky product molecules must undergo further reactions to smaller molecules in order to leave the zeolite crystal. [42, 43] Figure III.6. represents the product shape selectivity.

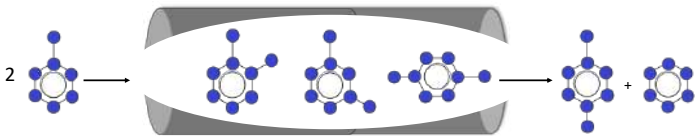


Figure III. 6 Representation of the product shape selectivity.

In general, both reactant and product shape selectivities occur due to mass transfer limitations. In reactant shape selectivity all molecules that diffuse to and from the active sites sufficiently fast will be converted, while in product shape selectivity molecules with high mass transport limitations remain in the adsorbed phase and continue to react for a longer period of time than species less affected by mass transfer limitations. Therefore, both reactant and product shape selectivities are affected by crystal sizes, whereas restricted transition state selectivity, which is not caused by mass transfer limitations, does not depend on crystal size. [43]

Another type of shape selectivity is the effect of the concentration related to the increase in the concentration of the reagents when they are inside the pores of the zeolite, which has a positive effect on the reaction rates, favoring the bimolecular reactions over monomolecular ones. [3, 10]

There are five other theories of the shape selectivity of the zeolite that are less recognized [45]: selectivity of the pore blocking/blocking key form, [46] molecular traffic control, [47] inverse form selectivity [48] and window effect [49] and nest effect. [45]

1.4. Synthesis of zeolites

Zeolites are materials that have been formed naturally and are also materials that can be synthesized in the laboratory. In both cases they are usually formed in the presence of water at moderate temperatures, although it is also possible for some examples in which water is replaced by an organic solvent, [50, 51] and there are even examples of synthesis in the absence of solvents. [52, 53] In general, zeolites are synthesized by solvothermal and more commonly hydrothermal methods. The hydrothermal synthesis of a zeolite consists in the preparation of a "homogeneous" solution of the different components of the synthesis gel that is introduced into a reactor. Then it is taken to a stove at the selected temperature and the autogenous pressure, that is, the one generated in the reactor by itself. After the set time, the product is recovered by filtration, followed by washing and drying.

The usual components of a gel in a hydrothermal synthesis are: source of silicon, aluminum, mineralizing agent and structure directing agents.

1.4.1. Silicon source

Alkoxides such as tetraethylorthosilicate, colloidal silica, sodium silicate or micronized silica, among others, can be used. The silicon source used has a decisive influence on the final result of the synthesis. [54]

1.4.2. Aluminum source

The most commonly used are aluminum oxides such as pseudoboehmite, aluminum isopropoxide or aluminum sulfate among others.

1.4.3. Mineralizing agent

The OH^- or F^- ions are responsible for mobilizing the silicon and aluminum species, providing the necessary precursors for the formation of Si-O-Al bonds. When the OH^- ion is used, the necessary pH must be higher than 10, while with the F^-, which form soluble compounds with silicon, the pH is usually lower.

1.4.4. Structure directing agents (SDA)

The structure directing agents, usually organic cations, are designed with a certain size and shape, looking for the conditions in which the SDA has a greater geometric specificity for the structure that it is desired to crystallize.

For several years, the term template was used for the use of organic cations in the synthesis of zeolites, since the notion that had these was that they helped the crystallization of the zeolite through a specific effect of filling the cavities, assuming that the size and shape of the organic cation determined in some way the size and shape of the zeolite channels. However, the direction effect may be more or less specific depending on whether or not there is a strong interaction and good correspondence between the cavities of the zeolite and the organic cation. Currently, there is a tendency to reserve the term template for cases in

which there is a great specificity in the direction effect, a strong interaction and a high correspondence of cations and cavities.

The mechanism through which the directing effect of structure by organic species takes place is not yet explicitly known. One of the main functions of organic SDA is to stabilize the microporous network through a series of interactions of different nature (Van der Waals type, electrostatic and hydrogen bonds) that contribute to the assembly of organic molecules and inorganic species. In this way, the first blocks from which the zeolite crystallizes are formed. The greater the stabilization of the SDA-zeolite system produced by the interaction in question, the more efficient the organic species will be in the direction of crystallization of the zeolitic material.

First, there are Van der Waals type interactions that are described as the sum of two terms; one attractive, proportional to $1/R^6$ and one repulsive proportional to $1/R^{12}$, where R is the distance between the interacting species. There is therefore a distance at which this interaction is maximum, and this happens the better the adjustment between the organic species and the empty volume of the zeolite in which it is occluded.

For this to happen, the size and shape of the organic species must allow a good "fit" of some molecules with others, avoiding overlaps that reduce their efficiency as SDA. Such is the case of some organic species that have aromatic rings that allow them to "package" forming supramolecular aggregates.

The electrostatic interactions, which are established between the positive charge of the organic species and the negative charge of the inorganic network, contribute at first to keep the organic species together with the first inorganic units so that nucleation can begin. Once the skeleton is formed, they provide additional stabilization to the SDA-zeolite system. [55]

Figure III.7 shows the generic scheme corresponding to the synthesis process of a zeolite. [56] This begins with a copolymerization of the silicate and aluminate ions that give rise to a gel. During the process of obtaining the zeolite, where numerous soluble species are involved

in an amorphous and crystalline phase, [57] reactions of dissolution, polymerization and depolymerization, condensation, precipitation and crystallization take place. All these facts, makes the synthesis is very susceptible to the modification of any factor that may cause some kind of physical change such as agitation during the same synthesis, the conditions used in aging and even the order and time chosen for the addition of the reagents. [58]

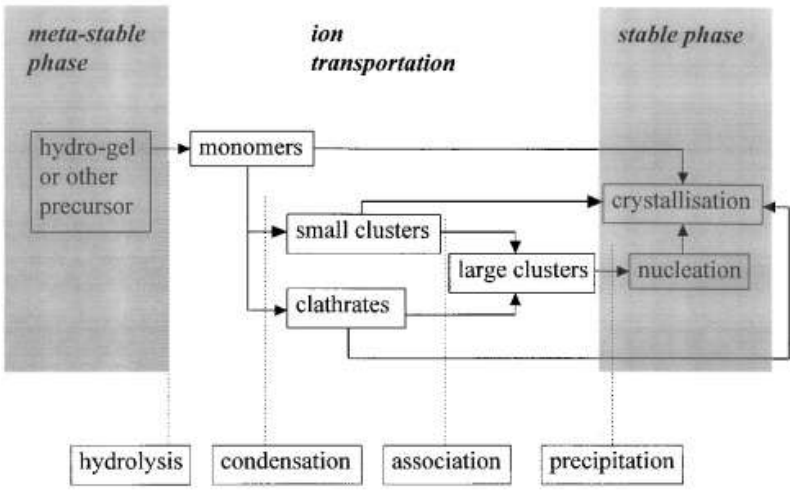


Figure III. 7 Diagram of the crystallization process of a zeolite. *Taken from* [56]

1.5. Synthesis of hierarchical zeolites

In recent studies using zeolites, it has focused on obtaining mesoporous zeolites that can retain the same properties of zeolites that are used in the industry and that do not present diffusion problems due to the small size of their pores. [59] These materials have been called zeolites with a hierarchical pore structure, that is, zeolite crystals that simultaneously contain mesoporous and interconnected micropores. [60] Many new methods of preparation of hierarchical zeolites have been discovered, which are divided into: *top-down* and *bottom-up* techniques. [59] On the one hand, *bottom-up* techniques involve the use of surfactants during the synthesis of the zeolite, in such a way that the elimination of these surfactants generates mesoporosity (or macroporosity) in the zeolite crystals, [61] Figure III.8.

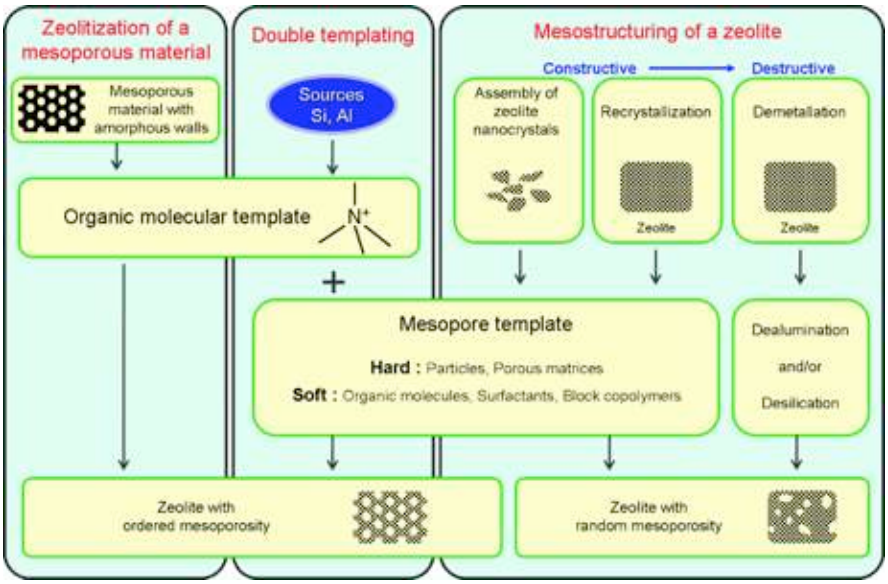


Figure III. 8 An overview of the various synthesis routes towards zeolite materials combining micro- and mesopores. *Taken from* [62]

In these techniques it is important that there is an optimal interaction between the surfactants and the zeolite precursors for the introduction of the surfactant into the structure during crystallization. If not, the segregated phase could be mixed with the zeolite precursors and form amorphous mesoporous materials composed of silicates or aluminosilicates. On the other hand, *top-down* techniques consist of subjecting the zeolites to different post-synthesis treatments to generate mesoporosity. Among the latter, it is worth highlighting the treatments in a basic medium in the presence [63] or absence of mesoporous directing agents. [64] In this way, the materials obtained have open pores that improve the accessibility of large molecules within the porous structure. In recent years, a novel technique has been developed that consists of the post-synthetic mesostructure of zeolite through the use of surfactants in a basic medium and in a single step. [65]

Figure III.9. shows the classification of the hierarchical zeolites: i) crystals of hierarchical zeolite, ii) zeolites with nanosized crystals and iii) crystals of supported zeolites. The pore size distribution associated with each type, always confirms the presence of micropores with additional meso or macropores depending on the type.

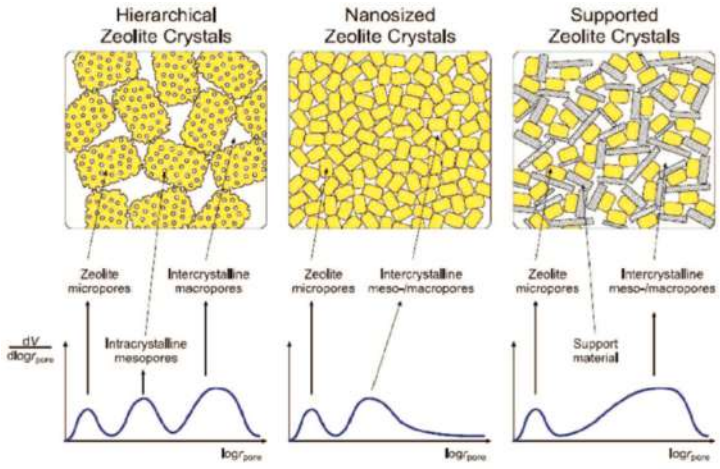


Figure III. 9 Hierarchical classification and typical pore distribution of zeolites. *Taken from* [66]

The introduction of mesopores into the zeolite crystals by *top-down* (or destructive post-synthetic treatments) can be achieved through selective extraction of atoms from the zeolitic framework. As zeolites are aluminosilicates generally, the most two studied destructive techniques are dealumination and desilication processes.

1.5.1. Dealumination

The dealumination consists in the extraction of aluminum atoms from the structure of the zeolite. It can be produced by hydrolysis of the Al-O-Si bond by thermal or hydrothermal treatment with steam at high temperatures, chemical treatment with HCl or by direct substitution of aluminum by silicon with $SiCl_4$ in the gas phase at elevated temperatures. Other less used dealumination treatments include reaction with chelating agents such as EDTA, which lead to aluminum complexation, reaction with oxalic acid, with aqueous $(NH_4)SiF_6$ or with F_2 gas. [67-71] Originally, the dealumination treatments were done to control the concentration and the strength of the acid sites by increasing the Si/Al ratio of low-silica zeolites. [62] The defects created in the structure of the zeolite during the removal of aluminum atoms are then at the origin of a partial collapse of the framework, thus generating mesopores (Figure III.10.).

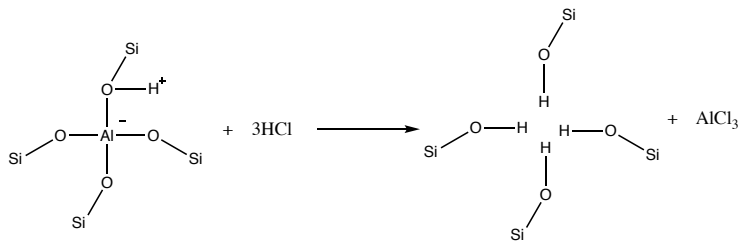


Figure III. 10 Mechanism of dealumination hydrochloric acid. *Taken from* [2]

1.5.2. Desilication

Desilication consists in the hydrolysis of the Si-O-Si bond by means of the treatment with basic medium (e.g. NaOH, Na_2CO_3, $NaAlO_2$, KOH, LiOH, etc.). This treatment allows the formation of mesoporosity while preserving the acidic properties of the zeolite (Figure III.11.).

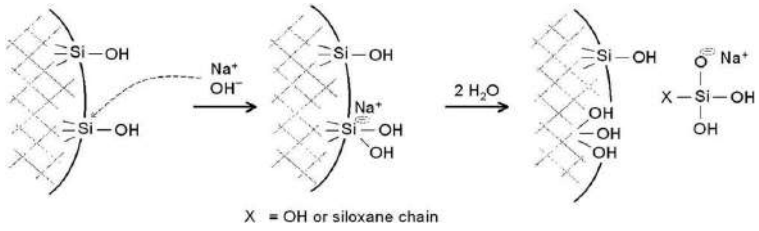


Figure III. 11 Hydrolysis of framework Si in alkaline medium. *Taken from* [72]

It has been known since long time that this technique yields lower Si/Al ratios with small changes in framework acidity. [73, 74] The desilication method can be used effectively for the introduction of mesopores when the Si/Al ratio of the parent material is in a certain range. At lower molar ratios Si/Al a limited formation of mesopores is observed, since the high concentration of Al atoms prevents the extraction of silicon, while at higher Si/Al molar ratios (lower Brønsted acidity) an uncontrolled silica extraction is observed producing the formation of large pores (Figure III.12).

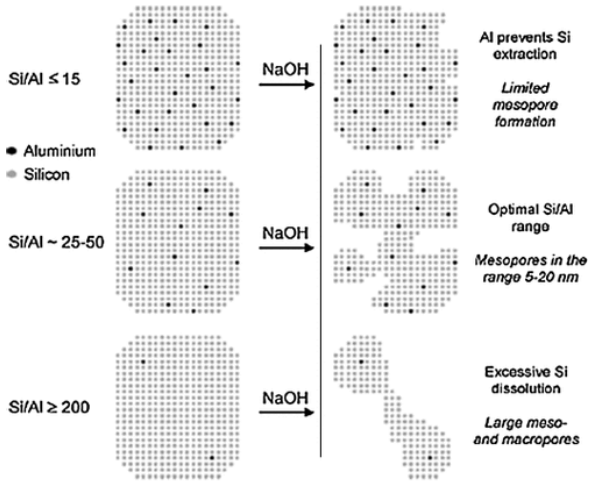


Figure III. 12 Diagram of the influence of the content of Al in the treatment of desilication by treatment with NaOH. *Taken from* [62]

During the alkaline treatment also the dissolution of part of the Al of the zeolite takes place, generating an amorphous phase outside the structure. This amorphous alumina can partially block the pores of the zeolitic structure, therefore, it is necessary to perform an acid wash to eliminate it and unblock the microporosity. In addition, a characteristic of the alkaline treatment is the reduction of the Si/Al ratio due to the partial dissolution of the silica, which can be partially recovered, by performing the acid treatment after the alkaline in order to eliminate the amorphous alumina formed during the first step. [75]

On the other hand, the constructive techniques (*bottom up*), allow the hierarchization through the use of three types of structuring agents: templates, structure-directing agents, and species filling porosity (space-fillers) during the synthesis. [76] In recent years, great progress has been made in the synthesis and characterization of hierarchical zeolites that comprise the structured mesoporosity obtained through constructive methods. However, the high amounts of the organic materials used in such synthesis approaches, and consequently their high cost, is a real problem as it marks a major drawback on a large industrial scale. The high operating conditions associated with presence of large quantities of organic molecules used, are considered highly inconvenient and may be behind the

release of effluent gases that may cause environmental problems. In addition to detrimental effect on the final framework structure caused by high applied temperatures. These concerns get in the way of the eventual industrializing of the constructive synthesis methods, and, consequently, their effective application in industry is somehow limited. [62] Table III.1. summarizes the advantages and disadvantages associated to the destructive and constructive approaches towards hierarchical zeolites synthesis.

Table III. 1 Summary of the advantages and disadvantages of the destructive and constructive synthesis approaches for mesoporous zeolite materials. [62]

	Formation route	Production cost	health/safety/environment issue	Hydrothermal stability	Flexibility in Si/Al
Destructive	Dealumination	Low	No	High	Medium
	Desilication	Low	No	High	Little
Constructive	Zeolitization of mesoporous material	High	Yes	Low	Medium
	Soft templating	Medium/High	Yes	Medium/High	Yes
	Hard templating	High	Yes	High	Yes
	Mesostructuring of zeolites	High	Yes	Medium/High	Yes

1.6. Zeolites in nanocrystals and their synthesis

The high interest in the nanosized porous materials at the beginning of the new millennium is a part of the revolution in the nanotechnology. It is known that the driving force for many processes is the local environment of atoms exposed at solid surfaces compared to that in the bulk. [77] Therefore, in order to increase the number of surface atoms in the solids, two main approaches are applied: (a) decrease the size of dense particles or (b) create an open pore network within the bulk solid. The combination of these two approaches leads to the formation of nanosized zeolites with accessible and uniform pores. [78] The zeolite nanocrystals have several properties, as shown in Figure III.13.



Figure III. 13 Different properties of nanometric zeolites. *Taken from* [78]

The main methods to obtain crystals of zeolites in nanometric sizes are: (i) synthesis from clear precursor suspensions in the presence of organic template, (ii) low temperature synthesis from highly alkaline organic-template-free hydrogels, and (iii) alternative methods including ionothermal, seed-induced and confined space synthesis. [79-81]

1.6.1. Synthesis from clear precursor

The method of synthesis of nanozeolites by means of "clear solution" is based on the principle that, in the absence of gel, the confluence of the nuclei between them is at a disadvantage, which inhibits their condensation. This absence of gelling is obtained with a high molar ratio of water/sodium hydroxide. The temperature of hydrothermal synthesis is generally moderate. [82-85]

1.6.2. Synthesis from strongly alkaline gels

Another form of synthesis of zeolite nanocrystals is to work at low molar ratios of water / sodium hydroxide and in the absence of structuring agent. The kinetics of nucleation accelerate strongly, so it takes precedence over the crystalline growth stage. [86-88] Comparing with the "clear solutions" method, in this method the hydrothermal processes require shorter times and lower temperatures.

1.6.3. Alternative methods

The use of porous matrices in the synthesis of zeolites has the objective of imposing a maximum size, of the same order of magnitude as the diameter of the pores of the matrix, where the forming crystals undergo steric stress. [89-91]

2. Zeolites as catalysts in the etherification of glycerol with *tert*-butyl alcohol

Reports in which zeolites have been used in the etherification of glycerol with *tert*-butyl alcohol (TBA) are relatively few. Historically, the use of zeolites in this reaction, was born timidly with the Klepáćová and co-workers study, [92] where they discovered that the catalytic activity of large pore zeolites, such as HY and H-BEA, can make an alkylation of glycerol, as does Amberlyst® 15; Two years later, the same authors published a more developed work comparing the same zeolites (HY and H-BEA) with the ion exchange resins, Amberlyst® 15 and Amberlyst® 35. [93] They conclude that glycerol conversion and selectivity to di-*tert*-butyl ether glycerol, are higher when acid resins are used, without giving too much relevance to zeolites. Selectivity to DTBG achieved with zeolites was around 25%, and TTBG was not detected when using these catalysts. This was attributed to steric hindrance effects because of the microporosity of the zeolites

In 2013, Gonzales *et al.*, [94] carried out the etherification of glycerol with TBA at 348 K, in three commercial acid zeolites: * BEA, MOR and MFI with respective Si/Al molar ratios of 10, 6.5 and 20. the authors showed that the *BEA zeolite allowed to achieve the highest conversion (75% with catalyst loads of 5% by weight) for this transformation, which was confirmed by the previous studies of the Klepáćová group. A year later, Gonzalez *et al.*, [95] showed that these results could be improved and its activity can be further improved by post-synthetic modifications, such as desilication (using alkaline agents) and fluorination treatments.

In 2016, Simone *et al.*, [96] synthesized MFI based nanosponge and nanosheet, featuring structured hierarchical systems of connected pores on different length scales. The authors

observed, that the hierarchical catalysts are both more active and selective towards the formation of higher substituted ethers compared to the purely microporous ones.

The same year (2016) Manjunathan and co-workers [97] used zeolites (H-ZSM-5, H-Y and H-BEA) to compare the catalytic activity with a sulfonic acid functionalized mesoporous polymer. Medium pore zeolite H-ZSM-5 gave lower glycerol conversion (10%) which is mainly attributed to the diffusion limitation of molecules due to pore size restriction. Large pore zeolites namely H-Y and H-beta showed higher glycerol conversion (59 and 77 % respectively) and h-GTBE selectivity compared to medium pore zeolite H-ZSM (28, 33 % for H-Y and H-BEA respectively and 0% with H-ZSM-5).

Considering that in the literature there are few studies in which the use of zeolites in the etherification of glycerol with *tert*-butyl alcohol reaction is completely detailed, the following section shows the motivation and the objective of this section of the thesis.

3. Motivation of the use of zeolites in the etherification of glycerol with *tert*-butyl alcohol

The location of protonic sites within the pore system influences the catalyst activity, selectivity and stability. This is particularly the case with zeolite materials where the size of micropores is often close to those of reactant(s), product(s) and reaction intermediate(s), which is at the origin of what is referred as molecular shape selectivity (MSS). MSS results from constraints arising from the interaction of molecules or intermediates within the zeolite channels or cages of molecular size. [39, 98] Reactant or product selectivity can be observed when reactant or product molecules diffuse at very different rates within the zeolite micropores as a function of their sizes. Moreover, the formation of bulky transition states can be limited or inhibited within cages or channel intersections (restricted transition state selectivity). Despite, these constraints positive interactions (such as confinement, solvation [99]) can further occur between reactant and intermediate molecules and the intracrystalline zeolite pore volume, which affect the rates of catalytic reactions. Therefore, the differences

in activity of zeolite catalysts can result from the solvating characteristics of their channels, channel intersections and cages.

4. Objective of the use of zeolites in the etherification of glycerol with *tert*-butyl alcohol

To evaluate the impact of the zeolite voids and void interconnections on the activity, selectivity and stability of the liquid phase glycerol etherification with *tert*-butyl alcohol. For this purpose, different types of acidic catalysts: Amberlyst® 15, silica, alumina, silica alumina and four series of zeolites: MOR, FAU, *BEA and MFI structure type (Figure III.14) with different Si/Al molar ratio, morphologies and crystal size ranging from few nanometers to several micrometers, were compared.

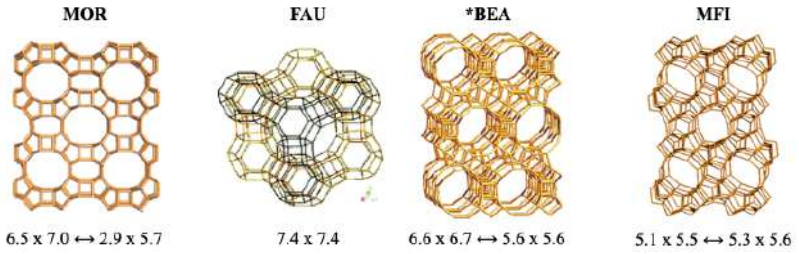


Figure III. 14. Structures of the zeolites studied.

5. Experimental section

5.1. Chemicals and catalysts

The reagents glycerol (99%) and *tert*-butyl alcohol (99.4%) were obtained from Acros Organics. Table III.2., shows the catalysts used, the origin and, in the case of zeolites are designated as follows: the type of zeolite is indicated in brackets by using the IZA structural code, the range of crystal size is in subscript, i.e., MC, SC, NC for micrometer, sub-micrometer, nanometer-sized, and NSp, NSh for nanosponge and nanosheets morphologies, respectively. The bulk Si/Al molar ratio is in superscript (the Si/Al radius and the crystal size determination are based on the results that will be shown later). For the mordenite and H-ZSM-5 catalysts, "d" indicates a desilication process, the values in

brackets are sodium hydroxide concentration (M) and temperature (K) used for alkaline treatment; "a" indicates a subsequent acid treatment.

Table III. 2 Catalysts used and their origin where C: commercial, S: synthetized, M: modified.

	Catalyst	Origin	Supplier	Reference
	A-15	C	Acros-Organics	9037-24-5
	SiO_2	C	Sigma-Aldrich	242179
	Al_2O_3	S		
	SiO_2-Al_2O_3	S		
MOR $\mathbf{H_xAl_xSi_{48-x}O_{96}}$	$(MOR)^{10}_{SC}$	C	Sud-chemie (Clariant)	T-4545
	d(0.4/358)-a-$(MOR)^{10}_{SC}$	M		
FAU $\mathbf{H_xAl_xSi_{192-x}O_{384}}$	$(FAU)^{2.6}_{MC}$	C	Zeolyst	CBV500
	$(FAU)^{17}_{MC}$	C	Zeolyst	CBV720
	$(FAU)^{40}_{MC}$	C	Zeolyst	CBV780
***BEA** $\mathbf{H_xAl_xSi_{64-x}O_{128}}$	$(*BEA)^{14}_{MC}$	S		
	$(*BEA)^{15}_{MC}$	S		
	$(*BEA)^{9}_{SC}$	S		
	$(*BEA)^{10}_{SC}$	S		
	$(*BEA)^{12}_{NC}$	C	PQ Zeolites B.V.	CP811 BL-25
	$(*BEA)^{15}_{NC}$	S		
	$(*BEA)^{17}_{NSp}$	S		
MFI $\mathbf{H_xAl_xSi_{96-x}O_{192}}$	$(MFI)^{40}_{MC}$	C	Zeolyst	CBV8014
	d(0.4/338)-$(MFI)^{40}_{MC}$	M		
	$(MFI)^{45}_{NC}$	C	Clariant	HCZP90
	$(MFI)^{45}_{NSh}$	S		
	$(MFI)^{20}_{NSp}$	S		

The process used for the synthesis and / or modification of the catalysts is described in annex A.

5.2. Characterization

The details of the equipment, the preparation and/or the treatment of the sample to perform the respective characterization are shown below. The principle of each technique of interest for this study was detailed in the first chapter of this document.

5.2.1. Chemical composition

X-ray fluorescence spectrometry (XRF): The analyzes were carried out in a PHILIPS MAGIX type device. The samples were prepared as pellets by compacting approximately 200 mg of zeolite powder using a press (applying a pressure of 2 tons for a few minutes).

Inductively coupled plasma emission spectrometry (ICP-OES): The analysis was performed on an argon plasma using a Perkin-Elmer OPTIMA 2000DV spectrometer. The sample is dissolved in aqua regia and then vaporized with a plasma to measure the emission intensity of a radiation characteristic of the element to be analyzed. The uncertainty of the measure is 2%.

5.2.2. Composition of the surface

X-ray Photoelectron Spectroscopy (XPS): The XPS analysis is performed using an AXIS Ultra DLD KRATOS spectrometer. The photoelectron spectra are obtained using a monochromatic Al Kα source (1486.6 eV), which operates at 150W (10 mA, 15 kV). The pressure in the analysis chamber during the measurements is 9.0×10^{-8} Pa. The charge neutralizer is used for all measurements to compensate for the accumulation of positive charges from the insulating samples. The spectra were recorded with a constant pass energy of 160eV. The binding energy of the reference taken in this study is the core Si2p (103 eV). The composition and the elements in contact on the surface of the sample are analyzed according to the binding energies of Si2p and Al2p. The decomposition of the high-resolution spectra is done using the CasaXPS software.

5.2.3. Determination of the Si/Al ratio of the zeolite framework

Nuclear magnetic resonance (NMR) of the solid: The ^{27}Al MAS (Magic Angle Spinning) NMR spectra were recorded at room temperature on a BRUKER ADVANCE II 400 MHz spectrometer according to the conditions described in Table III.3.

Table III. 3 Analysis conditions of NMR spectra.[107]

	^{27}Al MAS
Chemical reference	Chlorosodalite
Frequency (MHz)	104.28
Pulse duration (μs)	0.42
Pulse angle	π/12
Contact time (ms)	/
Recycling time (s)	0.58
Rotation speed (kHz)	4
Number of scans	100000

Infrared spectroscopy of the structure bands (IR Region 300 to 1300 cm^{-1}): The infrared spectra were carried out using a NICOLET MAGMA Fourier transformation apparatus (750 spectrometer). The sample holder is installed in a glass measuring cell. The catalyst is formed in a tablet of 10 to 20 mg of surface area of 2 cm^2 (the measurement is made in the sample diluted to 5% in KBr). Then it is entered into the measurement cell.

Example: the number of framework aluminium atoms, N_{Al}, and the Si/Al structure ratio of zeolite *BEA were determined by equations 1 and 2. [107,108]

$$\mathbf{N_{Al}} = \frac{1099-\upsilon}{3{,}3369} \qquad \text{(Eq. 1)}$$

With:

N_{Al}: is the number of framework aluminium atoms,

υ: is the wave number (cm^{-1}) close to 1090 cm^{-1} (Figure III.15).

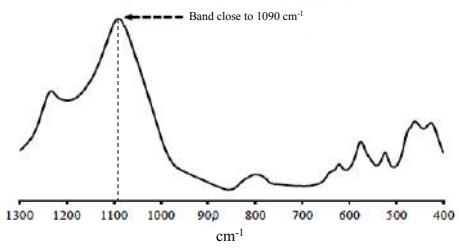


Figure III. 15 Structural bands of * BEA zeolite

$$\frac{\mathbf{Si}}{\mathbf{Al}} = \frac{64 - N_{Al}}{N_{Al}} \qquad \text{(Eq. 2)}$$

5.2.4. Determination of the framework formula

The formula of the framework can easily be deduced from the chemical composition of the zeolite and the structure of Si/Al ratio, provided that certain simplifying assumptions are made about the nature of extra-framework species and the composition of the structure. These simplifying assumptions depend in part on how the sample is prepared. In all cases, it is generally assumed that: all the Si atoms are located in the frame, the Al atoms can be either in the frame or outside the frame (EFAl); and that all cations are in exchange position.

Example: the calculation for determining the composition of the elementary cell of an H-*BEA zeolite is presented below (*Taken from* [107]):

- *Experimental data:*

  FLUOX (% by weight): Si: 44.5 ; Al: 2.48 ; Na: 0.088 ; O: 52.5

  Si/Al atomic ratio of framework 22 (determined by NMR and IR)

- *Solution:*

  framework formula without EFAl:

  N_T: is the total number of atoms Al and Si in an elemental cell of zeolite

  ***BEA**

$N_T = N_{Al} + N_{Si} = 64 = N_{Al} + 22\ N_{Al} = 23\ N_{Al}$ where $N_{Al} = 2,8$ and $N_{Si} = 61,3$

$N_{Na}/N_{Si} = 0,002$; $N_{Na} = 61,3 \times 0,002 = 0,1$;

$N_{H^+} = N_{Al} - N_{Na} = 2,7$

Result $H_{2,7}\ Na_{0,1}\ Al_{2,8}\ Si_{61,3}\ O_{128}$

Number of EFAl per framework:

$(Si/Al)_{total} = 17,3$; Total number of Al per framework = 61,3/17,3= 3,5

$N_{EFAl} = 3,5 - 2,8 = 0,7$

Result $H_{2,7}\ Na_{0,1}\ Al_{2,8}\ Si_{61,3}\ O_{128}$ 0,7 EFAl

To calculate the mass of the framework and estimate the theoretical concentration at the protonic acid sites, it is generally accepted that EFAl is in the form of Al_2O_3.

$M_{frame} = 3942\ g.mol^{-1}$

$C_{H^+} = 2,7/3942 = 685\ \mu mol.g^{-1}$

5.2.5. Structural analysis

X-ray diffraction (XRD): The X-ray diffractograms were recorded at room temperature in a fixed-slot X'PERT PRO (PANalytic) diffractometer using the Kα copper line (λ = 1.5418 Å) at a voltage of 50 KV and an intensity of 40 mA. The measurements were made in a Bragg-Brentano mode configuration in an angular range 2θ that varies from 3 to 50 degrees in steps of 0.017 degrees and with a counting time of 1.81 seconds per step. The samples studied were pressed in the form of pellets in a stainless-steel sample holder (for measurements at large angles ($5 < 2\theta < 50$ degrees) or extended as thin films on glass plates (for measurements at small angles ($0.5 < 2\theta < 5$ degrees).

5.2.6. Morphology

Scanning electron microscopy (SEM): The sample is first sieved to homogenize the size. he average size is then evaluated using a Philips XL 30 FEG microscope. The samples to be analyzed are deposited on a double-sided conductive adhesive and then covered with a thin layer of gold (10-20 nm) by sputtering. The samples are then placed in the SEM chamber. The vacuum is less than 2.0 $x10^{-5}$ bar, the electron beam voltage varies from 5 to 15 kV and the intensity is about 130 μA.

Transmission electron microscopy (TEM): The photographs obtained were made at room temperature on a FEI-PHILIPS CM200 device equipped with a thermionic gun, LaB6 filament. This microscope reaches a resolution of 0.3 nanometers. The samples must have a thickness of less than 100 nm obtained by grinding or ultramicrotomy. They are dispersed in a solvent. A drop of the suspension obtained is deposited on a copper grid covered with a carbon layer.

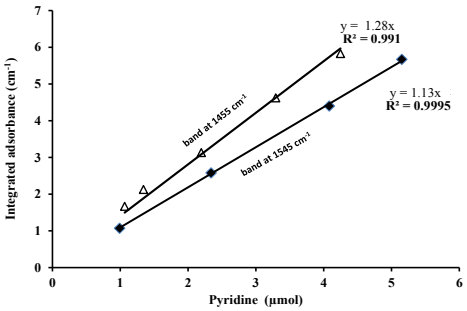
5.2.7. Textural properties

Nitrogen adsorption-desorption: The textural properties were evaluated by nitrogen adsorption at 77 K on a MICROMERITICS ASAP 2420 MP apparatus over a wide pressure range (1.0 $x10^{-7}$ to 1 Bar) on calcined samples. Before the nitrogen adsorption analyzes, the samples are degassed under vacuum at 363 K. for 1 h and then at 573 K for 15 h in order to eliminate all the adsorbed species, in particular the physisorbed water.

5.2.8. Acidity

Pyridine thermodesorption followed by infrared spectroscopy: Fourier transform Infrared spectra (FT-IR) of pyridine adsorbed samples were recorded on a Nicolet Magna 550-FT-IR spectrometer with a 2 cm^{-1} optical resolution. The zeolites were first pressed into self-supporting wafers (diameter: 1.6 cm, ≈ 20 mg) and pretreated from room temperature to 723 K (heating rate of 1.5 K min^{-1} for 5 h under a pressure of 1.33 10^{-4} Pa) in an IR cell connected to a vacuum line. Pyridine adsorption was carried out at 423 K. After establishing a pressure

of 133 Pa at equilibrium, the cell is evacuated at 623 K to remove all physisorbed species. The amount of pyridine adsorbed on the Brønsted (BAS) and Lewis (LAS) sites is determined by integrating the band areas at respectively 1545 cm^{-1} and 1454 cm^{-1} and using the following extinction coefficients measured at 293 K: ε_{1545} = 1.13 and ε_{1454} = 1.28 cm mol^{-1} (Calibration curves in the Figure III.16.). It is worth mentioning that the values of the integrated molar extinction coefficients are close to those found by Dwyer *et al.*, [109] and differ from the typically applied values presented by Emeis [110] (*i.e.* ε_{1545} = 1.67 and ε_{1445} = 2.22 cm mol^{-1}). The difference is due to the temperature at which the spectra were recorded. In this thesis and that presented in reference [109], they were reordered at 293 K, whereas in the publication of Emeis at 423 K. According to Shi and Zhang [111] and Bauer *et al.*, [112] the temperature dependence of extinction coefficient is represented by a simple power law: $\varepsilon = \varepsilon(T_0)\left(\frac{T}{T_0}\right)^A$, where A is the temperature exponent and T_0 the reference temperature. It is thus important to ensure for the accurate quantification of BAS and LAS that spectra are recorded at same temperatures used for the determination of molar extinction coefficients.



The calibration curves were obtained by adding to the IR cell a known amount of pyridine vapor from a gas admission compartment (0.9122 cm^3). The spectrums were recorded at 293 K.

Figure III. 16 Molar extinction coefficient of Brønsted acid sites (band at 1545 cm^{-1}) and Lewis acid sites (1455 cm^{-1}).

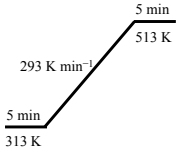
5.3. Glycerol etherification with *tert*-butyl alcohol

Etherification experiments were performed in a batch reactor: a glass stirred autoclave (15 mL) equipped with a temperature controller and a pressure gauge, Figure III.17.



Figure III. 17 Reactor used for etherification of glycerol with *tert*-butyl alcohol reaction.

For the etherification of glycerol with *tert*-butyl alcohol, the composition of the reaction mixture was: 2.79 g (3.0×10^{-2} mol) of glycerol, 9.00 g (1.2×10^{-1} mol) of *tert*-butyl alcohol (glycerol/*tert*-butyl alcohol molar ratio of 0.25) and constant catalyst loading of 7.5wt% (referred to glycerol mass). Stirring was fixed for all experiments to 1200 rpm to avoid external diffusion limitations. Zeolites were activated before testing at 473 K under reduced pressure during 12 h and the Amberlyst® 15 was washed with methanol and dried in vacuum at 333 K. The reaction temperature was fixed at 363 K and samples were taken at different times for 10 h under autogenous pressure, which can reach up to 5 bar. The reaction products were analyzed by gas chromatography using a chromatograph model Agilent Technologies 7820A equipped with an auto-sampler G4567A, DB-WAX column and an FID detector and butanol (Sigma Aldrich) as internal standard. The analyzes were performed using the following temperature program:



Glycerol, MTBG (3-*tert*-butoxy-1,2 propanediol and 2-*tert*-butoxy-1,3 propanediol) and DTBG (2,3-di-*tert*-butoxy-1-propanol and 1,3-di-*tert*-butoxy-2-propanol) response factors were determined by calibration performed with standards. MTBG and DTBG, which were not available commercially, were isolated from the products of the etherification reaction by column chromatography (1:9 Ethyl Acetate/petroleum ether) and identified by ^{1}H-NMR.

The ^{1}H NMR spectra were performed at 400 MHz using $CDCl_3$ as solvent, with a chemical shift (δ) referenced to internal $CDCl_3$ standard of 7.26 ppm, annex B.

Glycerol conversion (%), product selectivity (%) and the molar yield (%), were calculated using the following equations:

$$\text{Glycerol conversion (\%)} = \frac{\text{glycerol converted moles}}{\text{initial moles of glycerol}} \qquad \text{(Eq. 3)}$$

$$\text{Product selectivity (\%)} = \frac{\text{moles of obtained product}}{\text{total moles of product}} \qquad \text{(Eq. 4)}$$

$$\text{Molar yield (\%)} = \frac{\text{moles of obtained product}}{\text{initial moles of glycerol}} \qquad \text{(Eq. 5)}$$

The carbon balance with respect to glycerol was close to 97% for all the catalysts except with γ-Al_2O_3, which was lower than 90%.

5.3.1. Catalyst regeneration and catalytic recycling

After stopping reactions, catalysts were separated from reaction medium by centrifugation and spent catalysts were rinsed with 55.8 mL ethanol at 373 K under 10 MPa nitrogen pressure during 14.5 min using a Dionex ASE 350. The recovered rinsing solution was concentrated by evaporation on a rotavap and characterized by gas chromatography. The amount of confined organic molecules (after rinsing) was inferred through thermogravimetric analysis. Rinsed catalysts were used directly or after calcination (773 K/8 h) in catalytic recycling experiments by applying the protocol described above.

6. Results and discussion

This section is divided into two parts. The first shows the results of the characterization of the catalysts and the second part, deals with the influence of the catalysts on the glycerol etherification with *tert*-butyl alcohol.

6.1. Characterization of catalysts

6.1.1. Chemical composition and Si/Al ratio

Table III.4. shows the molar proportions of silicon and total aluminum of the zeolites, in the frame and the Extra-framework aluminum.

Table III. 4 Si/Al ratio, frame and aluminum Extra-framework.

Catalyst	Si/Al		EFAl[c]
	Tot.[a]	Fra.[b]	Atom per cell
A-15	/		
SiO_2			
Al_2O_3	/		
SiO_2-Al_2O_3	20		
$(MOR)^{10}_{SC}$	10	11.6	0.6
d(0.4/358)-a-$(MOR)^{10}_{SC}$	9.8	10.9	0.4
$(FAU)^{2.6}_{SC}$	2.6	3.9	19.6
$(FAU)^{17}_{SC}$	17	16	0.4
$(FAU)^{40}_{SC}$	40		
$(*BEA)^{15}_{MC}$	15	17	0.5
$(*BEA)^{9}_{SC}$	9	17	3.1
$(*BEA)^{10}_{SC}$	10	13	1.4
$(*BEA)^{12.5}_{NC}$	12	15	1.0
$(*BEA)^{15}_{NC}$	15	23 (21)	1.4
$(*BEA)^{17}_{NSp}$	17	22 (23)	0.8
$(MFI)^{40}_{MC}$	40		
d(0.4/338)-$(MFI)^{40}_{MC}$	42		
$(MFI)^{45}_{NC}$	45		
$(MFI)^{45}_{NSh}$	45		
$(MFI)^{20}_{NSp}$	20		

a. XRF analysis; b. estimated to TOT band at 1080-1200 cm^{-1} using the correlation given in ref. [108] or by ^{27}Al and ^{29}Si NMR (in parenthesis), c. Extra-framework Aluminum calculated from b and c.

The total Si/Al ratio is measured by X-ray fluorescence spectrometry. For some samples, the value obtained was verified and confirmed by inductive plasma spectrometry.

The Si/Al ratio of the framework is calculated using a correlation that provides the aluminum frame number from the position of the structure band to approximately 1090 cm^{-1}. This indirect method, which is fairly easy to use, is validated by measurements obtained using a more complex technique that is ^{27}Al NMR. In fact, it is known that aluminum NMR is used to identify and quantify the different coordination states of this nucleus. The NMR spectra of the aluminum of the various modified beta-zeolites have two signals, one of which is characteristic of the resonance of the tetracoordinated aluminum atoms and the other is characteristic of the resonance of the hexacoordinated aluminum atoms. Al (IV) tetracoordinated aluminum atoms resonate at a chemical change of +60 ppm and the hexacoordinated aluminum atoms of Al(VI) resonate at a chemical change of 0 ppm. The percentage by weight of the two aluminum species Al(IV) (intra-reticular aluminum located within the framework of the zeolite) and Al(VI) (extra-reticular aluminum) is quantified by integrating the signals corresponding to each of these species. The quantitative analysis of each of these two families allows to calculate the relationship of the Si/Al network and determine the number of extra-framework aluminum (EFAl) per zeolite frame. The extra-framework aluminum number can also be calculated from the total Si/Al ratios and the frame.

6.1.2. Structural results of zeolites

Figure III.18., shows the X-ray diffractograms of the zeolites that were synthesized and/or modified; for the mordenite, it can be observed that after the basic treatment and then an acid treatment, there is a conservation of the crystalline structure. In addition, the desilication causes a decrease in crystallinity (deduced from the ratio of the areas of the diffraction peaks of the modified zeolites and the original zeolite taken as reference) of about 25%.

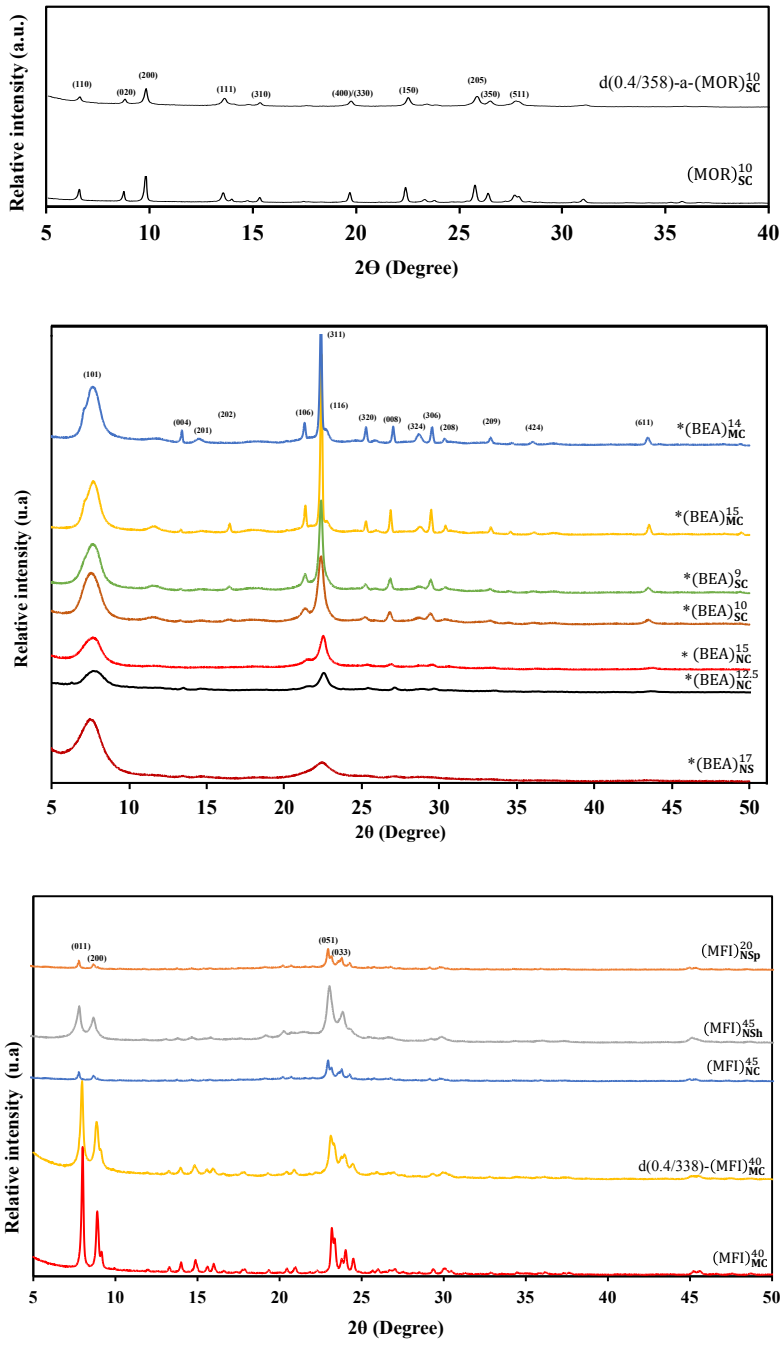


Figure III. 18 X-ray diffractograms for synthesized or modified zeolites.

For the Beta zeolite, it can be seen that all the diffraction peaks obtained for the different crystal sizes are indexable and characteristic of *BEA. It should be noted that the NC and NSp samples show both a widening and, at the same time, a decrease in the maximum

intensities compared to the larger crystal size samples, characteristic of these materials; this same effect occurs for MFI.

6.1.3. Morphology of the zeolites

Figure III.19 compares the SEM and TEM images of the MOR, FAU, *BEA and MFI-type zeolites. TEM image of $(MOR)^{10}_{SC}$ shows crystals with a length ranging from 100 to 500 nm and the alkaline treatment (d(0.4/358)-a- $(MOR)^{10}_{SC}$ yields to a lot of intracrystalline mesopores. SEM image of $(FAU)^{2,6}_{SC}$ displays large crystal (600 < ø <1000 nm) with a bipyramidal shape, and the TEM micrograph of $(FAU)^{17}_{SC}$ shows also large crystals (ø = 500 nm). SEM image of the $(*BEA)^{15}_{MC}$, exhibits a truncated bipyramidal shape with crystal sizes ranging from 6000 to 10000 nm. The crystals of $(*BEA)^{9}_{SC}$ with a size ranging from 300 to 1500 nm are aggregated. The $(*BEA)^{10}_{SC}$ sample, synthesized in alkaline medium at 423 K, consists on crystals with a smaller diameter (100–700 nm). Pseudo-spherical crystals with an average size of 40 nm are present for $(*BEA)^{15}_{NC}$; the aggregation of the nanocrystals yields into the formation of intercrystalline mesospores. *BEA-type zeolite synthesized from a polyquaternary ammonium surfactant exhibits a sponge-like morphology.[104] These nanosponges are formed by randomly aggregated nanoparticles delimited by ordered mesoporous channels. The corresponding TEM image reveals nanometer-sized *BEA units with a low thickness (2 nm) separated by narrow channels with a width of few nanometers. The $(MFI)^{40}_{MC}$ zeolite have crystals with a diameter of 250 nm, and a desilication treatment on this zeolite yields to intracrystalline mesopores (d(0.4/338)-$(MFI)^{40}_{MC}$). For $(MFI)^{45}_{NC}$ sample, the replacement of the conventional template (TPAOH) by a bifunctional organic compound generates the production of lamellar materials that are called nanosheets. [105] The overall thickness of the lamellar stacking of nanosheets was about 20-40 nm. The thickness of each nanosheet was 2 nm. [105] The increase of the carbon chain length and the number of quaternary ammonium of the used structuring agent ($C_{18\text{-}6\text{-}6\text{-}18}$) lead to nanosponge morphology (*sample* $(MFI)^{20}_{NSp}$). The morphology of nanosponges was spiky nanomaterials (composed of nanocrystals with a crystal size ranging from 3.7 to 4.6 nm) that are uniform

in size and shape as shown from SEM and TEM image in Figure III.19. Table III.5. summarizes all the sizes obtained for the zeolites.

Table III. 5 Crystal sizes of the zeolites.

Catalyst	Crystal size nm
$(MOR)^{10}_{SC}$	500-100
d(0.4/358)-a-$(MOR)^{10}_{SC}$	500-100
$(FAU)^{2.6}_{MC}$	1000-600
$(FAU)^{17}_{MC}$	500
$(FAU)^{40}_{MC}$	
$(*BEA)^{14}_{MC}$	10000-6000
$(*BEA)^{15}_{MC}$	10000-6000
$(*BEA)^{9}_{SC}$	1500-300
$(*BEA)^{10}_{SC}$	700-100
$(*BEA)^{12}_{NC}$	20
$(*BEA)^{15}_{NC}$	40
$(*BEA)^{17}_{NSp}$	2-4
$(MFI)^{40}_{MC}$	250
d(0.4/338)-$(MFI)^{40}_{MC}$	< 250
$(MFI)^{45}_{NC}$	20-50
$(MFI)^{45}_{NSh}$	2
$(MFI)^{20}_{NSp}$	3.7-4.6

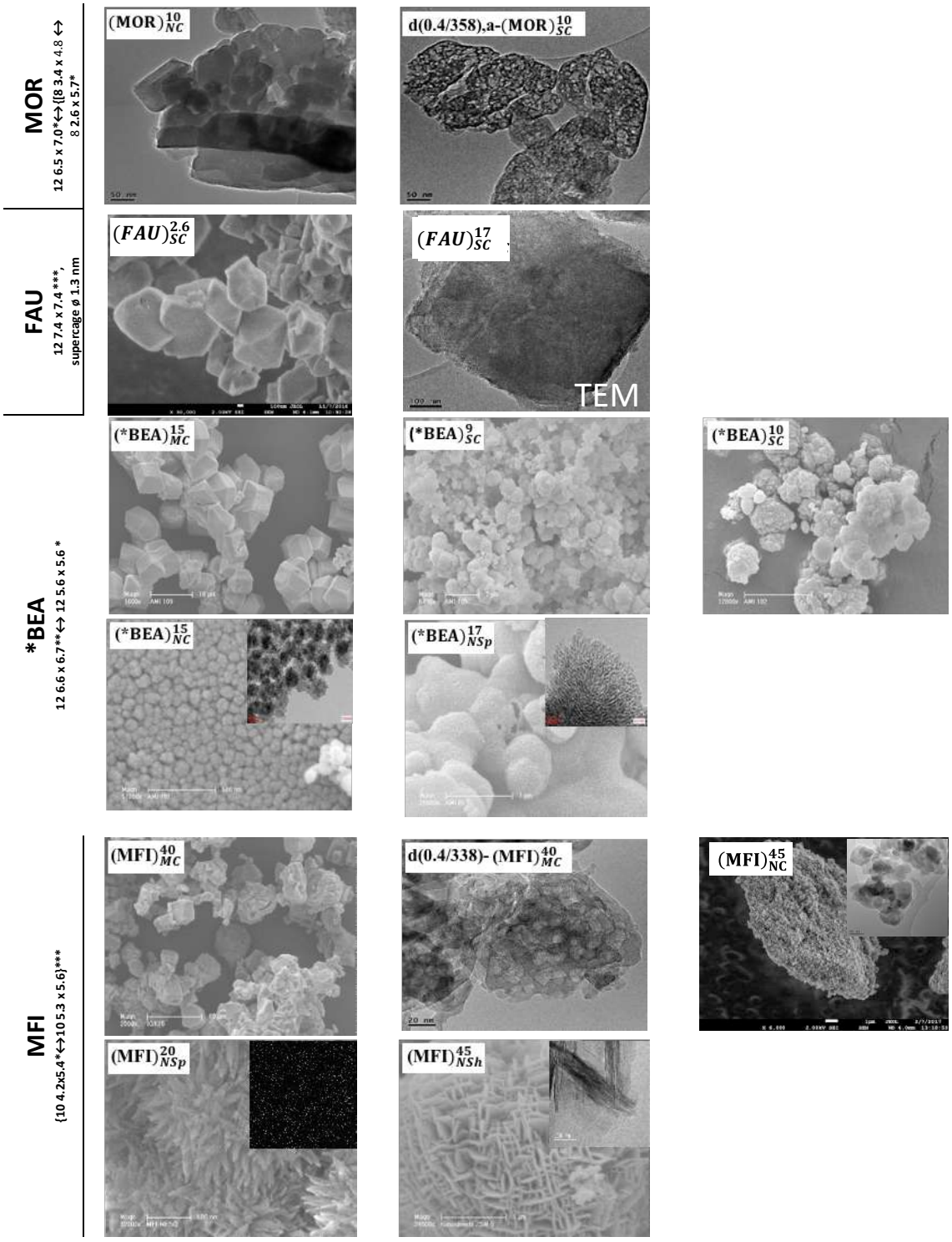


Figure III. 19 Scanning electron microscopy and transmission electronic images of commercial, modified and synthesized zeolites.

6.1.4. Textural results of zeolites

For mordenite, the N_2 adsorption/desorption isotherm of zeolite $(MOR)^{10}_{SC}$ has an isotherm type I (characteristic of a microporous material). However, there is a hysteresis at a high relative pressure ($p/p_0 > 0.9$), which corresponds to a mesoporosity created by the agglomeration of the crystallite. [113] On the other hand, a desilication treatment with 0.4 M NaOH and 358 K is sufficient to generate a low p/p_0 hysteresis (> 0.4). This hysteresis reflects the presence of mesopores, Figure III.20a.

With respect to the results of the series of beta zeolites, in the nitrogen isotherm of zeolite $(*BEA)^{15}_{MC}$, Figure III.20b, rapid increase in the amount of nitrogen adsorbed as a plateau is observed. According to IUPAC, this adsorption isotherm corresponds to type I. This zeolite is a purely microporous material with a volume of ~0.22 cm^3g^{-1}. The $(*BEA)^{9}_{SC}$ sample has an isotherm comparable to those obtained in $(*BEA)^{15}_{MC}$. However, at high p/p_0 values, there is a slight increase in the amount adsorbed, it is more pronounced in $(*BEA)^{10}_{SC}$. These differences are reflected in an increase in the mesoporous volumes (0.12 and 0.29 cm^3g^{-1}). In $(*BEA)^{15}_{NC}$, the increase in the amount adsorbed in p/p_0 greater than 0.8 is important. A narrow-type hysteresis H4 appears during desorption. The isotherm $(*BEA)^{15}_{NC}$ decomposes at low pressure in an isotherm Ib and in a type IV at p/p_0 high. The presence of this hysteresis is due to the presence of intercrystalline mesopores created by the agglomeration of nanocrystals. The isotherm for $(*BEA)^{17}_{NSp}$ after filling the micropores with N_2 (type Ib), the additional accumulation of the amount adsorbed appears from p/p_0 greater than 0.5 (type IV). The hysteresis that forms during desorption is H2 type. This type of hysteresis is generally observed in structured mesoporous materials.

For the MFI zeolites, Type I isotherms characteristics of microporous materials were observed for big crystal ($(MFI)^{40}_{MC}$) and for nanosheet MFI $(MFI)^{45}_{NSh}$. The isotherm $(MFI)^{20}_{NSp}$ decomposes similarly to the nano-sponge of *BEA.

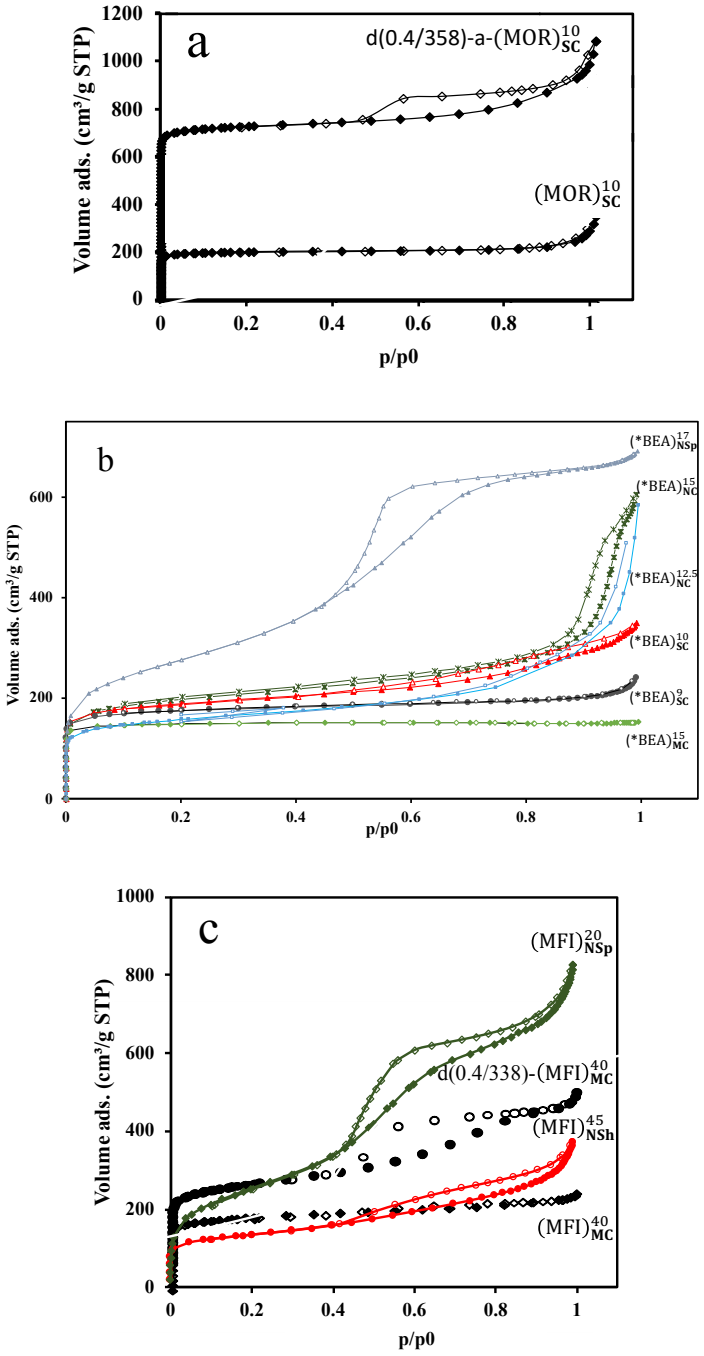


Figure III. 20 Isotherms of adsorption and nitrogen desorption for the zeolites synthesized and/or modified: a. MOR; b. *BEA and c. MFI zeolites.

Table III.6. reports the textural properties of the commercial and synthesized acidic catalysts.

Table III. 6 Textural properties of Amberlyst® 15, alumina, silica, alumina-silica and zeolites (commercial, modified and synthetized): MOR, FAU, *BEA and MFI.

Catalyst	S_{BET}[a] $m^2\ g^{-1}$	V_{micro}[b] $cm^3\ g^{-1}$	V_{meso}[c] $cm^3\ g^{-1}$
A-15	57	/	/
SiO_2			
Al_2O_3			
SiO_2-Al_2O_3		0.03	1.00
$(MOR)^{10}_{SC}$	524	0.20	0.06
d(0.4/358)-a-$(MOR)^{10}_{SC}$	558	0.21	0.26
$(FAU)^{2.6}_{SC}$	624	0.34	0.07
$(FAU)^{17}_{SC}$	840	0.32	0.15
$(FAU)^{40}_{SC}$	795	0.29	0.20
$(*BEA)^{15}_{MC}$	588	0.22	0.02
$(*BEA)^{9}_{SC}$	680	0.25	0.12
$(*BEA)^{10}_{SC}$	709	0.25	0.29
$(*BEA)^{12.5}_{NC}$	577	0.22	0.58
$(*BEA)^{15}_{NC}$	726	0.24	0.71
$(*BEA)^{17}_{NSp}$	977	0.30	0.74
$(MFI)^{40}_{MC}$	480	0.17	0.07
d(0.4/338)-$(MFI)^{40}_{MC}$	507	0.17	0.30
$(MFI)^{45}_{NC}$		0.18	0.36
$(MFI)^{45}_{NSh}$	492	0.18	0.36
$(MFI)^{20}_{NSp}$	888	0.30	0.98

a. Specific surface area measured by BET; b. micropore volume using *t*-plot method; c. mesopore volume =V_{total}-V_{micro} (V_{total}: determined from the adsorbed volume at p/p_0=0.96), total microporous volume estimated by DR method.

The silica, alumina and silica-alumina contrariwise to zeolite have practically no microporosity. The micropore volume value of the zeolites (V_{micro}) is a "fingerprint" of their framework. Regardless of the crystal size (Fig. II.21a), MOR, FAU, *BEA and MFI-type zeolites have a V_{micro} of 0.20, 0.30; 0.23 and 0.18 $cm^3\ g^{-1}$, respectively which are the values expected for conventional well crystallized zeolites from the same structural type. [37, 101, 103] The micropore volume of the nanosponge zeolites ($(BEA)^{17}_{NSp}$ and $(MFI)^{20}_{NSp}$) are higher owing to the presence of ultramicropores. The mesopores can be either intracrystalline or intergranular. [104, 105] The intergranular volume (V_{meso}) depends on both size and shape of the zeolite crystals; smaller the crystal size, greater the mesopore volume (Fig. II.21b). Therefore,

V_{meso} is near to zero on conventional micrometer zeolite samples. The alkaline treatment with NaOH on MOR and MFI zeolites allows generating intracrystalline mesopores while preserving their micropore volumes.

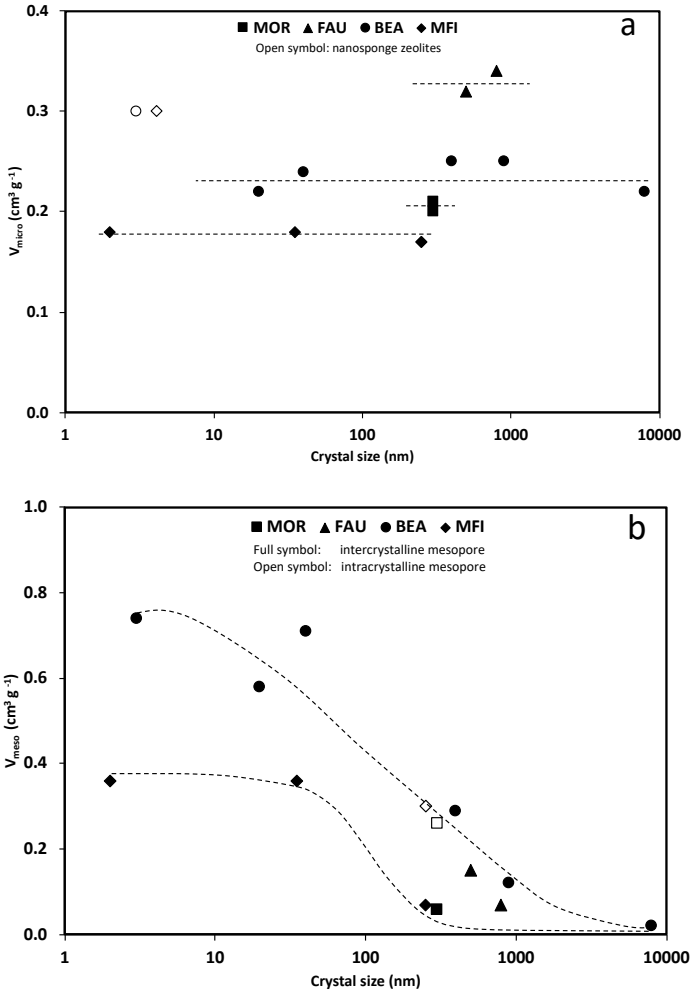


Figure III. 21 Micropore (a) and mesopore (b) volumes as a function of zeolite crystal size.

6.1.5. Acidity of the catalysts

Table III.7, shows the acidity values of the catalysts.

Table III. 7 Acidic properties of Amberlyst® 15, alumina, silica, alumina-silica and zeolites (commercial, modified and synthetized): MOR, FAU, *BEA and MFI.

Catalyst	$[P_yH^+]^a$ µmol g^{-1}	$[PyL]^b$ µmol g^{-1}
A-15	2370	/
SiO_2	0	0
Al_2O_3	0	321
SiO_2-Al_2O_3	43	96
$(MOR)^{10}_{SC}$	1056	31
d(0.4/358)-a-$(MOR)^{10}_{SC}$	533	101
$(FAU)^{2.6}_{SC}$	403	149
$(FAU)^{17}_{SC}$	197	44
$(FAU)^{40}_{SC}$	100	20
$(*BEA)^{15}_{MC}$	752	215
$(*BEA)^{9}_{SC}$	470	490
$(*BEA)^{10}_{SC}$	798	186
$(*BEA)^{12.5}_{NC}$	487	352
$(*BEA)^{15}_{NC}$	354	336
$(*BEA)^{17}_{NSp}$	130	176
$(MFI)^{40}_{MC}$	304	44
d(0.4/338)-$(MFI)^{40}_{MC}$	224	55
$(MFI)^{45}_{NC}$	332	25
$(MFI)^{45}_{NSh}$	83	119
$(MFI)^{20}_{NSp}$	151	44

a, b. Concentrations of Brønsted ($[PyH^+]$) and Lewis ([PyL]) sites able to retain pyridine at 423 K

A portion of the sulfonic acid groups on the Amberlyst® 15 (A-15) are strong enough to protonate and retain pyridine at 423 K. The concentration of the Brønsted acid sites (BAS) amounts to 2300 µmol g^{-1}, which corresponds to half of exchange capacity (between Na^+ and H^+) provided by the Rohm & Hass (4.7 mmol g^{-1}). This result corresponds well to earlier reports,[114] where acid site density on the dry macroreticular resin was measured from calorimetry of NH_3 at 353 K. The dry alumina catalyst has only Lewis acid sites (321 µmol g^{-1}) while the SiO_2 based material features no acidity able to retain pyridine at 423 K. On the other hand, the silica-alumina material features some BAS (43 µmol g^{-1}). For the zeolites, the BAS concentration depends on both the Si/Al molar ratio and on their accessibility. For

instance, in the case of FAU type zeolites BAS located within the sodalite cages are not accessible by pyridine and do not amount to the bulk probed acidity. Hence, the ratio between the probed acid sites to the theoretical, calculated from the elemental composition of the zeolite ($[PyH^+]_{423K}/[H^+]_{Theoretical}$) depends strongly on the zeolite framework (Figure III.22).

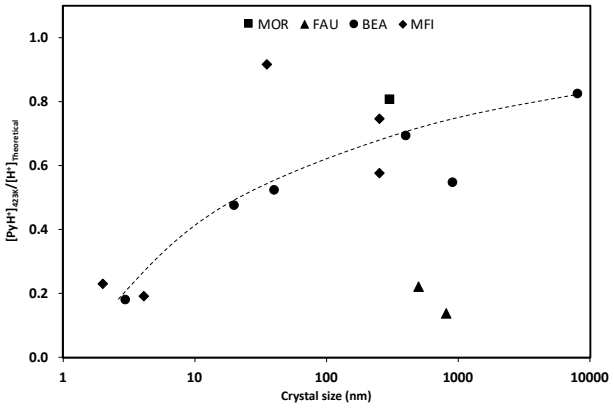


Figure III. 22 Proportion of theoretical Brønsted acid site probed by pyridine at 423 K as a function of zeolite crystal size.

This ratio is low for FAU type zeolite and 0.8 for MOR, due to acid sites located on the sodalite cages and side pockets, which are inaccessible to the basic probe. On *BEA and MFI zeolites, the portion of acid sites that are able to retain pyridine further depends on the average crystal size and $[PyH^+]_{423K}/[H^+]_{Theoretical}$ decreases drastically with the crystal size. Yet, Ryoo *et al.* observed slight or no change in BAS concentration with crystal downsizing.[115, 116] They evidenced that a nanospongenous *BEA zeolite (20 nm) contained 7 times more BAS at the external surface compare to a micron-sized *BEA (2 μm)[115], and almost 9 times more on MFI-based nano-sheets (2 nm) than on large MFI crystals (> 300 nm). [116] The same research group moreover concluded from various catalytic tests, such as Friedel-Crafts alkylation of benzene, *n*-octane cracking, Claisen-Schmidt condensation and methanol to DME conversion, that the external BAS are weaker than those within the sheets (*i.e.* internal BAS). This suggests that, the local geometry of protonic sites has a major impact on their

activity since the intrinsic strength of protonic sites, as demonstrated by Bokhoven *et al.*,[117] is identical regardless of the zeolite framework.

The amount of EFAl sites per unit cell can be concluded through comparing the bulk and the framework Si/Al molar ratios. The quantity of EFAl sites is very high on aluminum rich zeolite, such as FAU, which can easily be removed by thermal treatment (essentially for FAU with a low Si/Al ratio).[118] The presence of EFAl species can generate Lewis acid sites (LAS). *BEA zeolite features an important portion of LAS (176 – 490 μmol g^{-1}) amounting to the total acidity**.** The total concentration of Lewis acid sites increases with the number of EFAl species. Yet, this correlation is not perfectly linear (Figure III.23) as not all of the EFAl species comprise LAS and can be of cationic or neutral nature, such as $Al(OH)_2^+$, $Al(OH)^{2+}$, AlO^+, Al^{3+}, AlO(OH), pseudobohemite and Al_2O_3. [119-122] Moreover, EFAl species can be located within or at the outer surface of the zeolite microporosity.

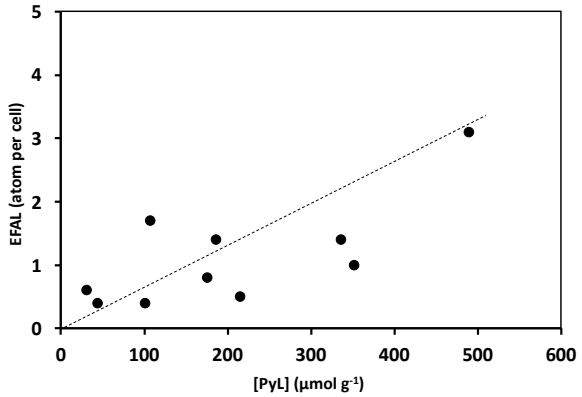


Figure III. 23 Correlation between EFAl and the Lewis acidity.

6.2. Glycerol etherification with *tert*-butyl alcohol

6.2.1. Thermodynamic analysis of reaction equilibrium

The glycerol etherification with *tert*-butyl alcohol was carried out in batch reactors at 363 K under autogenous pressure the reactions involved in the direct etherification of glycerol (G)

and *tert*-butyl alcohol (TBA) in mono-, di- and tri- ethers (MTBG, DTBG and TTBG, respectively) are summarized as follows:

$$G_{(l)} + TBA_{(l)} \underset{k_{-1}}{\overset{k_1}{\rightleftharpoons}} MTBG_{(l)} + H_2O_{(l)} \text{ with } \Delta G_1°_{298K} = -7.47 \text{ kJ mol}^{-1} \quad \text{(eq. 6)}$$

$$MTBG_{(l)} + TBA_{(l)} \underset{k_{-2}}{\overset{k_2}{\rightleftharpoons}} DTBG_{(l)} + H_2O_{(l)} \text{ with } \Delta G_2°_{298K} = -1.12 \text{ kJ mol}^{-1} \quad \text{(eq. 7)}$$

$$DTBG_{(l)} + TBA_{(l)} \underset{k_{-3}}{\overset{k_3}{\rightleftharpoons}} TTBG_{(l)} + H_2O_{(l)} \text{ with } \Delta G_3°_{298K} = 7.40 \text{ kJ mol}^{-1} \quad \text{(eq. 8)}$$

$$TBA_{(l)} \underset{k_{-4}}{\overset{k_4}{\rightleftharpoons}} IB_{(g)} + H_2O_{(l)} \quad \text{with } \Delta G_4°_{298K} = -1.52 \text{ kJ mol}^{-1} \quad \text{(eq. 9)}$$

It is worth to mention that the reverse reaction of TBA dehydration is negligible, since only a small amount of isobutene (IB) is dissolved in the liquid solution due to the low autogenous pressure (<0.5 MPa). The standard Gibbs free energy of formation used for MTBG, DTBG and TTBG are those obtained by Kiatkittipong[123] by using the Gani's method.[124] Table III.8, shows the thermodynamic data.

Table III. 8 Thermodynamic data.

Name	G° kJ. mol^{-1}	Origin
MTBG	-394.97	Gani method
DTBG	-336.49	Gani method
TTBG	-269.49	Gani method
TBA	-177.6	database
G	-447.1	database
$H_2O_{(l)}$	-237.2	database
$IB_{(g)}$	58.08	database

The authors predicted a minimization of the Gibbs free energy for an equilibrium conversion of glycerol (X_{eq}) at 363 K (with a supposed equimolar reactant mixture) of 75%.

Pico *et al*. found from two simplified kinetic models at 363 K with a TBA:G ratio of 1:4 (*i.e*. similar experimental condition to ours) a slightly higher value of X_{eq}, *i.e.* 80%.[125] Hence, the etherification of glycerol and *tert*-butyl alcohol in mono-, di- and tri-ethers is a reaction limited by a thermodynamic equilibrium, under the experimental conditions of this thesis, the maximum glycerol conversion expected is of 80%.

6.2.2. Kinetic model

The external mass transfer effect over $(*BEA)_{NC}^{12.5}$ shows that the conversion and selectivity into MTBG and DTBG increases with increasing stirring speed and levels off at speeds higher than 800 rpm (Figure III.24), indicating the absence of external diffusion limitations at such stirring speeds. This results compare well to those obtained by Gonzáles *et al.*, [95] and Karinen *et al.*, [126] who observed a dependence of the product selectivity as function of the stirring rate and that at higher speeds, the reaction was more selective towards the ethers, while below 1000 rpm oligomerization of isobutylene was observed. Therefore, the stirring speed has been set to 1200 rpm for all experiments.

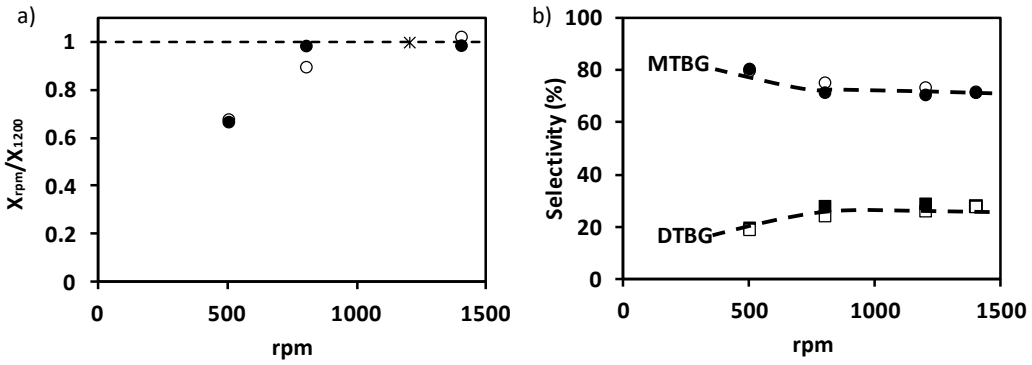


Figure III. 24 (a) Conversion normalized by the conversion achieved at 1200 rpm and (b) Selectivity of MTBG and DTBG as function of the stirring rate on $(*\mathbf{BEA})_{\mathbf{NC}}^{\mathbf{12.5}}$.

The order of reaction for glycerol and *tert*-butyl alcohol were established on the $(*BEA)_{NC}^{12.5}$ catalyst at 363 K and estimated from the variation of the initial rate with the concentration of that reactant, using the natural logarithm of the rate equation: $\ln r_0 = \ln k + \alpha ln[Gly]_0 +$

$\beta ln[TBA]_0$. The initial rate are measured in a series of experiments at different initial concentration of Gly ranged from 2.0 x10^{-4} to 1.0 x10^{-3} mol cm^{-3} with a molar ratio TBA/Gly from 10 to 40. In these conditions, the concentration of the exceeding reactant can be considered as almost invariant. The slope of the straight line in Figure III.25 of lnr_0 plot as a function of ln[Gly]$_0$ then corresponds to the partial order with respect to Gly. Similar experiments were carried out by maintaining the concentration of Gly constant and varying that of TBA concentration from 4.0 x10^{-4} to 2.0 x10^{-3} mol cm^{-3}.

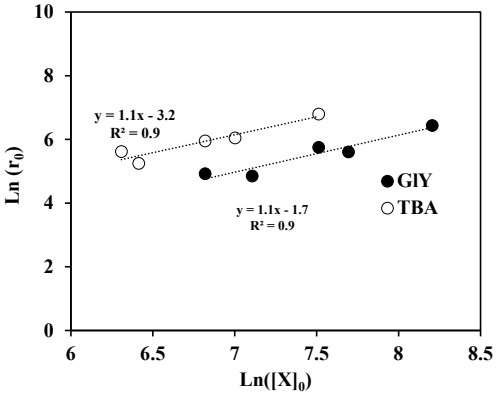


Figure III. 25 Natural logarithm of initial rates (lnr_0) as a function of natural logarithm of the initial concentration (ln[X]$_0$) of glycerol (full symbols) and TBA (open symbols). Kinetic study carried out on $(^*\mathbf{BEA})_{\mathbf{NC}}^{\mathbf{12.5}}$ at 363 K (data is given as absolute values).

The partial kinetic orders with respect to Gly and TBA are both close to 1. It is worth mentioning that for the etherification on the solid-acid resin Amberlyst® 15, the kinetic orders found by Frusteri *et al.*[127] are different and amount to an order of 0.3 with respect to Gly and an order of 1.7 with respect to *tert*-butyl alcohol. A possible explanation to this discrepancy might be due to the ability of the macroporous resin to enable the kinetically relevant steps between proximal adsorbates. Yet, Kiatkittipong *et al.*[123] found that on Amberlyst® 15 the Langmuir-Hinshelwood (LH) activity based model is the best suited kinetic model to fit the experimental results.

Nevertheless, a LH mechanism involving elementary steps between adsorbates on identical sites is highly unlikely especially on high Si/Al zeolites due to the distance between two adsorbates species (several nanometers). The coupling between such spatially dispersed adsorbates to form C-O bonds in etherification is highly unlikely. Bimolecular reactions on zeolites typically occur through Eley-Rideal (ER) type mechanisms, such as for alcohol dehydration,[128] alkane alkylation,[129] olefin oligomerization[130] and aromatics alkylation.[131] The partial kinetic orders with respect to glycerol and *tert*-butyl alcohol concentration equal to 1 are consistent with an ER mechanism, where TBA reacts with the adsorbed Gly.

6.2.3. Activity and stability

In Figure III.26, the glycerol conversion has been compared as a function of the reaction time for following catalysts: Amberlyst® 15 (A-15 as reference catalyst [93, 132, 133]), γ-Al_2O_3, SiO_2, SiO_2-Al_2O_3 and commercial zeolites ($(MOR)^{10}_{NC}$, $(FAU)^{40}_{SC}$, $(*BEA)^{12.5}_{NC}$, and $(MFI)^{45}_{NC}$).

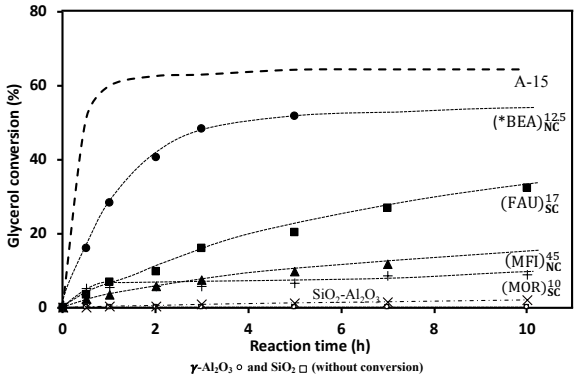


Figure III. 26 Glycerol conversion as a function of reaction time. Test carried out at 363 K, 1200 rpm, autogenous pressure, 7,5 % of catalyst (referred to glycerol mass) and glycerol/*tert*-butyl alcohol molar ratio of 0.25.

By employing A-15 as the catalyst, the conversion increases rapidly and reaches a plateau at 64% within 1 h. The plateau is 16% lower than the predicted equilibrium value, which means that conversion is hampered by deactivation of the sulfonic resin, probably due to a product inhibition effect, *e.g.* by H_2O. The catalysts based on SiO_2 and γ-Al_2O_3 show no

catalytic activity for the etherification (Table III.9, shows the conversion, selectivity and activity of catalysts). Hence, glycerol etherification at 363 K requires protonic sites. It is to note that the Lewis acid sites can catalyze the etherification reaction, yet merely at higher reaction temperatures (T>473 K [134-136]). At low temperatures the alcohol remains strongly adsorbed on the Lewis sites, [137] thus yielding an incomplete carbon balance (< 90%). On silica-alumina catalyst, the glycerol conversion is extremely slow and amounts to only 2% after 10 h of reaction, ascribable to the low BAS concentration (43 μmol g^{-1}). Employing $(*BEA)_{\mathbf{NC}}^{12.5}$ allows to achieve an increasing conversion up to a pseudo-plateau lower than that of A-15 at approximately 54%.

Indeed, the rate decreases with time due to reactant consumption and accumulation of products (MTBG) and more particularly water in the media. As there is no asymptotic approach towards the value of glycerol conversion equilibrium, this suggests that the catalysts deactivate (not by coking since the reaction temperature is too low, *i.e.* 353 K), but through a product inhibiting effect. [138] Using $(MOR)_{\mathbf{NC}}^{\mathbf{10}}$ a much stronger deactivation is observed, achieving a plateau at only 6% after 1 h. Indeed, such mono-dimensional zeolites are extremely sensitive to deactivation. [139] Employing $(FAU)_{\mathbf{SC}}^{\mathbf{40}}$ and $(MFI)_{\mathbf{NC}}^{\mathbf{45}}$ as catalysts, the glycerol conversion increases continuously with the reaction time, yet after 10 h the conversions are considerably lower than on $(*BEA)_{\mathbf{NC}}^{12.5}$, and are 33% and 20% against 54%, respectively (Figure III.26). It is interesting to note that the catalytic behavior of both of the large pores zeolites, FAU and *BEA, is significantly different. The higher efficiency of *BEA could be due to either the small crystal size that favors the diffusion of reactant and products or as proposed by Veiga *et al.,* [140] to the hydrophobic/hydrophilic balance of its surface. As far as the latter is concerned, the authors correlated catalytic activity and hydrophobicity index (drawn from the non-competitive adsorption of water and toluene) for FAU, MFI and *BEA zeolites. Yet, this relation is not consistent, as authors compared zeolites featuring different crystal size, as suggested by the indicated external surface (S_{ext}). Indeed, the high-value of S_{ext} of *BEA zeolite indicates small crystal size, whereas for FAU and MFI zeolites,

S_{ext} is low and corresponds hence to larger crystal sizes. Yet, the authors found *BEA to be the most active catalyst among all tested zeolites.

Table III. 9 Glycerol etherification with *tert*-butyl alcohol: conversion and selectivity after 10 h, initial activity (A_0) and TOF obtained on Amberlyst® 15, silica, alumina, silica-alumina and zeolites (commercial and synthetized): MOR, FAU, *BEA and MFI.

Catalyst	Conv. (%)	Selectivity (%)		$A_{0glycerol}$ (mol h^{-1} g^{-1}) x 10^4	TOF[a] (h^{-1}) x 10^2
		MTBG	h-GTBE		
A-15	64	75	25 (0.3)	15.00	63
SiO_2	0	0	0	0	0
Al_2O_3	0	0	0	0	0
SiO_2-Al_2O_3	2	100	0	0.22	51
$(MOR)_{NC}^{10}$	9	97	3	0.57	5
$(FAU)_{SC}^{2.6}$	5	100	0	1.33	33
$(FAU)_{SC}^{17}$	33	82	18 (0.6)	3.26	166
$(FAU)_{SC}^{40}$	23	83	17 (0.6)	1.36	136
$(*BEA)_{MC}^{15}$	12	93	7	0.08	1
$(*BEA)_{SC}^{9}$	61	74	26	9.90	198
$(*BEA)_{SC}^{10}$	57	81	19	5.60	70
$(*BEA)_{NC}^{12.5}$	54	70	30 (0.1)	7.00	151
$(*BEA)_{NC}^{15}$	57	71	29 (0.1)	4.80	161
$(*BEA)_{NSp}^{17}$	8	92	8	1.90	180
$(MFI)_{MC}^{40}$	8	99	< 1	0.31	10
$(MFI)_{NC}^{45}$	20	99	< 1	0.89	41
$(MFI)_{NSh}^{45}$	12	99	< 1	0.13	46
$(MFI)_{NSp}^{20}$	6	99	< 1	0.47	9

Reaction conditions: 7.5 wt.% of catalyst (referred to glycerol mass), glycerol/*tert*-butyl alcohol molar ratio = 0.25, reaction temperature = 363 K, reaction time = 10 h, stirring = 1200 rpm. MTBG: glycerol monoethers; h-GTBE: glycerol diethers + glicerol triether. In parenthesis, selectivity to glycerol triether (%). [a] Turnover frequency per Brønsted acid sites probed by the pyridine at 423 K,

Results of the catalytic etherification of glycerol with *tert*-butyl alcohol further compared in terms of initial activity (A_0), where possible deactivation does not occur. A_0 was estimated from the slope of the tangent at zero time fitted to the curves presented in Figure III.27. The initial activity of the sulfonic resin A-15 is the highest due to the important amount of BAS (Table III.7). On the tridimensional zeolites with large pores, *i.e.* FAU and *BEA zeolites, A_0

is proportional to the concentration of BAS, excepted for the catalyst featuring large crystals, *i.e.* $(*BEA)^{15}_{\mathbf{MC}}$ and $(FAU)^{2.6}_{\mathbf{SC}}$, that indicate the occurrence of diffusion limitation (DL), (Figure III.27).

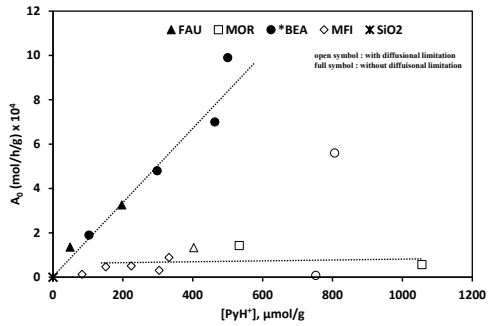


Figure III. 27 Initial activity of glycerol etherification with *tert*-butyl alcohol as a function of the concentration of protonic sites probed by pyridine at 423 K. (operating conditions: glycerol/*tert*-butyl alcohol molar ratio = 0.25, T = 363 K).

The effectiveness factor (η) relates the observed reaction rate with the intrinsic chemical rate ($r_{obs}/r_{intrinsic}$) and can be calculated from the ratio of two crystal sizes ($\frac{L_1}{L_2}$) and the ratio of corresponding initial activities ($\frac{r_{A1}}{rA_2}$) by using an iteratively resolved algebraic loop; [141] the method is described below:

The initial rate can be simplified in respect to a TBA/GLY ratio of 4 as follows:

$$r_{A,0} = 4k[GLY]_0^2 \qquad \text{(eq. 10)}$$

- The expression of Thiele modulus for reaction order of n [142]

$$\phi_s = \sqrt{\frac{n+1}{2}}\, L \sqrt{\frac{kC^{n-1}}{D_e}} \qquad \text{(eq. 11)}$$

with, L: crystal size (nm), *k*: intrinsic kinetic constant (mol/m^3 cat.s), and D_e: effective diffusion (m^2/s)

- Effectiveness factor:

$$\eta = \frac{\text{(actual mean reaction rate within pore)}}{\text{(rate if not slowed by pore diffusion)}} = \frac{r_A, \text{ with diffusion}}{r_A, \text{ without resistance}} \qquad \text{(eq. 12)}$$

where for the shape here considerate,

$$\eta = \frac{1}{\emptyset_s}\left(\frac{1}{\tanh 3\emptyset_s} - \frac{1}{3\emptyset_s}\right) \qquad \text{(eq. 13)}$$

- Combining (eq. 11) and (eq. 12):

$$\phi_s = \sqrt{\frac{3}{2}}\, L\sqrt{\frac{\eta\, k}{[GLY]_0^1\, D_e}} \qquad \text{(eq. 14)}$$

- Assumption: the same zeolite framework leads to identical *k* and D_e

If two crystal sizes L_1 and L_2 and two kinetic rates (k_{a1} and k_{a2}), are known, then,

$$\Rightarrow \quad \frac{\emptyset_{s1}}{\emptyset_{s2}} = \frac{L_1}{L_2} \qquad \text{(eq. 15)}$$

$$\Rightarrow \quad \frac{r_{A1}}{r_{A2}} = \frac{\eta_1}{\eta_2} \qquad \text{(eq. 16)}$$

The solution becomes possible with this algebraic loop resolved by iteration. [141] For that we begin by an arbitrary value of η_1 (e.g. 0.7), and solve the system by using the loop up to convergence. With this method, it is no need to have the value of $r_{intrinsic}$ to calculate the Thiele modulus and the efficiency factor.

Figure III.28, reports η as a function of the zeolite crystal size. The diffusion path being extremely short in *BEA nanosheets (*BEA)$^{17}_{\mathbf{NSp}}$, no diffusion limitations occur (η= 1). DL occur on the *BEA zeolite with crystal sizes above 100 nm. For the very acid MOR zeolite (1056 μmol g^{-1} [H^+]), activity is very low due to the diffusion controlled reaction induced by the long diffusion path (crystal size > 200 nm), and further accentuated by the mono-dimensional channel system. Although *BEA and MFI zeolites have identical acid strength[117] and similar confining voids (see section 3.2), the turnover rate is very low on the medium pore zeolite (9-46 h^{-1}) compared to that with large pores (150-198 h^{-1}). This suggests

that diffusion limitations occur even with a diffusion path length of a few nm. The DL is thus in this case most importantly governed by zeolite pore size and the void connectivity. Indeed for *BEA the void is connected by six 12 MR (0.67 nm), while for MFI by four 10 MR (0.54 nm). The kinetic diameter of glycerol is 0.61 nm[143] that explains the diffusion limitation encountered with the medium pore zeolite.

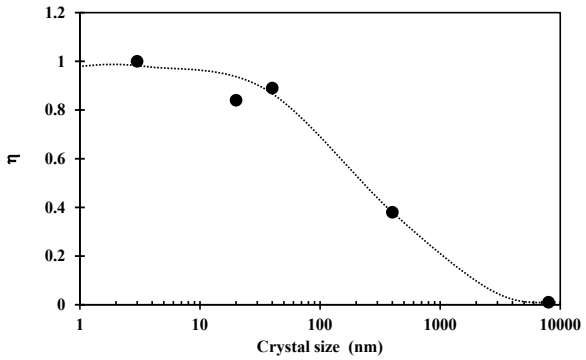


Figure III. 28 Effectiveness factor (***η***) in etherification of glycerol with *tert*-butyl alcohol as a function of the zeolite beta crystal size (operating conditions: glycerol/*tert*-butyl alcohol molar ratio = 0.25, T = 363 K).

6.2.4. Selectivity

The etherification of glycerol with *tert*-butyl alcohol (TBA) proceeds via a consecutive path that yields to the formation of water and five different alkyl glycerol ethers: MTBG (3-*tert*-butoxy-1,2 propanediol and 2-*tert*-butoxy-1,3 propanediol), DTBG (2,3-di-*tert*-butoxy-1-propanol and 1,3-di-*tert*-butoxy-2-propanol) and tri-*tert*-butoxy-propane (TTBG). Side reactions can occur such as the dehydration of TBA to isobutylene (IB) followed of its dimerization. No diisobutylene is detected (according to the chromatogram, Figure III.29) and the yield into isobutylene estimated from the autogenous pressure is negligible (less than 1%).

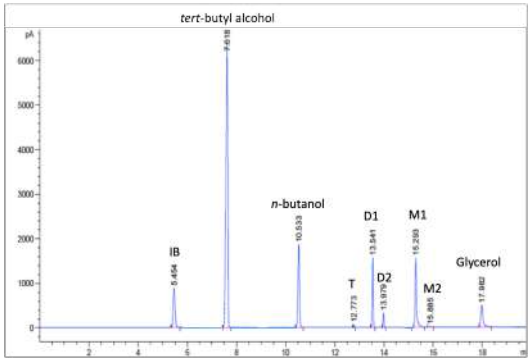


Figure III. 29 Typical chromatogram for the etherification of glycerol with *tert*-butyl alcohol; M1: 3-*tert*-butoxy-1,2 propanediol, M2: 2-*tert*-butoxy-1,3 propanediol, D1: 1,3-di-*tert*-butoxy-2-propanol, D2: 2,3-di-*tert*-butoxy-1-propanol, T: tri-*tert*-butoxy-propane, IB: isobutylene. *n*-butanol as internal standard.

Figure III.30, compares as function of conversion the molar yield of the MTBG (%) (primary product) and the DTBG (secondary product) on Amberlyst® 15 and commercial zeolites.

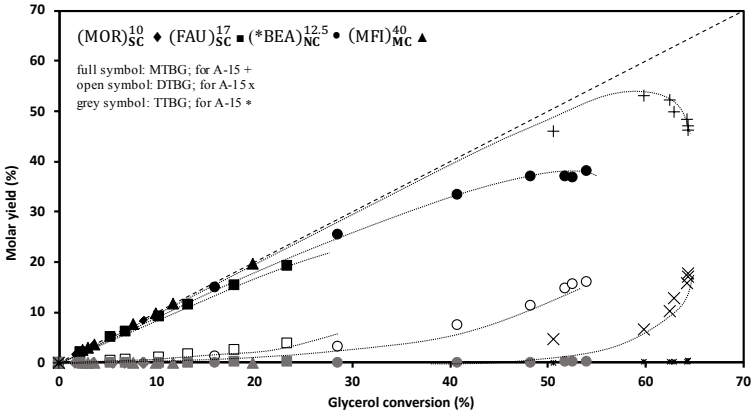


Figure III. 30 Molar yields into MTBG, DTBG and TTBG as a function of glycerol conversion.

Using A-15, the yield of the primary product reaches a maximum at *ca.* 50% glycerol conversion (Table III.9). The DTBG (secondary product) is starting to be formed at 30% glycerol conversion (extrapolated value at zero conversion). After 10 h of reaction, one quarter of the products are composed of DTBG, whereas the yield of TTBG (ternary product) is negligible (0.3%). Employing the large pores zeolites (*BEA, FAU and MOR) the di-

substituted ethers begin to be formed at a much lower glycerol conversion than for A-15, *i.e.* below 6% (Figure III.26). After 10 h of reaction, the selectivity into DTBG is 5% higher for $(BEA)_{NC}^{12.5}$ than for A-15. $(FAU)_{SC}^{17}$, is more selective for the formation of the di-substituted ether than the *BEA zeolite, the small difference provides from a higher yield into 1,2,3-tri-*tert*-butoxy propane. For $(MOR)_{NC}^{10}$ the selectivity into DTBG is low (1%), ascribable to the low glycerol conversion (6%). The medium pore zeolite $(MFI)_{NC}^{45}$ is almost totally selective to MTBG (99 %) even for a conversion of 20% (Table III.10).

Table III. 10 Selectivity of glycerol monoethers (MTBG), glycerol diethers (DTBG) and glycerol triether (TTBG) at isoconversion. (X ≈ 20 %) obtained on MOR, FAU, *BEA and MFI catalysts.

Catalyst	X (%)	MTBG (%)	DTBG (%)	TTBG (%)
$(FAU)_{SC}^{17}$	20	87	12.6	0.4
$(FAU)_{SC}^{40}$	23	83	16.4	0.6
$(*BEA)_{SC}^{9}$	22	97	3	0
$(*BEA)_{SC}^{10}$	23	98	2	0
$(*BEA)_{NC}^{12.5}$	22	89	11	0
$(MFI)_{NC}^{45}$	20	99	1	0

Glycerol etherification: 7.5 wt.% of catalyst to glycerol mass, glycerol/*tert*-butyl alcohol molar ratio = 0.25, T = 363 K.

In comparison with the sulfonic resin (A-15), which is a macroporous solid that hence features no spatial constraint, the use of large pore zeolites favors at low conversions successive etherification reactions ascribable to the overconcentration of ethers in the micropores resulting from steric hindrance. It can thus be assumed that zeolite catalysis induces "product shape selectivity".[93, 96] Yet, Gonzalez *et al.* claimed that the selectivity towards di- and tri-ethers is correlates with the strength of protonic sites. [94] Nevertheless, the correlation put forward is highly disputable and moreover merely valid for one zeolite (*BEA). Hence, the "product shape selectivity" mechanism through zeolite catalysis is a valuable mean that allows for explaining the observed selectivity.

6.2.5. Regeneration

The deactivated catalysts were regenerated either by (*i*) rinsing with ethanol at 373 K under 10 MPa nitrogen pressure by using a Dionex ASE 350 apparatus or (*ii*) through calcination in air at 823 K for 5 h. As expected, calcination allows to recover the entire activity of zeolite catalyst (Figure III.31).

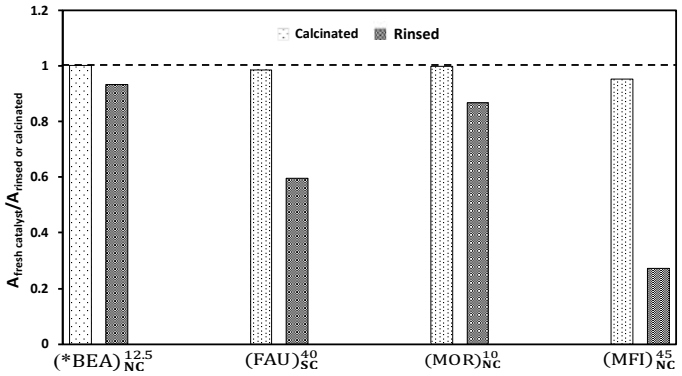


Figure III. 31 Recovered activity after washing with ethanol and calcination (823 K/6 h) of the deactivated catalysts.

Furthermore, as far as MOR and *BEA zeolites are concerned, rinsing with ethanol allows to recover greatly the catalytic activities, which are 87 and 93%, respectively. The extracted molecules by ethanol rinsing are glycerol and desired conversion products, MTBG and DTBG (only in the case of *BEA). This confirms what has been put forward by Gonzales *et al.*, who evidenced that the deactivation of *BEA zeolite during glycerol etherification resulted from zeolite micropores blocking with the reagent and products. [94] The retention of reactant and products within the micropores is thus due to steric hindrance.[144] These confined molecules are prone to limit or inhibit the bimolecular reaction. It can thus be assumed that the auto-inhibition is responsible for rapid decrease of the reaction rate (as observed in Figure III-26). The inhibition effect is strongly pronounced for mono-dimensional pore systems, *e.g.* $(MOR)^{10}_{NC}$, where a single molecule confined in the pore mouths already prevents the access to reagents to an important amount of acid sites located within the crystal, leading to a very fast deactivation.

Rinsing the deactivated $(FAU)_{SC}^{40}$ with ethanol permits to regenerate only partially catalytic activity (up to 60%), despite of recovering entirely the initial Brønsted acidity. Indeed, no interaction was observed between retained molecules (4.2 wt%) and zeolite –OH groups located in the supercages and in the sodalite cages (Figure III.32).

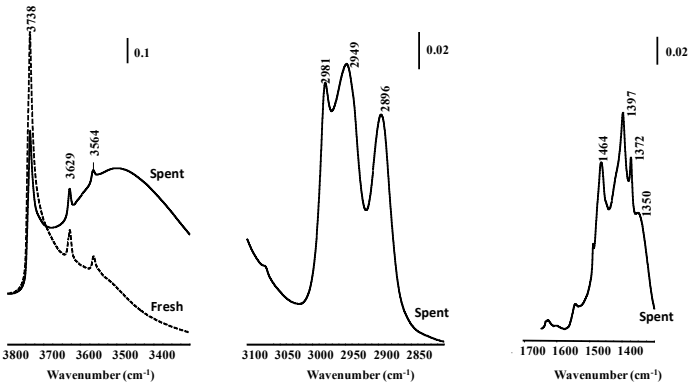


Figure III. 32 FT-IR spectra of: fresh and spent (after rinsing with ethanol) zeolite $(\mathbf{FAU})_{\mathbf{SC}}^{\mathbf{40}}$.

The loss of activity is thus merely due to a steric blockage of trapped molecules. The presence of the retained molecules within the surpercages decreases the available space that is enough to inhibit the bimolecular etherification reaction.

In the case of $(MFI)_{NC}^{45}$, the ethanol washing allows to recover 30% of catalytic activity, as almost 5.0wt% of molecules remain retained within the micropores upon rinsing. This observation can readily be attributed to the steric blocking of the pore intersections through retained molecules.

Washing with ethanol is more efficient on the zeolite featuring straight channels, such as *BEA and MOR zeolites, compared to zeolites possessing larger cavities than the pore size, *i.e.* the FAU supercage or presenting an intersected channel system, such as MFI, where the formation of large molecules is favored. The results obtained in this section thus clearly support the "product shape selectivity" mechanism suggested for the glycerol etherification over zeolites.

7. Conclusion

The results showed that, in a reaction sensitive to diffusion limitation (liquid phase, low temperature, bimolecular mechanism, large products molecules), such as the glycerol etherification with *tert*-butyl alcohol the zeolite confining void is not sufficient to predict activity, selectivity and stability; the accessibility to the void volume has to be taken into account. As an example, *BEA and MFI zeolites feature the same confining voids but the difference in their access (over 1 Å) is sufficient to generate strong diffusion limitations in the case of the medium pore zeolite. For *BEA (12 MR zeolite) the activity is proportional to the concentration of BAS at the condition that the crystal size is lower than 100 nm (absence of internal diffusion limitations). For zeolites featuring the biggest confining voids (*i.e.* the FAU supercage) successive etherification is favoured, yet product desorption is hampered.

For liquid phase reactions catalyzed by zeolite active sites the porous geometry (*i.e.* void volume, interconnection, size) has a crucial effect on confinement and shape selectivity and hence on catalytic key parameters (activity, selectivity and stability).

References

1. Broach, R. W.; Jan, D.-Y.; Lesch, D. A.; Kulprathipanja, S.; Roland, E.; Kleinschmit, P., Zeolites. In *Ullmann's Encyclopedia of Industrial Chemistry*, Chemistry, U. s. E. o. I., Ed. 2012.

2. Flanigen, E. M., Chapter 2 Zeolites and molecular sieves: An historical perspective. In *Introduction to Zeolite Science and Practice*, van Bekkum, H.; Flanigen, E. M.; Jacobs, P. A.; Jansen, J. C., Eds. Elsevier: 2001; Vol. 137, pp 11-35.

3. Guisnet, M.; Gilson, J.-P., *Zeolites for Cleaner Technologies*. Published by Imperial College Press and distributed by World Scientific Publishing CO.: London, 2002; Vol. 3.

4. Weigel, O.; Steinhoff, E., IX. Die Aufnahme organischer Flüssigkeitsdämpfe durch Chabasit. *Z. Kristallogr. Cryst. Mater.* **1924,** *61* (1-6), 125.

5. McBain, J. W., The Sorption of Gases and Vapours by Solids. *J. Phys. Chem.* **1932,** *37* (1), 149-150.

6. Barrer, R. M., 33. Synthesis of a zeolitic mineral with chabazite-like sorptive properties. *J. Chem. Soc.* **1948,** (0), 127-132.

7. Milton, R. M. Molecular-sieve adsorbents. 1959.

8. Wadlinger, R. L.; Kerr, G. T.; Rosinski, E. J. Catalytic composition of a crystalline zeolite. 1964.

9. Argauer, R. J.; Landolt, G. R. Crystalline zeolite zsm-5 and method of preparing the same. 1969.

10. Flanigen, E. M., Chapter 2 Zeolites and Molecular Sieves an Historical Perspective. In *Introduction to Zeolite Science and Practice*, van Bekkum, H.; Flanigen, E. M.; Jansen, J. C., Eds. Elsevier: 1991; Vol. 58, pp 13-34.

11. Maesen, T., The Zeolite Scene – An Overview. In *Introduction to Zeolite Science and Practice*, Čejka, J.; van Bekkum, H.; Corma, A.; Schüth, F., Eds. Elsevier: 2007; Vol. 168, pp 1-12.

12. Flanigen, E. M.; Patton, R. L. Silica polymorph and process for preparing same. 1976.

13. Wilson, S. T.; Lok, B. M.; Messina, C. A.; Cannan, T. R.; Flanigen, E. M., Aluminophosphate molecular sieves: a new class of microporous crystalline inorganic solids. *J. Am. Chem. Soc.* **1982,** *104* (4), 1146-1147.

14. Tanabe, K., Industrial application of solid acid–base catalysts. *Appl. Catal., A* **1999,** *181* (2), 399-434.

15. Sherman, J. D., Synthetic zeolites and other microporous oxide molecular sieves. *Proc Natl Acad Sci U S A* **1999,** *96* (7), 3471-8.

16. Rabo, J. A.; Schoonover, M. W., Early discoveries in zeolite chemistry and catalysis at Union Carbide, and follow-up in industrial catalysis. *Appl. Catal., A* **2001,** *222* (1-2), 261-275.

17. Rules for Framework Type Assignment. In *Atlas of Zeolite Framework Types*, Baerlocher, C.; McCusker, L. B.; Olson, D. H., Eds. Elsevier Science B.V.: Amsterdam, 2007; p 371.

18. Smith, J. V., Topochemistry of zeolites and related materials. 1. Topology and geometry. *Chem. Rev.* **1988,** *88* (1), 149-182.

19. Newsam, J. M., The zeolite cage structure. *Science* **1986,** *231* (4742), 1093-1099.

20. Chen, N. Y.; Degnan, T. F.; Smith, C. M., *Molecular Transport and Reaction in Zeolites: Design and Application of Shape Selective Catalysts*. VCH: 1994.

21. Davis, M. E.; Saldarriaga, C.; Montes, C.; Garces, J.; Crowdert, C., A molecular sieve with eighteen-membered rings. *Nature* **1988,** *331* (6158), 698-699.

22. Dessau, R. M.; Schlenker, J. L.; Higgins, J. B., Framework topology of AlPO4-8: the first 14-ring molecular sieve. *Zeolites* **1990,** *10* (6), 522-524.

23. Estermann, M.; McCusker, L. B.; Baerlocher, C.; Merrouche, A.; Kessler, H., A synthetic gallophosphate molecular sieve with a 20-tetrahedral-atom pore opening. *Nature* **1991,** *352* (6333), 320-323.

24. Derouane, E. G.; Védrine, J. C.; Pinto, R. R.; Borges, P. M.; Costa, L.; Lemos, M. A. N. D. A.; Lemos, F.; Ribeiro, F. R., The Acidity of Zeolites: Concepts, Measurements and Relation to Catalysis: A Review on Experimental and Theoretical Methods for the Study of Zeolite Acidity. *Chem. Rev.* **2013,** *55* (4), 454-515.

25. Walling, C., The Acid Strength of Surfaces. *J. Am. Chem. Soc.* **1950,** *72* (3), 1164-1168.

26. Rabo, J. A.; Gajda, G. J., Acid Function in Zeolites: Recent Progress. In *Guidelines for Mastering the Properties of Molecular Sieves*, Barthomeuf, D.; Derouane, E. G.; Hölderich, W., Eds. Springer US: Boston, MA, 1990; pp 273-297.

27. Bronsted, J. N., Acid and Basic Catalysis. *Chem. Rev.* **1928,** *5* (3), 231-338.

28. Lewis, G. N., The Atom and the Molecule. *J. Am. Chem. Soc.* **1916,** *38* (4), 762-785.

29. Busca, G., Acidity and basicity of zeolites: A fundamental approach. *Microporous Mesoporous Mater.* **2017,** *254*, 3-16.

30. Shannon, R. D.; Gardner, K. H.; Staley, R. H.; Bergeret, G.; Gallezot, P.; Auroux, A., The nature of the nonframework aluminum species formed during the dehydroxylation of H-Y. *J. Phys. Chem.* **1985,** *89* (22), 4778-4788.

31. Morin, S.; Berreghis, A.; Ayrault, P.; Gnep, N. S.; Guisnet, M., Dealumination of zeolites Part VIIIAcidity and catalytic properties of HEMT zeolites dealuminated by steaming. *J. Chem. Soc., Faraday Trans.* **1997,** *93* (17), 3269-3275.

32. Elanany, M.; Koyama, M.; Kubo, M.; Broclawik, E.; Miyamoto, A., Periodic density functional investigation of Lewis acid sites in zeolites: relative strength order as revealed from NH3 adsorption. *Appl. Surf. Sci.* **2005,** *246* (1-3), 96-101.

33. Chen, T.; Men, A.; Sun, P.; Zhou, J.; Yuan, Z.; Guo, Z.; Wang, J.; Ding, D.; Li, H., Lewis acid sites on dehydroxylated zeolite HZSM-5 studied by NMR and EPR. *Catal. Today* **1996,** *30* (1-3), 189-192.

34. Guisnet, M., Influence of zeolite composition on catalytic activity. In *Supported Catalysts and Their Applications*, Sherrington, D. C.; Kybett, A. P., Eds. The Royal Society of Chemistry: 2007; pp 55-67.

35. Parikh, P. A.; Subrahmanyam, N.; Bhat, Y. S.; Halgeri, A. B., Toluene ethylation over metallosilicates of MFI structure. Effects of acidity and crystal size on para-selectivity. *Catal. Lett.* **1992,** *14* (1), 107-113.

36. Hattori, T.; Yashima, T., *Zeolites and Microporous Crystals*. Elsevier Science: 1994.

37. Chaouati, N.; Soualah, A.; Hussein, I.; Comparot, J. D.; Pinard, L., Formation of weak and strong Brønsted acid sites during alkaline treatment on MOR zeolite. *Appl. Catal., A* **2016,** *526*, 95-104.

38. Smit, B.; Maesen, T. L., Towards a molecular understanding of shape selectivity. *Nature* **2008,** *451* (7179), 671-678.

39. Csicsery, S. M., Shape-selective catalysis in zeolites. *Zeolites* **1984,** *4* (3), 202-213.

40. Maxwell, I. E., Shape-selective catalysis and process technology via molecular inclusion in zeolites. *Journal of Inclusion Phenomena* **1986,** *4* (1), 1-29.

41. Derouane, E. G.; Dejaifve, P.; Gabelica, Z.; Védrine, J. C., Molecular shape selectivity of ZSM-5, modified ZSM-5 and ZSM-11 type zeolites. *Faraday Discuss. Chem. Soc.* **1981,** *72* (0), 331-344.

42. Weisz, P. B., Molecular shape selective catalysis. *Pure Appl. Chem.* **1980,** *52* (9), 2091-2103.

43. Teketel, S.; Westgård Erichsen, M.; Lønstad Bleken, F.; Svelle, S.; Petter Lillerud, K.; Olsbye, U., Chapter 6. Shape selectivity in zeolite catalysis. The Methanol to Hydrocarbons (MTH) reaction. In *Catalysis*, 2014; Vol. 26, pp 179-217.

44. Csicsery, S. M., Catalysis by shape selective zeolites-science and technology. *Pure Appl. Chem.* **1986,** *58* (6), 841–856.

45. Degnan, T. F., The implications of the fundamentals of shape selectivity for the development of catalysts for the petroleum and petrochemical industries. *J. Catal.* **2003,** *216* (1-2), 32-46.

46. Martens, J. A.; Vanbutsele, G.; Jacobs, P. A.; Denayer, J.; Ocakoglu, R.; Baron, G.; Muñoz Arroyo, J. A.; Thybaut, J.; Marin, G. B., Evidences for pore mouth and key–lock catalysis in hydroisomerization of long n-alkanes over 10-ring tubular pore bifunctional zeolites. *Catal. Today* **2001,** *65* (2-4), 111-116.

47. Roque-Malherbe, R.; Ivanov, V., Codiffusion and counterdiffusion of para-xylene and ortho-xylene in a zeolite with 10 MR/12 MR interconnected channels. An example of molecular traffic control. *J. Mol. Catal. A: Chem.* **2009,** *313* (1-2), 7-13.

48. Santilli, D. S.; Harris, T. V.; Zones, S. I., Inverse shape selectivity in molecular sieves: Observations, modelling, and predictions. *Microporous Mater.* **1993,** *1* (5), 329-341.

49. Dubbeldam, D.; Calero, S.; Maesen, T. L.; Smit, B., Understanding the window effect in zeolite catalysis. *Angew. Chem. Int. Ed. Engl.* **2003,** *42* (31), 3624-6.

50. Bibby, D. M.; Dale, M. P., Synthesis of silica-sodalite from non-aqueous systems. *Nature* **1985,** *317* (6033), 157-158.

51. Morris, R. E.; Weigel, S. J., The synthesis of molecular sieves from non-aqueous solvents. *Chem. Soc. Rev.* **1997,** *26* (4), 309-317.

52. Deforth, U.; Unger, K. K.; Schüth, F., Dry synthesis of B-MFI, MTN- and MTW-type materials. *Microporous Mater.* **1997,** *9* (5-6), 287-290.

53. Althoff, R.; Unger, K.; Schüth, F., Is the formation of a zeolite from a dry powder via a gas phase transport process possible? *Microporous Mater.* **1994,** *2* (6), 557-562.

54. Martínez Blanes, J. M.; Szyja, B. M.; Romero-Sarria, F.; Centeno, M. Á.; Hensen, E. J. M.; Odriozola, J. A.; Ivanova, S., Multiple Zeolite Structures from One Ionic Liquid Template. *Chem. Eur. J.* **2013,** *19* (6), 2122-2130.

55. Čejka, J.; Peréz-Pariente, J.; Roth, W. J., *Zeolites: From Model Materials to Industrial Catalysts*. Transworld Research Network: 2008.

56. Coker, E. N.; Jansen, J. C.; Martens, J. A.; Jacobs, P. A.; DiRenzo, F.; Fajula, F.; Sacco, A., The synthesis of zeolites under micro-gravity conditions: a review. *Microporous Mesoporous Mater.* **1998,** *23* (1-2), 119-136.

57. Cundy, C. S.; Cox, P. A., The hydrothermal synthesis of zeolites: Precursors, intermediates and reaction mechanism. *Microporous Mesoporous Mater.* **2005,** *82* (1-2), 1-78.

58. Breck, D. W., *Zeolite molecular sieves: structure, chemistry, and use*. Wiley: 1973.

59. Triantafyllidis, K. S.; Iliopoulou, E. F.; Karakoulia, S. A.; Nitsos, C. K.; Lappas, A. A., Mesoporous Zeolite Catalysts for Biomass Conversion to Fuels and Chemicals. In *Mesoporous Zeolites: Preparation, Characterization and Applications*, García-Martínez, J.; Li, K., Eds. 2015.

60. Van Aelst, J.; Verboekend, D.; Philippaerts, A.; Nuttens, N.; Kurttepeli, M.; Gobechiya, E.; Haouas, M.; Sree, S. P.; Denayer, J. F. M.; Martens, J. A.; Kirschhock, C. E. A.; Taulelle, F.; Bals, S.; Baron, G. V.; Jacobs, P. A.; Sels, B. F., Catalyst Design by NH4OH Treatment of USY Zeolite. *Adv. Funct. Mater.* **2015,** *25* (46), 7130-7144.

61. Poladi, R. H. P. R.; Landry, C. C., Oxidation of octane and cyclohexane using a new porous substrate, Ti-MMM-1. *Microporous Mesoporous Mater.* **2002,** *52* (1), 11-18.

62. Chal, R.; Gérardin, C.; Bulut, M.; van Donk, S., Overview and Industrial Assessment of Synthesis Strategies towards Zeolites with Mesopores. *ChemCatChem* **2011,** *3* (1), 67-81.

63. Xiao, F. S.; Han, Y.; Yu, Y.; Meng, X.; Yang, M.; Wu, S., Hydrothermally stable ordered mesoporous titanosilicates with highly active catalytic sites. *J. Am. Chem. Soc.* **2002,** *124* (6), 888-889.

64. Groen, J. C.; Jansen, J. C.; Moulijn, J. A.; Pérez-Ramírez, J., Optimal Aluminum-Assisted Mesoporosity Development in MFI Zeolites by Desilication. *J. Phys. Chem. B.* **2004,** *108* (35), 13062-13065.

65. Sachse, A.; Grau-Atienza, A.; Jardim, E. O.; Linares, N.; Thommes, M.; García-Martínez, J., Development of Intracrystalline Mesoporosity in Zeolites through Surfactant-Templating. *Cryst. Growth Des.* **2017,** *17* (8), 4289-4305.

66. Egeblad, K.; Christensen, C. H.; Kustova, M.; Christensen, C. H., Templating Mesoporous Zeolites†. *Chem. Mater.* **2008,** *20* (3), 946-960.

67. Viswanadham, N.; Kumar, M., Effect of dealumination severity on the pore size distribution of mordenite. *Microporous Mesoporous Mater.* **2006,** *92* (1-3), 31-37.

68. Nesterenko, N. S.; Thibault-Starzyk, F.; Montouillout, V.; Yuschenko, V. V.; Fernandez, C.; Gilson, J. P.; Fajula, F.; Ivanova, I. I., Accessibility of the acid sites in dealuminated small-port mordenites studied by FTIR of co-adsorbed alkylpyridines and CO. *Microporous Mesoporous Mater.* **2004,** *71* (1-3), 157-166.

69. Weitkamp, J.; Sakuth, M.; Chen, C.-Y.; Ernst, S., Dealumination of zeolite beta using (NH4)2SiF6 and SiCl4. *J. Chem. Soc., Chem. Commun.* **1989,** (24), 1908-1910.

70. Sánchez, N. A.; Saniger, J. M.; d'Espinose de la Caillerie, J.-B.; Blumenfeld, A. L.; Fripiat, J. J., Dealumination and surface fluorination of H-ZSM-5 by molecular fluorine. *Microporous Mesoporous Mater.* **2001,** *50* (1), 41-52.

71. Müller, M.; Harvey, G.; Prins, R., Comparison of the dealumination of zeolites beta, mordenite, ZSM-5 and ferrierite by thermal treatment, leaching with oxalic acid and treatment with SiCl4 by 1H, 29Si and 27Al MAS NMR. *Microporous Mesoporous Mater.* **2000,** *34* (2), 135-147.

72. Groen, J. C.; Moulijn, J. A.; Pérez-Ramírez, J., Alkaline Posttreatment of MFI Zeolites. From Accelerated Screening to Scale-up. *Ind. Eng. Chem. Res.* **2007,** *46* (12), 4193-4201.

73. Dessau, R. M.; Valyocsik, E. W.; Goeke, N. H., Aluminum zoning in ZSM-5 as revealed by selective silica removal. *Zeolites* **1992,** *12* (7), 776-779.

74. Ogura, M.; Shinomiya, S.-y.; Tateno, J.; Nara, Y.; Kikuchi, E.; Matsukata, M., Formation of Uniform Mesopores in ZSM-5 Zeolite through Treatment in Alkaline Solution. *Chem. Lett.* **2000,** *29* (8), 882-883.

75. Su, L.; Liu, L.; Zhuang, J.; Wang, H.; Li, Y.; Shen, W.; Xu, Y.; Bao, X., Creating Mesopores in ZSM-5 Zeolite by Alkali Treatment: A New Way to Enhance the Catalytic Performance of Methane Dehydroaromatization on Mo/HZSM-5 Catalysts. *Catal. Lett.* **2003,** *91* (3/4), 155-167.

76. Benghalem, M. A.; Pinard, L.; Comparot, J.-D.; Astafan, A.; Daou, T. J.; Belin, T., Impact of Crystal Size on the Acidity and the Involved Interactions Studied by Conventional and Innovative Techniques. *J. Phys. Chem. C.* **2017,** *121* (34), 18725-18737.

77. Valtchev, V.; Tosheva, L., Porous nanosized particles: preparation, properties, and applications. *Chem. Rev.* **2013,** *113* (8), 6734-6760.

78. Zaarour, M.; Dong, B.; Naydenova, I.; Retoux, R.; Mintova, S., Progress in zeolite synthesis promotes advanced applications. *Microporous Mesoporous Mater.* **2014,** *189*, 11-21.

79. Mintova, S.; Olson, N. H.; Valtchev, V.; Bein, T., Mechanism of Zeolite A Nanocrystal Growth from Colloids at Room Temperature. *Science* **1999,** *283* (5404), 958-960.

80. Huang, L.; Wang, Z.; Sun, J.; Miao, L.; Li, Q.; Yan, Y.; Zhao, D., Fabrication of Ordered Porous Structures by Self-Assembly of Zeolite Nanocrystals. *J. Am. Chem. Soc.* **2000,** *122* (14), 3530-3531.

81. Larsen, S. C., Nanocrystalline Zeolites and Zeolite Structures: Synthesis, Characterization, and Applications. *J. Phys. Chem. C.* **2007,** *111* (50), 18464-18474.

82. Vuong, G. T.; Do, T. O., A new route for the synthesis of uniform nanozeolites with hydrophobic external surface in organic solvent medium. *J. Am. Chem. Soc.* **2007,** *129* (13), 3810-3811.

83. Camblor, M. A.; Corma, A.; Valencia, S., Characterization of nanocrystalline zeolite Beta. *Microporous Mesoporous Mater.* **1998,** *25* (1-3), 59-74.

84. Liu, Y.; Sun, M.; Lew, C. M.; Wang, J.; Yan, Y., MEL-type Pure-Silica Zeolite Nanocrystals Prepared by an Evaporation-Assisted Two-Stage Synthesis Method as Ultra-Low-k Materials. *Adv. Funct. Mater.* **2008,** *18* (12), 1732-1738.

85. Larlus, O.; Mintova, S.; Bein, T., Environmental syntheses of nanosized zeolites with high yield and monomodal particle size distribution. *Microporous Mesoporous Mater.* **2006,** *96* (1-3), 405-412.

86. Kim, Y. C.; Jeong, J. Y.; Hwang, J. Y.; Kim, S. D.; Kim, W. J., Influencing factors on rapid crystallization of high silica nano-sized zeolite Y without organic template under atmospheric pressure. *J. Porous Mater.* **2008,** *16* (3), 299-306.

87. Huang, Y.; Wang, K.; Dong, D.; Li, D.; Hill, M. R.; Hill, A. J.; Wang, H., Synthesis of hierarchical porous zeolite NaY particles with controllable particle sizes. *Microporous Mesoporous Mater.* **2010,** *127* (3), 167-175.

88. Ng, E. P.; Chateigner, D.; Bein, T.; Valtchev, V.; Mintova, S., Capturing ultrasmall EMT zeolite from template-free systems. *Science* **2012,** *335* (6064), 70-73.

89. Madsen, C.; Madsen, C.; Jacobsen, C. J. H., Nanosized zeolite crystals—convenient control of crystal size distribution by confined space synthesis. *Chem. Commun.* **1999,** (8), 673-674.

90. Tang, K.; Wang, Y. G.; Song, L. J.; Duan, L. H.; Zhang, X. T.; Sun, Z. L., Carbon nanotube templated growth of nano-crystalline ZSM-5 and NaY zeolites. *Mater. Lett.* **2006,** *60* (17-18), 2158-2160.

91. Wang, H.; Holmberg, B. A.; Yan, Y., Synthesis of template-free zeolite nanocrystals by using in situ thermoreversible polymer hydrogels. *J. Am. Chem. Soc.* **2003,** *125* (33), 9928-9.

92. Klepáþová K. , M. D., Etherification of Glycerol. *Pet. Coal* **2003,** *45* (1-2), 54-57.

93. Klepáčová, K.; Mravec, D.; Bajus, M., tert-Butylation of glycerol catalysed by ion-exchange resins. *Appl. Catal., A* **2005,** *294* (2), 141-147.

94. González, M. D.; Cesteros, Y.; Salagre, P., Establishing the role of Brønsted acidity and porosity for the catalytic etherification of glycerol with tert-butanol by modifying zeolites. *Appl. Catal., A* **2013,** *450*, 178-188.

95. González, M. D.; Salagre, P.; Linares, M.; García, R.; Serrano, D.; Cesteros, Y., Effect of hierarchical porosity and fluorination on the catalytic properties of zeolite beta for glycerol etherification. *Appl. Catal., A* **2014,** *473*, 75-82.

96. Simone, N.; Carvalho, W. A.; Mandelli, D.; Ryoo, R., Nanostructured MFI-type zeolites as catalysts in glycerol etherification with tert -butyl alcohol. *J. Mol. Catal. A: Chem.* **2016,** *422*, 115-121.

97. Manjunathan, P.; Kumar, M.; Churipard, S. R.; Sivasankaran, S.; Shanbhag, G. V.; Maradur, S. P., Catalytic etherification of glycerol to tert-butyl glycerol ethers using tert-butanol over sulfonic acid functionalized mesoporous polymer. *RSC Advances* **2016,** *6* (86), 82654-82660.

98. Weisz, P. B.; Frilette, V. J., Intracrystalline and Molecular-Shape-Selective Catalysis by Zeolite Salts. *J. Phys. Chem.* **1960,** *64* (3), 382-382.

99. Derouane, E. G., Zeolites as solid solvents1Paper presented at the International Symposium `Organic Chemistry and Catalysis' on the occasion of the 65th birthday of Prof. H. van Bekkum, Delft, Netherlands, 2–3 October 1997.1. *J. Mol. Catal. A: Chem.* **1998,** *134* (1-3), 29-45.

100. Okada, K.; Tomita, T.; Kameshima, Y.; Yasumori, A.; MacKenzie, K. J., Surface Acidity and Hydrophilicity of Coprecipitated Al(2)O(3)-SiO(2) Xerogels Prepared from Aluminium Nitrate Nonahydrate and Tetraethylorthosilicate. *J. Colloid Interface Sci.* **1999,** *219* (1), 195-200.

101. Borade, R. B.; Clearfield, A., Preparation of aluminum-rich Beta zeolite. *Microporous Mater.* **1996,** *5* (5), 289-297.

102. Lauridant, N.; Jean Daou, T.; Arnold, G.; Patarin, J.; Faye, D., MFI/∗BEA hybrid coating on aluminum alloys. *Microporous Mesoporous Mater.* **2013,** *166*, 79-85.

103. Na, K.; Jo, C.; Kim, J.; Cho, K.; Jung, J.; Seo, Y.; Messinger, R. J.; Chmelka, B. F.; Ryoo, R., Directing Zeolite Structures into Hierarchically Nanoporous Architectures. *Science* **2011,** *333* (6040), 328-332.

104. Astafan, A.; Benghalem, M. A.; Pouilloux, Y.; Patarin, J.; Bats, N.; Bouchy, C.; Daou, T. J.; Pinard, L., Particular properties of the coke formed on nano-sponge *BEA zeolite during ethanol-to-hydrocarbons transformation. *J. Catal.* **2016,** *336*, 1-10.

105. Kabalan, I.; Khay, I.; Nouali, H.; Ryzhikov, A.; Lebeau, B.; Albrecht, S.; Rigolet, S.; Fadlallah, M.-B.; Toufaily, J.; Hamieh, T.; Patarin, J.; Daou, T. J., Influence of the Particle Sizes on the Energetic Performances of MFI-Type Zeolites. *J. Phys. Chem. C.* **2015,** *119* (32), 18074-18083.

106. Choi, M.; Na, K.; Kim, J.; Sakamoto, Y.; Terasaki, O.; Ryoo, R., Stable single-unit-cell nanosheets of zeolite MFI as active and long-lived catalysts. *Nature* **2009,** *461* (7261), 246-249.

107. Astafan, A. Synthèses, caractérisations et performances catalytiques des zéolithes nanoéponge de type structurale *BEA. Université de Poitiers, France, 2016.

108. Coutanceau C., J. M. D., M F Alvarez, M. Guisnet, Dealumination of zeolites. Influence of the acid treatment of a HBEA zeolite on the framework composition and on the porosity. *J. Chim. Phys. Phys.- Chim. Biol.* **1997,** *94*, 765-781.

109. Makarova, M. A.; Karim, K.; Dwyer, J., Limitation in the application of pyridine for quantitative studies of brönsted acidity in relatively aluminous zeolites. *Microporous Mater.* **1995,** *4* (2-3), 243-246.

110. Emeis, C. A., Determination of Integrated Molar Extinction Coefficients for Infrared Absorption Bands of Pyridine Adsorbed on Solid Acid Catalysts. *J. Catal.* **1993,** *141* (2), 347-354.

111. Shi, G.; Zhang, H., The relationship between absorption coefficient and temperature and their effect on the atmospheric cooling rate. *J. Quant. Spectrosc. Radiat. Transfer* **2007,** *105* (3), 459-466.

112. Bauer, A.; Godon, M.; Carlier, J.; Ma, Q.; Tipping, R. H., Absorption by H2O and H2O-N2 mixtures at 153 GHz. *J. Quant. Spectrosc. Radiat. Transfer* **1993,** *50* (5), 463-475.

113. Paixão, V.; Monteiro, R.; Andrade, M.; Fernandes, A.; Rocha, J.; Carvalho, A. P.; Martins, A., Desilication of MOR zeolite: Conventional versus microwave assisted heating. *Appl. Catal., A* **2011,** *402* (1-2), 59-68.

114. Nguyen, V. C.; Bui, N. Q.; Mascunan, P.; Vu, T. T. H.; Fongarland, P.; Essayem, N., Esterification of aqueous lactic acid solutions with ethanol using carbon solid acid catalysts: Amberlyst 15, sulfonated pyrolyzed wood and graphene oxide. *Appl. Catal., A* **2018,** *552*, 184-191.

115. Kim, J.-C.; Cho, K.; Ryoo, R., High catalytic performance of surfactant-directed nanocrystalline zeolites for liquid-phase Friedel–Crafts alkylation of benzene due to external surfaces. *Appl. Catal., A* **2014,** *470*, 420-426.

116. Kim, K.; Ryoo, R.; Jang, H.-D.; Choi, M., Spatial distribution, strength, and dealumination behavior of acid sites in nanocrystalline MFI zeolites and their catalytic consequences. *J. Catal.* **2012,** *288*, 115-123.

117. Xu, B.; Sievers, C.; Hong, S.; Prins, R.; Vanbokhoven, J., Catalytic activity of Brønsted acid sites in zeolites: Intrinsic activity, rate-limiting step, and influence of the local structure of the acid sites. *J. Catal.* **2006,** *244* (2), 163-168.

118. Silaghi, M.-C.; Chizallet, C.; Raybaud, P., Challenges on molecular aspects of dealumination and desilication of zeolites. *Microporous Mesoporous Mater.* **2014,** *191*, 82-96.

119. Song, C.; Garcés, J. M.; Sugi, Y., *Shape-Selective Catalysis*. American Chemical Society: 1999; Vol. 738, p 428.

120. Whyte, T. E.; Dalla Betta, R. A.; Derouane, E. G.; Baker, R. T. K., *Catalytic Materials: Relationship Between Structure and Reactivity*. American Chemical Society: 1984; Vol. 248, p 484.

121. Gates, B. C., *Chemistry of catalytic processes*. American Institute of Chemical Engineers: New York, 1979; Vol. 25.

122. Ribeiro, F. R.; Guisnet, M., *Les zéolithes, un nanomonde au service de la catalyse: un nanomonde au service de la catalyse*. EDP Sciences: 2012.

123. Kiatkittipong, W.; Intaracharoen, P.; Laosiripojana, N.; Chaisuk, C.; Praserthdam, P.; Assabumrungrat, S., Glycerol ethers synthesis from glycerol etherification with tert-butyl alcohol in reactive distillation. *Comput. Chem. Eng.* **2011,** *35* (10), 2034-2043.

124. Constantinou, L.; Gani, R., New group contribution method for estimating properties of pure compounds. *AlChE J.* **1994,** *40* (10), 1697-1710.

125. Pico, M. P.; Romero, A.; Rodríguez, S.; Santos, A., Etherification of Glycerol by tert-Butyl Alcohol: Kinetic Model. *Ind. Eng. Chem. Res.* **2012,** *51* (28), 9500-9509.

126. Karinen, R. S.; Krause, A. O. I., New biocomponents from glycerol. *Appl. Catal., A* **2006,** *306*, 128-133.

127. Frusteri, F.; Arena, F.; Bonura, G.; Cannilla, C.; Spadaro, L.; Di Blasi, O., Catalytic etherification of glycerol by tert-butyl alcohol to produce oxygenated additives for diesel fuel. *Appl. Catal., A* **2009,** *367* (1-2), 77-83.

128. Blaszkowski, S. R.; van Santen, R. A., The Mechanism of Dimethyl Ether Formation from Methanol Catalyzed by Zeolitic Protons. *J. Am. Chem. Soc.* **1996,** *118* (21), 5152-5153.

129. Kirsch, F., Isoparaffin-olefin alkylations with crystalline aluminosilicates I. Early studies?C4-olefins. *J. Catal.* **1972,** *27* (1), 142-150.

130. Vandenberg, J., Low-temperature oligomerization of small olefins on zeolite H-ZSM-5. An investigation with high-resolution solid-state 13C-NMR. *J. Catal.* **1983,** *80* (1), 130-138.

131. Venuto, P. B.; Landis, P. S., Organic Catalysis over Crystalline Aluminosilicates. In *Advances in Catalysis*, Eley, D. D.; Pines, H.; Weisz, P. B., Eds. Academic Press: 1968; Vol. 18, pp 259-371.

132. Pico, M. P.; Rosas, J. M.; Rodríguez, S.; Santos, A.; Romero, A., Glycerol etherification over acid ion exchange resins: effect of catalyst concentration and reusability. *J. Chem. Technol. Biotechnol.* **2013,** *88* (11), 2027-2038.

133. Melero, J. A.; Vicente, G.; Morales, G.; Paniagua, M.; Bustamante, J., Oxygenated compounds derived from glycerol for biodiesel formulation: Influence on EN 14214 quality parameters. *Fuel* **2010,** *89* (8), 2011-2018.

134. Xu, M.; Lunsford, J. H.; Goodman, D. W.; Bhattacharyya, A., Synthesis of dimethyl ether (DME) from methanol over solid-acid catalysts. *Appl. Catal., A* **1997,** *149* (2), 289-301.

135. Yaripour, F.; Mollavali, M.; Jam, S. M.; Atashi, H., Catalytic Dehydration of Methanol to Dimethyl Ether Catalyzed by Aluminum Phosphate Catalysts. *Energy Fuels* **2009,** *23* (4), 1896-1900.

136. Aboul-Fotouh, S. M. K., Effect of ultrasonic irradiation and/or halogenation on the catalytic performance of γ-Al2O3 for methanol dehydration to dimethyl ether. *Journal of Fuel Chemistry and Technology* **2013,** *41* (9), 1077-1084.

137. Copeland, J. R.; Santillan, I. A.; Schimming, S. M.; Ewbank, J. L.; Sievers, C., Surface Interactions of Glycerol with Acidic and Basic Metal Oxides. *J. Phys. Chem. C.* **2013,** *117* (41), 21413-21425.

138. Guidotti, M.; Canaff, C.; Coustard, J.; Magnoux, P.; Guisnet, M., Acetylation of aromatic compounds over H-BEA zeolite: the influence of the substituents on the reactivity and on the catalyst stability. *J. Catal.* **2005,** *230* (2), 375-383.

139. Magnoux, P., Coking, aging, and regeneration of zeolites *1II. Deactivation of HY zeolite during n-heptane cracking. *J. Catal.* **1987,** *106* (1), 235-241.

140. Veiga, P. M.; Gomes, A. C. L.; Veloso, C. O.; Henriques, C. A., Acid zeolites for glycerol etherification with ethyl alcohol: Catalytic activity and catalyst properties. *Appl. Catal., A* **2017,** *548* (Supplement C), 2-15.

141. Levenspiel, O., *Chemical reaction engineering*. Wiley: 1999.

142. Ruud I. Wijngaarden, K. R. W., Alexander Kronberg, A. N. R. Bos, *Industrial Catalysis: Optimizing Catalysts and Processes*. Wiley: 2008.

143. Li, S., Separation of 1,3-propanediol from glycerol and glucose using a ZSM-5 zeolite membrane. *J. Membr. Sci.* **2001,** *191* (1-2), 53-59.

144. Guisnet, M.; Magnoux, P., Deactivation of Zeolites by Coking. Prevention of Deactivation and Regeneration. In *Zeolite Microporous Solids: Synthesis, Structure, and Reactivity*, Derouane, E. G., Lemos, F., Naccache, C., Ramôa Ribeiro, F. , Ed. Springer Netherlands: 1992; pp 457-474.

Chapter 4:

Sulfonated graphenes in the etherification of glycerol with *tert*-butyl alcohol

(Based on the publication: C. Miranda *et al.* / Journal of Applied Catalysis: A, General 580 (2019) 167-177)

1. The carbon

The carbon is the chemical element with the symbol C and the atomic number 6. It has three isotopes of natural origin (^{12}C and ^{13}C are stable, ^{14}C is radioactive). It can be linked to other small atoms, including other carbon atoms, thus giving a series of kinetically stable allotropes with varying dimensions. [1]

The electronic configuration of carbon is $1s^2\ 2s^2\ 2p^2$ (where the p orbital is divided into p_x, p_y and p_z). Due to the possibility of combining orbitals in this element, the carbon atoms can adopt three types of hybridization: sp^3, sp^2 and sp.

Carbon sp^3 hybridization

The sp^3 or tetragonal hybridization arises from the mixture of an orbital s with three p orbitals that originate four equivalent hybrid orbitals. These hybrid orbitals are oriented as far apart as possible by placing them at the vertices of a regular tetrahedron with bond angles of 109.5º. The four bonds formed are covalent sigma bonds (σ) that have the function of conferring structural stability to the molecule.

It is important to bear in mind that although a high energy is required to carry out the hybridization, it is compensated with the energy released by the formation of extraordinarily strong bonds. [2]

Carbon sp^2 hybridization

In sp^2 hybridization of carbon, three equivalent hybrid orbitals are generated from the mixture of one s orbital with two p orbitals. These three σ hybrid orbitals are oriented in a flat trigonal geometry and the angle of union between them is 120º.

In this case, the 2pz orbital remains unhybridized and is located perpendicular to the plane integrated by the hybridized orbitals σ and its electron is available for the formation of a pi (π) bond with other atoms.

Carbon sp hybridization

In sp or linear hybridization, two hybrid orbitals are generated by the combination of an orbital s with a p orbital. Both hybrid orbitals form an angle of 180° and, consequently, the molecular geometry is linear. In this process, the $2p_y$ and $2p_z$ orbitals do not participate in the hybridization and their electrons are weakly bound and available for the formation of π bonds.

Figure IV. 1 shows the carbon hybridization.

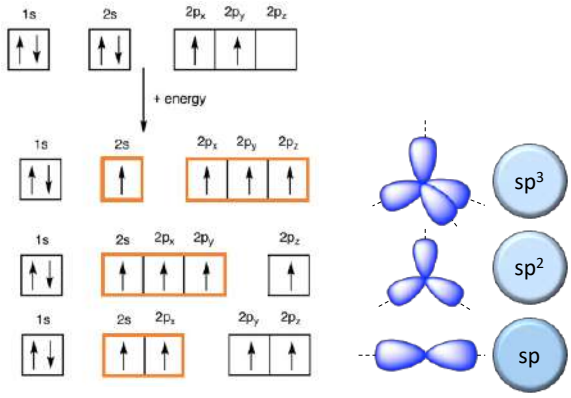


Figure IV. 1 Hybridization of carbon orbitals.

The multiple ways in which carbon atoms can be organized in space are linked to the type of hybridization that has been obtained from their orbitals and, therefore, this atom has a wide variety of allotropic forms with varied characteristics and properties.

1.1. Allotropic forms of carbon

For a long time, it was considered that carbon formed only two primary structures: diamond and graphite. The diamond is formed by carbon atoms with an sp^3 hybridization where each atom is joined to four others in a tetrahedral arrangement that forms a three-dimensional

network. This three-dimensional network of covalent bonds is what gives the diamond the properties of high hardness, excellent thermal conductivity, behavior electrical insulation, optical transparency and high melting points. On the other hand, the structure of the graphite is entirely different from that of the diamond. It presents an sp^2 hybridization which causes its orbitals to be distributed in a flat trigonal geometry, with angles of 120^o to each other. Each atom is covalently bound to three other carbon atoms in a hexagonal distribution mesh. These meshes are linked by weak Van der Waals links and, consequently, the graphite has a high anisotropy, so some of its properties vary considerably depending on the direction in which they are measured. In the plane, the graphite is a good electrical and thermal conductor, not in the normal direction to the surface due to the relatively high separation of layers. Mechanically, its planes can easily slide over each other, but in the perpendicular direction it has a high hardness. It is essential to highlight that graphite chemically is an inert material.

However, in the last three decades a new exotic series of carbon allotropes has been discovered with a high potential in several fields, so much so that it has been called "the era of carbon allotropes" as proposed by Hirsch.[3]

The first allotrope of this new series to be discovered was fullerene in 1985, when Smalley and Kroto [4] studied the nature of carbon in interstellar space; It consists of a family of structures where carbon atoms are organized into geodetic conformations that consist of a five- and six-member ring network that allows that structure to close in a sphere. Its hybridization is partially of type sp^3 and sp^2 depending on the number of atoms that constitute it, although, essentially, it is considered sp^2. Fullerenes have high lubricity and good chemical reactivity.

In 1991, S. Ijima discovered the nanotubes when he studied the deposit obtained by an electric discharge of graphite. Carbon nanotubes can be considered as the result of the

coiling of an atomic plane of graphite.[5] This plane can be simple or multiple, which results in single wall or multiple wall nanotubes. The nanotubes behave as electrical conductors, semiconductors or insulators depending on the way they are wound with respect to the direction of a specific axis in the graphitic plane. This property is known as chirality. Its sp^2 hybridization provides them with a high resistance -10 times greater than that of steel-, low density, great flexibility, hardness and excellent thermal conductivity.

Finally, and as the most unexpected discovery of all due to the predicted theoretical non-existence of two-dimensional crystals, in 2004 a group of scientists led by Andre Geim and Kostya Novoselov [6] managed to isolate and identify graphene from a graphite crystal, where they used a technique called micromechanical exfoliation that is based on the weakness of the van der Waals type bonds with which the graphene sheets that make up the graphite interact and which consists of the repeated exfoliation of the piece of graphitic crystal using an adhesive tape.

Today, three types of carbon allotropes can be clearly recognized [7]:

- Structures with sp^3 hybridization such as diamond and lonsdaleite (a form detected in meteorites).
- Structures with sp^2 hybridization such as graphite and graphene, among others.
- Structures with sp hybridization or hybridization mixtures such as carbines and fullerenes, respectively.

2. Graphene

Graphene is a nanosized two-dimensional structure of strongly cohesive carbon atoms on a uniform, slightly flat, undulating, thick-walled, honeycomb-like surface due to its hexagonal atomic configuration. [8] This sheet, composed of benzene rings without their hydrogen atoms, is considered the basis for the understanding of properties in other carbon allotropes. [9] With the exception of diamond, graphene can be visualized as the building

block from which all other allotropes are formed (Figure IV.2); this two-dimensional plane can be wrapped like a balloon liner that provides fullerenes; cylindrically rolled to form nanotubes; or superimposed three-dimensionally to produce graphite.

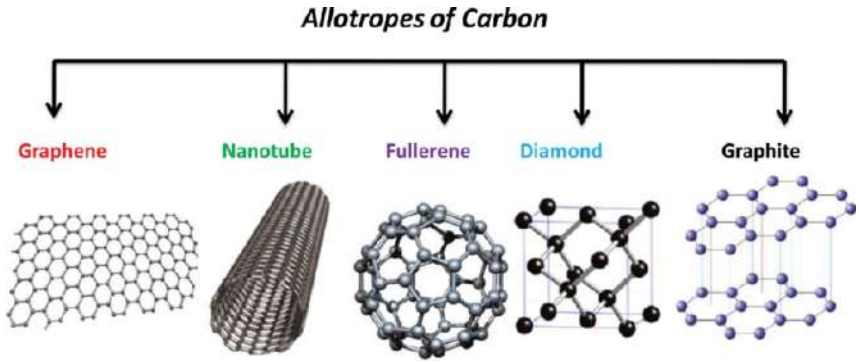


Figure IV. 2 Allotropes of carbon with graphene as a building block for all other allotropes. *Taken from* [10]

Graphene in stacked layers constitutes laminar graphite and began to be widely used in the 60s of the 16th century. [11] Graphene has been studied theoretically since 1947 by P. Wallace, [12] later in 1956 by J. McClure [13] and in 1984 by G. Semenoff. [14] However, Peierls [15, 16] and Landau [17] showed that, in the standard harmonic approach, [18] thermal fluctuations should destroy the long-range order, which would essentially result in the merging of a 2D network into any finite temperature towards a 3D Network. In addition, Mermin and Wagner demonstrated that there could not be a long-range magnetic order in one and two dimensions. [19] Therefore, it was thought that the experimental production of graphene sheets would not be possible. It was not until 2004 that Geim and Novoselov experimentally obtained a graphene layer; [6] In addition, other two-dimensional materials were found, such as boron nitride and molybdenum disulfide. [20, 21] It was observed that these materials were continuous and with high crystalline quality. [22, 23]

The conciliation of the existence of crystals of atomic thickness with the theory is based on the argument that the crystals of said characteristics are stabilized in a metastable state at

the moment of their exfoliation and the formation of wrinkles on the exfoliated surfaces. The small surface of these materials (<< 1 mm) and their strong interatomic bonds mean that thermal fluctuations do not generate dislocations or other crystalline defects, even at high temperatures. [24, 25] Otherwise, it can be understood that the two-dimensional crystals, extracted from their corresponding three-dimensional structures, become intrinsically stable from the generation of wrinkles (a soft wrinkle) in the third dimension in a lateral scale of the order of 10 nm. [26] This three-dimensional deformation results in an increase in the elastic energy of the material, but suppresses thermal vibrations that, at a certain temperature, can minimize the total free energy. [27]

However, it is important to note that structures similar to graphene, such as the intercalation of compounds in graphite sheets (GIC), graphene oxide (GO) and reduced graphene oxide (rGO), were already known much earlier. In 1840 Schafhaeutl, reported the insertion of acid or alkali metal between the carbon sheets and the exfoliation of graphite with sulfuric acid and nitric acid. [28] Later, in 1859 Brodie, [29] in 1899 Staudenmair [30] and in 1958 Hummers [31] also produced GO by exfoliating the graphite with strong oxidizing agents. In 1962, Boehm (who proposed the term "graphene" in 1986 as a combination of the word graphite and the suffix -ene, referring to polycyclic aromatic hydrocarbons) and collaborators reported for the first time laminar carbon containing a small amount of hydrogen and oxygen by chemical reduction of GO dispersions in alkaline media diluted with hydrazine, hydrogen sulphide or iron (II) salts. [32] The thermal reduction of the GO was also published by the same group in the same year. [33]

The word graphene today is often used to refer to a material composed of few leaves, comprising one to 10 overlapping layers and in which their properties are a function of their dimensionality. Taking as a discriminatory basis the specificity of its properties, graphene can be classified according to the number of layers stacked, the size and the C/O ratio, as proposed by Wick, [34] Figure IV. 3.

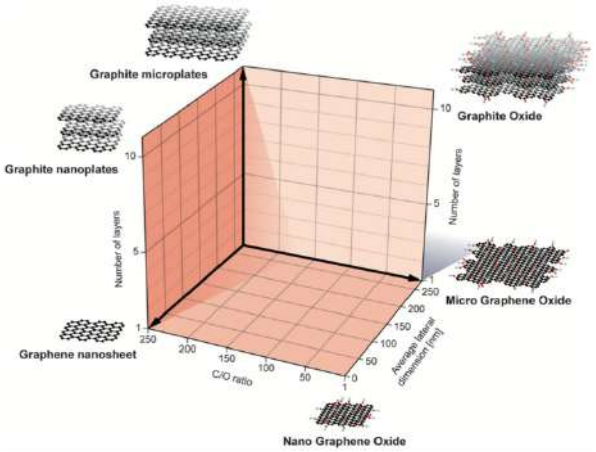


Figure IV. 3 Classification grid for the categorization of different graphene types according to three fundamental properties: number of graphene layers, average lateral dimension, and atomic carbon/oxygen ratio. *Taken from* [34]

Graphene since its discovery has aroused great scientific interest due to its remarkable properties; [35, 36] it is an excellent electrical conductor [37] and thermal, [38] transparent, [39] elastic, [40, 41] highly impermeable, [42, 43] extremely strong [41] and one of the finest 2D materials. [43]

2.1. Methods of obtaining graphene

As indicated above, graphene in free state was obtained for the first time in 2004 by micromechanical exfoliation. The micromechanical exfoliation technique consists of subjecting the clean, new surface, smooth of a graphite crystal, to a fine scraping, from top to bottom, using any object with a solid surface or, by means of a repeated peeling with an adhesive tape until the thinnest leaflets are extracted. Most of the extracted leaflets are three-dimensional, that is, they are graphite; however, some are also two-dimensional, that is, graphene. To tentatively identify the latter, optical microscopy is used, taking advantage of the characteristic of two-dimensional crystallites to be visible in the upper part of a thin sheet of silicon oxide and produce a weak contrast of color interference with respect to an empty sheet. [44] Although this procedure provides large graphene crystallites (up to 100 μm) of high quality that satisfy the needs of fundamental studies and electronic applications, the

performance is extremely low and, being a manual process, the obtaining and identification of material is considerably laborious for this reason, other methods to obtain profitable graphene yields are currently being developed and refined. These methods, in broad strokes, can be classified into two main approaches: top to bottom and bottom to top.

Top-down **approach:** this method of manufacturing nanostructures is initiated from a bulk material and involves the removal or reformation of atoms to create the desired structure at the nanoscale. [45] Although intrinsically simpler than the *bottom-up* approach, the main disadvantage of this technique is imperfection in the surface of the structure. These imperfections generated during the process could have a significant impact on the physical properties and chemistry of the surface because the surface/volume ratio in the nanostructures is very large.

Bottom-up **approach:** in this process, atoms, molecules and even nanoparticles can be used as building blocks for the creation of complex nanostructures. By altering the size of the blocks and controlling their organization and assembly, this approach offers a greater opportunity to obtain structures with fewer defects, with a more homogeneous chemical composition and with greater order. The process is, in essence, highly controlled and involves a complex chemical synthesis. [46]

Applying this criterion, the bottom-up approach for the production of graphene allows to synthesize it through a wide variety of methods, among which are chemical vapor deposition (CVD), arc discharge and epitaxial growth in carbide. silicon (SiC), reduction of CO, the opening of carbon nanotubes and self-assembly of surfactants. The nature of the leaves obtained by this approach is, in general, of high quality; there is also a fine control of the size and thickness of the sheets, however, the yields are low and the production costs are very high. [47]

In the top-down process, graphene sheets or modified graphene sheets are produced by separation or exfoliation of graphite or graphite derivatives. Since graphite is relatively inexpensive and available in large quantities, this process has received the most attention with respect to the large-scale production of graphene. [48] The production of graphene by direct exfoliation of graphite comprises micromechanical exfoliation, exfoliation by ultrasound in the presence of polyvinylpyrrolidone, assisted electrochemical functionalization with ionic liquids and dissolution in superacids.

2.1.1. Obtaining graphene from graphite oxide

Graphite oxide was prepared for the first time in 1859 by Brodie. In the formation of this derivative, the graphite is subjected to reaction with strong oxidizing agents such as potassium perchlorate ($KClO_3$) in acid medium (H_2SO_4/HNO_3). Future modifications were made by W. S. Hummers and R. E. Offeman [31] in 1957 who synthesized graphite oxide in shorter times and more safely. After the oxidation process, a material with a laminar structure similar to graphite is obtained, however, the basal planes that constitute this structure are sheets of graphene oxide that contain oxygen functionalities. [49, 50] The presence of these functional groups makes the sheets highly hydrophilic and causes the van Waals interactions between sheets to weaken allowing the introduction of water molecules between the sheets. The increased distance between sheets and their hydrophilicity allows graphite oxide to be easily exfoliated in water and in various polar organic solvents by the application of external energy such as ultrasonic vibration. [51, 52] The colloidal dispersions thus obtained are constituted by simple sheets of graphene oxide, stabilized by the electrostatic repulsion coming from the negative charge they acquire in dispersion due to the ionization of the hydroxyl and carboxyl groups located on the planes and at their ends (Figure IV.4.). [53]

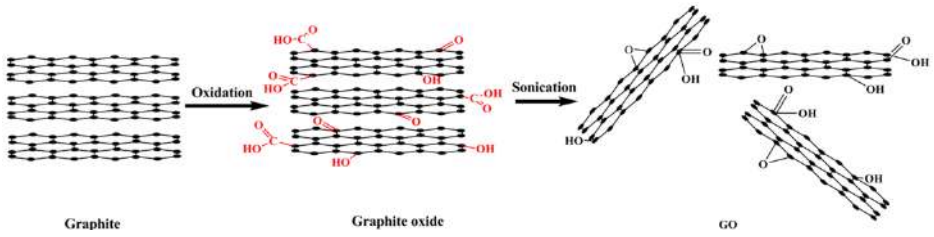


Figure IV. 4 The oxidation of graphite and the exfoliation of graphite oxide to obtain graphene oxide. *Taken from* [54]

The elucidation of the graphene oxide structure has been the subject of several studies, [55] however, the Lerf-Klinowski model is the one that is believed to best describe it. In this model, graphene oxide is delineated as a material constructed by unoxidized aromatic segments of different sizes, which are separated from each other by oxidized regions containing epoxy and hydroxyl groups on the surface of their planes and carbonyl and carboxyl groups located probably at the ends of the leaves [56] as can be seen in Figure IV.5.

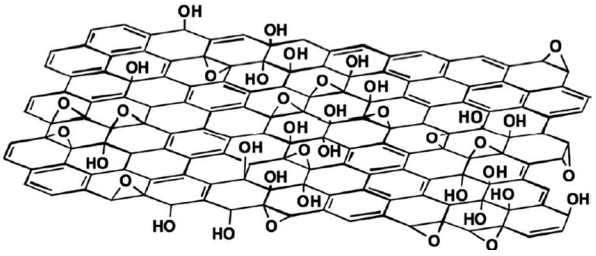


Figure IV. 5 A proposed schematic (Lerf–Klinowski model) of graphene oxide structure. *Taken from* [56]

The presence of oxygenated functional groups causes the rupture of the graphitic mesh, which causes the graphene oxide to behave electrically as an insulator. In order not to diminish the electronic applications of graphene, it is possible to restore the electrical conductivity of the leaves by restoring the π system through different reduction methods, which have been used satisfactorily and can be classified, in general, in chemical reduction and thermal reduction. [57]

2.1.2. Chemical reduction of graphene oxide

Colloidal graphene oxide suspensions can be chemically treated using various reducing agents, such as sodium borohydride ($NaBH_4$) [58, 59] and hydrazine (N_2H_4), [51, 60-62] as the most commonly used. Although this route is efficient for the production of chemically reduced graphene sheets, the toxic nature and cost of the reducing agents have led to the investigation of alternative routes. Table IV.1, shows some alternative methods used for the reduction of graphene oxide.

Table IV. 1 Reducing agents for graphene oxide towards chemically reduced graphene oxide.

Reducing agents	C/O ratio	Conditions	Ref.
L-Ascorbic acid	-	RT, 48 h	[63]
L-Ascorbic acid/NH_3	12.5	368 K, 15 min	[64]
Gallic acid	5.3	368 K, 6 h	[65]
Thiophene	10.9	353 K, 24 h	[66]
Thiourea	5.6	368 K, 8 h	[67]
Glycine	11.2	368 K, 36 h	[68]
Zn/H_2SO_4	21.2	RT, 2 h	[69]
Zn/HCl	33.5	RT, 1 min	[70]
Al foil/HCl	21.1	RT, 20 min	[71]

The reduction degree of graphene oxide or oxidation degree of graphene has certain influences on their properties, such as electrical conductivity, catalysis activity and semi-conductive band positions. [72-74] That is why depending on the reduction route followed, it is possible to control the reduction of graphene oxide. [75] It is well known that the oxygenated functional groups on GO sheets mainly consist of hydroxyl, carboxyl and epoxy groups. [76] In theory, these functional groups should have different reaction activities.

2.1.3. Functionalization of graphene oxide and reduced graphene oxide

The epoxide and hydroxyl groups located on the surface of the graphene sheets (graphene oxide or reduced graphene oxide) and the carboxylic acids located at their edges act as chemical anchoring sites for several organic and inorganic molecules. The introduction of specific molecular species in graphene can be obtained through two approaches: the formation of covalent bonds or the non-covalent interaction. [77]

Covalent interaction: The covalent attachment of a molecule on the surface of graphene involves the breaking of the bonds with sp^2 hybridization and the formation of sp^3 bonds. During this process, unpaired electrons are generated that cause a chain reaction from the starting point of the covalent bond and over the conjugate network, thus improving reactivity. Another important aspect to consider is the geometry of certain regions in the graphene sheet because, depending on the configuration of its edges ("zig-zag or armchair"), the reactivity in the area is favored or not. In parallel, Dreyer and his colleagues explain that this type of functionalization can occur through particular mechanisms, in carboxyl groups or in epoxies. [78, 79] The functionalization reaction in the carboxylic acids typically requires a prior activation and the subsequent addition of nucleophilic species to produce the covalent bond through the formation of amides or esters. On the other hand, the epoxide groups, located in the basal planes of graphene, can be easily modified by ring opening reactions. This reaction involves the nucleophilic attack by an amine.

Non-covalent interaction: The non-covalent interactions are based on the π-π stacking of aromatic molecules in the graphene sheet; in van der Waals type interactions; and about π-ionic interactions. The advantage of this type of functionalization is that there is no break in the conjugate network π and that both graphene and oxidized graphene can have this type of π-π stacking.

In addition to containing oxygenated groups that can confer a certain degree of acidity, the advantage of functionalizing the graphene oxide or the reduced graphene oxide has caused this material to be used as a catalyst in a wide series of reactions. From a broader perspective, the unique properties inherent to well-defined 2D nanomaterials, such as graphene and graphene oxide (GO), are suitable for facilitating a wide range of transformations and may offer extraordinary potential in the design of novel catalytic systems. [80]

3. Graphene oxide as a catalyst

Graphene oxide possesses interesting and potentially useful reactivity, such as its ability to function as an oxidant and/or acid. [78] This solid can be used directly as a catalyst or as a support for metals, oxides and other chemical functionalities.

Bielawski and co-workers revealed the potential of harnessing the reactivity of GO for various synthetic reactions. [81] The authors demonstrated the efficient oxidation of benzyl alcohol to benzaldehyde (conversion >90%) in the presence of GO as a heterogeneous catalyst. Overoxidation to benzoic acid was observed in only minimal amounts (7%) and only under certain conditions (e.g. at elevated temperatures). Interestingly, this and other oxidation reactions of alcohols were performed under ambient conditions and did not proceed under a nitrogen-blanketed atmosphere, which suggests that oxygen may be functioning as the terminal oxidant. [80]

Loh and co-workers also used graphene oxide in oxidation reactions with the oxidative coupling of amines to imines (up to 98% yield at 5 wt% catalyst loading, under solvent-free, open-air conditions). [82] In this case, the carboxylic groups at the edges of defects, along with the localized unpaired electrons, work synergistically to trap molecular oxygen and the amine molecules, thus facilitating intermolecular arrangements.

Sometimes, not only the oxygenated functionalities present in the graphene oxide are responsible for the catalytic activity, but the method to obtain it also plays an important role. For example, Garcia demonstrated that the GO obtained through the standard oxidation of graphite hummers was a highly efficient reusable heterogeneous catalyst for the acetalization of aldehydes. [83] The analytical and spectroscopic evidence suggests that the sulphate groups introduced spontaneously during the oxidation of Hummers are the sites responsible for the catalysis. The presence of these sulfate groups were also able to promote the ring opening reaction epoxides at room temperature. [84]

For his part Zhu, reported the use of GO as a catalyst in the production of alkyl levulinates by alcoholysis and esterification. [85] The control experiments and characterization results revealed that SO_3H groups were the dominant active sites, while the surface carboxyl groups worked synergistically to adsorb furfuryl alcohol.

The own acidity and the possible functionalization with acidic groups on the surface of graphene oxide, has aroused great interest among the scientific community and proof of this are the multiple reports of its use as an acid catalyst.

Gao and co-workers, showed that GO is a high active catalyst towards glycerol esterification (with acetic acid) to valuable bioadditives. [86] The excellent performance of GO, complete glycerol conversion with 90.2% combined selectivity to di- acylglycerol and tri- acylglycerol, was mainly attributed to the rich SO_3H groups and unique lamellar structure.

Liu and co-workers, synthesized graphene oxide and increased its surface acidity by inserting sulfate groups (-HSO_3) on the surface by hydrothermal sulfation with concentrated sulfuric acid. [87] The resulting catalyst (G-SO_3H) was used in the esterification of acetic acid with cyclohexanol, the esterification of acetic acid with 1-butanol, the Peckmann reaction of resorcinol with ethyl acetoacetate, and the hydration of propylene oxide. In all these

reactions the catalyst showed to be very active, in addition to being recyclable and very stable.

Upare and co-workers, reported the use of heterogeneous graphene oxide (GO)-based catalysts with sulfonic acid (SO_3H) functional groups (GO–SO_3H) were used for the selective decomposition of the hexose sugars, glucose and fructose into levulinic acid (LA), achieving yields of around 78% for LA and showed good reuse compatibility with reliable performance. [88]

In many of the studies in which graphene oxide or functionalized graphene oxide were used, the authors highlighted its great thermal stability and its great chemical stability, since it can be reused in several reaction cycles without loss of activity, which means that this solid is a promising catalyst. A great advantage of this catalyst is that it is tolerable to water.[89]

4. Motivation of the study of graphene oxide in the etherification of glycerol with tert-butyl alcohol

As seen in the previous chapters, the etherification of glycerol with *tert*-butyl alcohol requires acidic Bronsted sites in the catalyst to promote the reaction. According to the review of the literature, graphene oxide has been shown as a catalyst of acidic characteristics that it is also possible to functionalize to increase its acidity. Another notable feature is that it can tolerate water without loss of catalytic activity, a crucial factor in the etherification of glycerol with *tert*-butyl alcohol, since it is a by-product. In several reports has also studied the thermal stability, finding that it can get to withstand temperatures close to 473 K, which would make it a catalyst of greater stability than the acid resin Amberlyst® 15 (catalyst reference). In the same review of the literature, there are no reports to date on the use of graphene oxide in the etherification of glycerol with tertiary butyl alcohol, making this thesis to be the first research where it is studied.

5. Objective of the use of graphene oxide in the etherification of glycerol with *tert*-butyl alcohol

When we visualize the non-existence of studies in which graphene oxide is used as a catalyst in the etherification of glycerol with *tert*-butyl alcohol, we intend to study this carbocatalyst in this system. To achieve this purpose, the synthesis of graphene oxide will be carried out using the modified Hummers method and, subsequently, a chemical reduction treatment will be carried out in three different routes, followed by functionalization with sulphonic acid groups. A complete study of the characterization of the solids in parallel will be carried out to relate the physicochemical properties with their catalytic behavior in the etherification reaction.

6. Experimental section

6.1. Chemical and catalysts

Glycerol (99%) and *tert*-butyl alcohol (99.4%) were obtained from Fisher and Merck respectively. Commercial activated carbon (G60) was obtained from Darco. Amberlyst® 15 (dry) ion-exchange resin was purchased from Across Organic. Graphite powder (<20 μm, synthetic) was obtained from Sigma-Aldrich. The preparation of catalysts based on graphene oxide is described below:

Preparation of graphene oxide

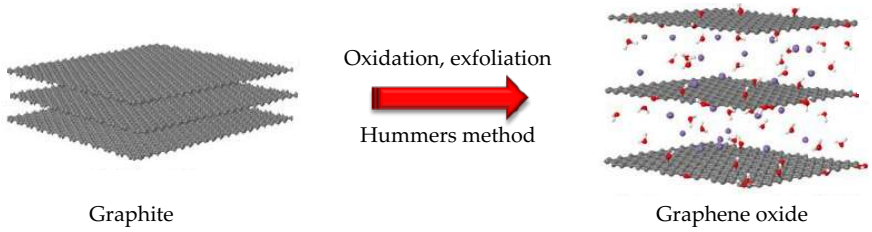


Figure IV. 6 Representation of obtaining graphene oxide from graphite.

Graphene oxide was synthesized from graphite powder by Hummers method modified as originally presented by Kovtyukhova, *et al.* [31, 90] Graphite powder (2.01 g) was mixed with

of concentrated sulfuric acid (5 mL), potassium persulfate (2.04 g) and phosphorus pentoxide (2.03 g). The resulting mixture was heated at 353 K for 2 h. Then, the solid was filtered through a using a 0.2 micron Nylon Millipore filter and washed with deionized (DI) water (100 mL), MeOH (200 mL) and Et_2O (200 mL). The resulting black paste (2.16 g) was dried at 313 K for 12 h. The pretreated graphite (2.16 g) was mixed with sulfuric acid (55 mL) at 273 K and potassium permanganate (7.47 g) was then added by portion with careful attention. The reaction mixture was stirred at 308 K for 2 h and then the reaction mixture was cooled to 273 K, followed by the addition of 30% hydrogen peroxide (6 mL) in DI water (80 mL). The solid was centrifuged (4000 rpm, 30 min) and the liquid phase was removed. DI water (4 x 50 mL) was added and the centrifugation (4000 rpm, 20 min) was performed three times. The same procedure was carried out with MeOH and Et_2O. The resulting brown solid (3.6 g) was dried at 313 K for 12 h. The solid brown obtained for this method was named (GO). To show the synthesis procedure in a clearer way, Figure C.1 of the annex C shows the synthesis scheme.

Reduction of graphene oxide

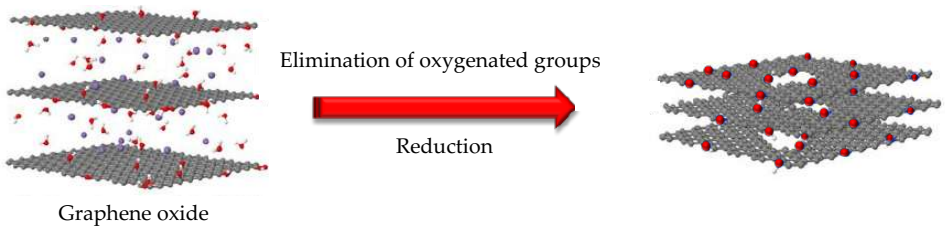


Figure IV. 7 Representation of obtaining reduced graphene oxide.

The reduction of graphene oxide was carried out by three different routes: with hydrazine dihydrochloride, ascorbic acid and Zn/HCl. For the first route, graphite oxide synthetized (1.00 g) was sonicated in deionized water (500 mL) for 2 h. Na_2CO_3 (3.03 g) was added in order to increase the pH up to 9-10. Then, hydrazine dihydrochloride (30.00 g) was added to the suspension and the mixture was refluxed for 24 h. The solution was cooled down to room temperature (293 K) and filtered through Millipore membrane (filters nylon 0.45 mm, 47 mm) and washed with deionized water (100 mL), MeOH (200 mL) and Et_2O (200 mL).

The black powder (0.82 g) was dried at 333 K for 12 h. The solids obtained by this route was named (GO)R_H. For the reduction with ascorbic acid, GO (0.51 g) was sonicated in deionized water (600 mL) for 2 h. Then, ascorbic acid (164.0 g) were added at 353 K under stirring for 2 h. The solution was cooled down to room temperature (293 K) and filtered through Millipore membrane (filters nylon 0.45 mm, 47 mm) and washed with deionized water (100 mL), MeOH (200 mL) and Et_2O (200 mL). The black powder (0.32 g) was dried at 333 K for 12 h. The solids obtained were named (GO)R_A. Finally, for the reduction with Zn/HCl, GO (0.50 g) was sonicated in deionized water (500 mL) for 2 h and acidified (pH=1.9) with concentrated HCl. Then, zinc powder (1.02 g) was added at room temperature (298 K) under stirring for 10 min, follow of the addition of concentrated HCl (125 mL). After of 1 h, the black solid was filtered through Millipore membrane (filters nylon 0.45 mm, 47 mm) and washed with deionized water (1.5 L). The black powder (0.27 g) was dried at 333 K for 12 h. These solids were named (GO)R_Z. To show the synthesis procedure in a clearer way, Figure C.2 of the annex C shows the synthesis scheme.

sulfonation of reduced graphene oxide

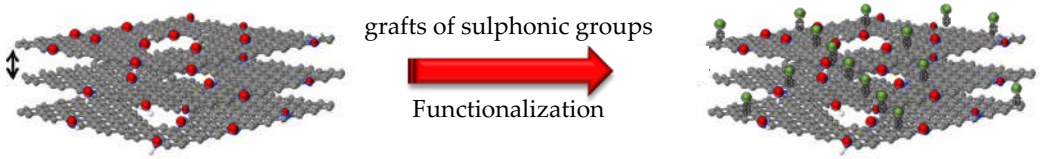


Figure IV. 8 Representation of obtaining sulfonated reduced graphene oxide.

The graphene oxide synthetized (GO) as well the reduced graphene oxide (GO)R_H, (GO)R_A, and (GO)R_Z, were sulfonated through 4-benzenediazoniumsulfonate generation *in situ*. For this purpose, the initial solid (0.27 g) was sonicated in deionized water (40 mL) for 2 h. Then, sodium nitrite (0.95 g) and sulfanilic acid (0.80 g) were added to the resulting solution, allowing the formation of the diazonium salt *in situ*, and the reaction was conducted at 298 K for 24 h. The solution was filtered through Millipore membrane (filters nylon 0.45 mm, 47 mm) and washed with 1N HCl (100 mL) and acetone (300 mL). The black powder was dried at 313 K at 333 K for 12 h. The resulting samples were named (GO)-S, (GO)R_H-S, (GO)R_A-S,

and (GO)Rz-S. To show the synthesis procedure in a clearer way, Figure C.3 of the annex C shows the synthesis scheme.

6.2. Characterization

The characterization of materials based on graphene oxide has been categorized into three main properties that will be essential to understand the performance of these catalysts in the etherification of glycerol with *tert*-butyl alcohol: i) textural properties, ii) elemental analysis and iii) acidity. The fundamentals of each characterization technique useful for carbocatalysts were detailed in the first chapter of this thesis.

6.2.1. Textural properties

Nitrogen adsorption-desorption: Surface area measurements with nitrogen adsorption were performed with a TriStar II plus. The samples were outgassed at 3 mTorr and 423 K for 12 h prior to analysis.

Transmission electron microscopy (TEM): Characterization by transmission electron microscopy (TEM) was carried out on a JEOL JEM-2011TEM. To prepare samples for the TEM study, graphene derived samples were dispersed in ethanol, and deposited onto copper grids.

Scanning electron microscopy (SEM): Scanning electron microscopy images (SEM) were obtained on a JEOL JSM-790CF microscope.

X-ray diffraction (XRD): X-ray powder diffraction (XRD) patterns were recorded at room temperature on Empyrean X-ray diffractometer (Malvern Panalytical Ltd., Royston, UK) operating with Cu Kα radiation (λ = 0.15418 nm) with a scan speed of 1° min^{-1} and a scan range of 5–65° at 30 kV and 15 mA.

Raman spectroscopy: Raman spectroscopy was performed using a Raman HORIBA JOBIN YVON Labram HR800UV confocal microscope equipped with a Peltier cooled CCD detector. The exciter wavelength is 532 nm. The laser power delivered to the sample was 0.02 mW (use of an optical density filter). The device was equipped with an Olympus confocal microscope that allows working backscatter. A diffraction grating with 600 lines.mm^{-1} was used and the opening of the confocal hole is 200 µm. The spectral resolution was 1.5 cm^{-1}. The spectrometer was calibrated with a silicon sample. The LabSpec 5 software allows the acquisition and processing of results.

6.2.2. Chemical composition

Elemental analysis: The contents of carbon, hydrogen, oxygen and sulfur (C,H,O and S) in graphene-based catalysts were obtained with an elemental analyzer NA2100 Protein, Thermoquest Instruments.

X-ray Photoelectron Spectroscopy (XPS): XPS was performed in a high vacuum chamber (pressure ≤ 9.0 ×10^{-8} Pa) on a Kratos Axis Ultra DLD spectrometer equipped with a monochromatic radiation source Al Mono ($Al_{k\alpha}$: 1486.6 eV) operating at 150 W (15 kV and 10 mA). Survey spectra were recorded with a step of 1 eV (transition energy: 160 eV). Based on the collected basic information, high-resolution XPS spectra were collected at a step of 0.1 eV (transition energy: 20 eV).

6.2.3. Acid properties

Boehm titration: 0.1 g of catalyst was added to 20 mL of 2 M NaCl solution. After 24 h of stirring at room temperature, the solution was titrated with 0.1 M NaOH solution. The number of acid sites was then calculated from the amount of NaOH required in the titration. This method has been commonly used in previous studies, correlating the loading of SO_3H calculated by elemental analysis. [91-93]

6.3. Etherification of glycerol with *tert*-butyl alcohol and analysis

Etherification experiments were performed in a batch reactor (described in chapter 3).

The reaction products were analyzed by gas chromatography using a chromatograph model Agilent 6890, DB-WAX column and a FID detector and butanol (Sigma Aldrich) as internal standard. The analyzes were performed using the temperature program and the equations described in chapter 3.

The carbon balance with respect to glycerol was close to 97 % for all the catalysts.

7. Results and discussion

In this section, the results and their respective discussion will be presented following the order established in the experimental procedure; the characterization of the solids and, subsequently, their application as catalysts in the etherification of glycerol with *tert*-butyl alcohol.

7.1. Characterization of catalysts

7.1.1. Textural properties

Table IV.2 reports the BET Surface of activated carbon (AC), Amberlyst® 15 (reference catalyst) and graphene oxide (GO) series.

Table IV. 2 Textural properties of Amberlyst® 15 (A-15), graphene oxide and sulfonated reduced graphene oxide.

Catalyst	S_{BET}
(AC)	978
(AC)-S	224
(AC)R_H	919

(AC)R_H-S	163
A-15	53
Graphite	-
(GO)	5
(GO)-S	
(GO)R_H	22
(GO)R_Z	
(GO)R_A	14
(GO)R_H-S	11
(GO)R_Z-S	10
(GO)R_A-S	7

The surface area obtained for activated carbon is characteristic of a microporous solid, where the reduction process leads to a small decrease in the initial value (from 978 to 919 $m^2\ g^{-1}$), while the sulfonation process drastically decreases the surface area, probably because of the obstruction of some pores. [94] As for the Amberlyst® 15, it has an area of 53 $m^2\ g^{-1}$, characteristic of this resin that can have pores of 400 to 800 Å, which makes it a macroporous structure. [95] On the other hand, graphene oxide (GO) sample exhibit N_2 adsorption isotherm typical of nonporous solids and have low surface area with 5 $m^2\ g^{-1}$. The theoretical value for completely exfoliated and isolated graphene sheets is 2600–2700 $m^2\ g^{-1}$, however, the textural properties of GO in the wet/dispersed state differ significantly from those in the dried state, [96] and the restacking of the sheets upon drying leads to a strong decrease in the specific surface area. [97]

A reduction process using hydrazine dihydrochloride (R_H) leads to a small increase in surface area by removing some oxygenated groups from the surface, while sulfonation generates areas in catalysts less than 11 $m^2\ g^{-1}$ for GO reduced and sulfonated solid.

The XRD patterns of graphite, pre-oxidized graphite, (GO), (GO)R_A, (GO)R_H, and (GO)R_Z-S are shown in Figure IV.9.

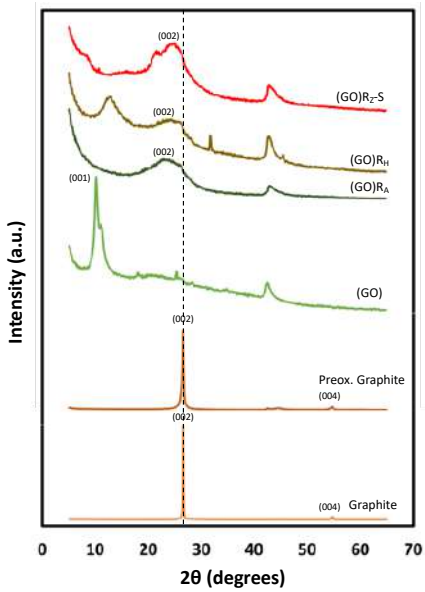


Figure IV. 9 XRD patterns of Graphite, preoxidated graphite, (GO), (GO)R_A, (GO)R_H and (GO)R_Z-S.

According to XRD for the pre-oxidized graphite, it shows no structural changes after treatment with the mixture between concentrated sulfuric acid, potassium persulfate and phosphorus pentoxide, retaining the same very strong [002] peak at 26.57° as the starting graphite, but by XPS (Fig. IV.14) some oxygenated groups were observed. For (GO) appear a [001] peak at 10.13° due to the formation of hydroxyl, epoxy and carboxyl groups. These oxygenated functions introduced onto graphene sheets increased the interlayer spacing from 0.34 nm in graphite to 0.87 nm in (GO) as determined by the Bragg's law:

$$n\lambda=2d_{(002)}\sin\theta \qquad \text{(Eq. 1)}$$

The stacking hight and the layered arrangement were calculated by the Scherrer equation:

$$\tau = \frac{K\lambda}{\beta\cos\theta} \qquad \text{(Eq. 2)}$$

For graphite, the stacking hight and the layered arrangement was 41 nm and 110 sheets respectively for graphite and 10 nm and 12 sheets respectively for (GO). After reduction with ascorbic acid ((GO)R_A), the oxygen- containing functional groups are removed and this

causes the reduced graphene oxide peak to shift to 24.33° and a weak [100] band 2θ = 43.4°. This feature was attributed to the destruction of the layered structure during the exfoliation step and suggests an intermediate crystalline structure between graphite and amorphous carbon that has been called turbostratic structure or random layer lattice structure. [91, 98] For (GO)R_A, the interlayer spacing was 0.37 nm and the stacking hight and the layered arrangement for this solid was 1.13 nm and 3 sheets. With a reduction process using hydrazine dihydrochloride ((GO)R_H) not all oxygen groups are eliminated, for this reason apart from main peak to 2θ = 26.18°, a peak at 13.16° is observed, suggesting that part of the initial structure of GO is maintained after the reduction process with this agent. The interlayer spacing was 0.34 nm for reduced graphene oxide and 0.67 nm for the remaining unreduced graphene oxide. On the other hand, a sulfonation process no affect the structure of the reduced oxide with Zn/HCl ((GO)R_Z-S) where a [002] peak at 25.25° is predominant. Additionally, it has a broad shoulder at 2θ = 22.23°, presumably induced by a bimodal or multimodal character of the interlayer spacing of (GO)R_Z-S powder. [60] The stacking hight and the layered arrangement in this case was 1.41 nm and 4 sheets respectively. This result confirms the successful exfoliation with the reduction and with the respective functionalization.

The Raman spectra of graphite, (GO), (GO)R_H and (GO)R_A are shown in the Figure IV.10. The Raman spectra of the materials confirm the observations of the XRD patterns i.e., the changes of structure during the oxidation process from graphite to graphene oxide. The Raman spectrum of graphite displays a strong peak at 1580 cm^{-1}, corresponding to the G-band and this is attributed to the first order scattering of the E_{2g} phonon of the sp^2 carbon-carbon bond; [99] the Raman spectra of (GO), shows a slight shift of the G-band until 1584 cm^{-1}, and for (GO)R_H, (GO)R_A, the G-band appear around of 1590 cm^{-1}. After oxidation process of the graphite to obtain graphene oxide, the D-band develops, which represents the defect sites associated with vacancies and grain boundaries, [100-102] possibly due to the extensive

oxidation. [51] The D-band around 1355 cm^{-1} is a breathing mode of A_{1g} symmetry involving phonons near the K zone boundary. [103]

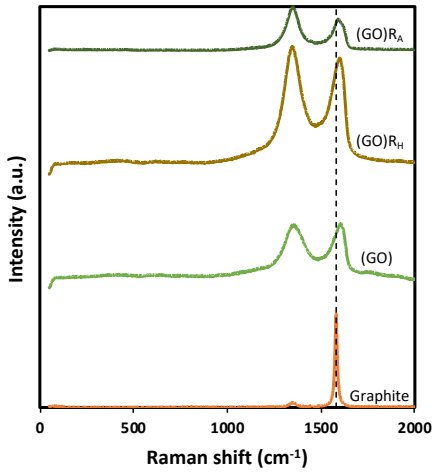


Figure IV. 10 Raman spectra of graphite, (GO), $(GO)R_H$ and $(GO)R_A$.

The morphological characteristics of the samples were investigated by microscopy. Scanning electron microscopy (SEM) images showed that the laminar form of the graphite was not significantly altered by the oxidation processes. The observed corrugation of GO sheets was attributed to the breaking of the planar polyaromatic structure, [91] (Fig. IV.11b). After the reduction process (with ascorbic acid), the restoration of the sheets by the *pi*-interactions between the aromatic carbons is evident, while the ultrasound treatment, accompanied by the sulfonation of $(GO)R_A$, leads to the separation of the layers and a completely corrugated morphology is observed (Fig. IV.11d).

The results obtained from SEM images were supported by transmission electron microscopy (TEM) analyses (Fig. IV.12). The TEM image of the graphite shows dark areas that indicate the existence of several layers of polyaromatic structure. Electron clear regions present in GO, indicate much thinner films of a few layers of graphene oxide. Additionally, GO sample present sizes of 200 to 500 nm. The reduction with ascorbic acid of graphene oxide and subsequent sulfonation does not alter the morphology. On the other hand, the reduction with hydrazine generates large agglomerations, probably due to the combination between

the remaining graphene oxide that was not able to be reduced (determined by XRD) and the reduced layers present. This agglomeration is maintained even after sulfonation.

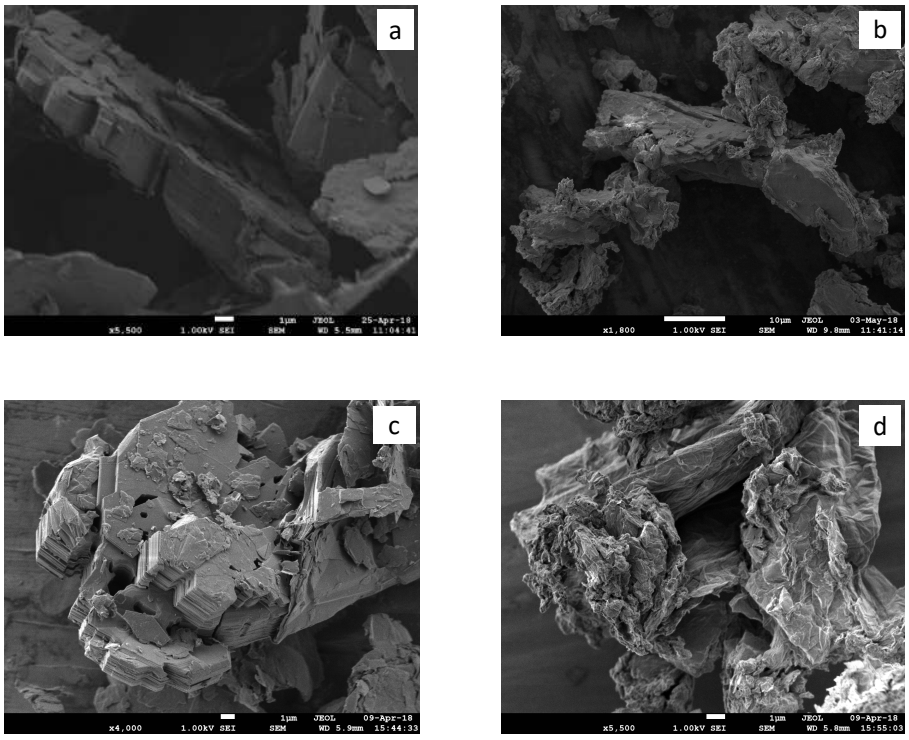
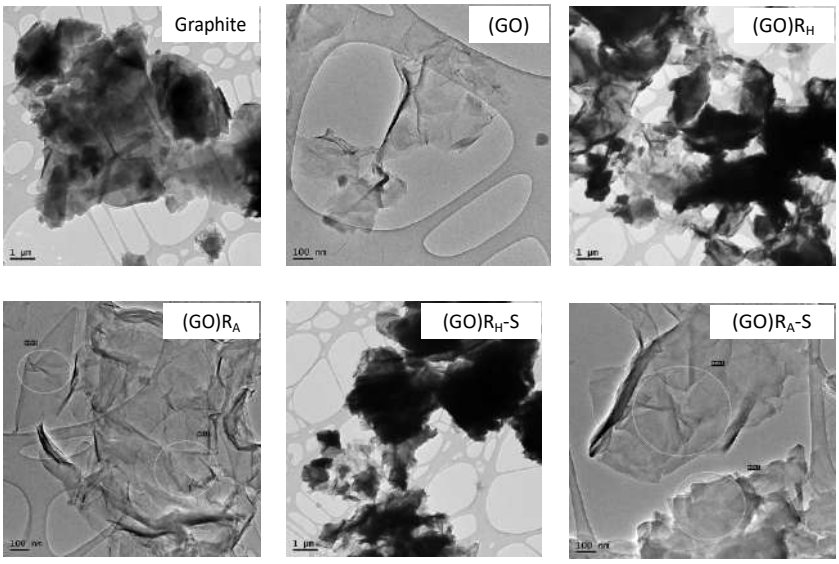


Figure IV. 11 SEM images of: a) graphite; b) (GO), c) (GO)R_A; d) (GO)R_A-S.



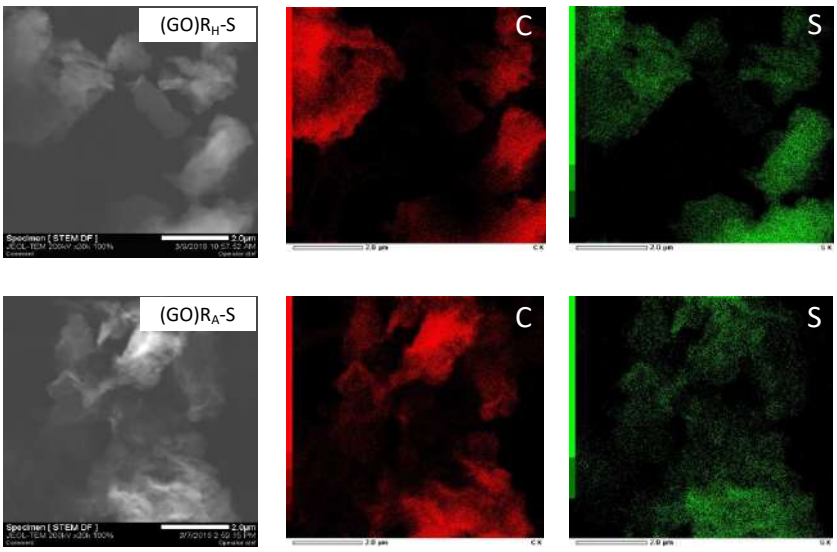


Figure IV. 12 Transmission electronic images of the samples and EDS mapping showing the spatial distribution of C and S of (GO)R_H-S and (GO)R_A-S.

7.1.2. Elemental Analysis

Elemental analysis by combustion was used to investigate the degree of reduction of the powder samples and the degree of sulfonation. Table IV.3 summarizes the results of the elemental analysis, in addition to the determination of the C/O and S/C ratio.

Table IV. 3 Elemental analysis of activated carbon, graphene oxide and sulfonated reduced graphene oxide.

Catalyst	Elemental Analysis (%)			C/O ratio	S/C ratio
	C	O	S		x10^{-2}
(AC)	73.16	24.89	0.00	3.92	--
(AC)-S	67.75	26.29	3.35	3.44	1.85
(AC)R_H	79.39	19.19	0.00	5.52	--
(AC)R_H-S	68.70	25.33	3.94	3.62	2.15
Graphite	97.70	2.30	0.00	56.64[a]	--
(GO)	35.47	60.29	1.45	0.78	1.53
(GO)-S	46.99	47.27	2.37	1.33	1.89
(GO)R_H	66.40	31.40	0.00	2.82	--
(GO)R_Z	93.16	6.86	0.00	18.1	--

(GO)R_A	70.96	27.59	0.00	3.43	--
(GO)R_H-S	60.14	34.82	3.29	2.30	2.05
(GO)R_Z-S	85.13	10.15	4.72	11.2	2.08
(GO)R_A-S	55.86	35.01	6.88	2.13	4.62

[a] Measured by XPS.

The obtained graphene oxide (GO) has a C/O ratio of 0.78, which reflects the good oxidation rate in the material with respect to the starting graphite, which has a ratio of 56.64. When performing the reduction processes in the GO, it is possible to observe notable differences in the ratio of C/O (Figure IV.13).

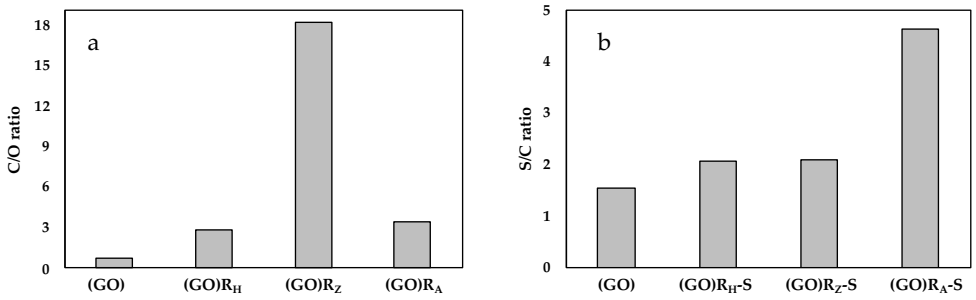


Figure IV. 13 The C/O and S/C ratios of reduced and sulfonated graphene oxide, respectively.

According to our results, the reduction with Zn/HCl was more effective than with hydrazine hydrochloride and ascorbic acid, generating a ratio of 18.1 against a ratio of 2.82 and 3.43 for (GO)R_H and (GO)R_Z respectively. With respect to the S/C ratio, it is possible to observe that the graphene oxide contains residual sulfur, product of the synthesis method in which sulfuric acid was used. [85, 86] This sulfur, which is in the form of sulphate [104] and can be lodged in the middle of the leaves of the GO or forming covalent bonds, [105] moves with the reduction, probably thanks to the restoration of the leaves and the high solubility in water of the sulphate group. In this sense, it can be attributed that the presence of sulfur in solids (GO)R_H, (GO)R_Z and (GO)R_A, is only due to functionalization with sulphanilic acid. The ratio S/C in these solids is greater in the catalyst (GO)R_A, followed by (GO)R_Z and (GO)R_H. Clearly, these results indicate that the method of graphene oxide reduction significantly

influences the degree of functionalization. Probably the little agglomeration of the sheets after the reduction with L-ascorbic acid (Fig. IV.12), helps so that more -$PhSO_3H$ groups can be grafted on the surface.

The XPS spectra of the C1s for graphite, shows a predominant peak at 284.4 eV corresponding to the sp^2 carbon and a small peak at 286.4 eV corresponding to small amounts of C-O-H groups of alcohols or phenols [106] present in the starting material (Fig. III.14a). This same region confirmed that the pre-oxidation treatment of graphite with $K_2S_2O_8/P_2O_5$ (Fig. IV.14b) generated a small number of groups of C-O and C=O groups characterized by the low intensity peaks at 286.4 and 287.7 eV respectively, while the peak represents Csp^2 to 284.4 eV remains intense. The pre-oxidized graphite after of the treatment with $KMnO_4$ an H_2SO_4 leading to the formation of the (GO) solid. In this material it is evident the presence of Csp^3 carbons (284.2 eV) in a high content, as well as the functional groups C-O-C (286.2 eV), C=O (288.2 eV) and O-C=O (289.5 eV), which confirm the formation of graphene oxide (Fig. IV.14c). The reduction of GO by the use of hydrazine dihydrochloride partially restored the aromatic structure of the material, although some oxygenated groups remain in this solid, principally C-O-C (286.6 eV), Figure IV.14d. During the reduction, parts of the basal planes near the edges become reduced and subsequently snap together due to π - π interactions, thus narrowing the interlayer distance. Consequently, the reducing agent, hydrazine dihydrochloride, cannot penetrate further into the interior of the GO particles, presumably leading to the lower degree of reduction [60] and greater agglomeration (TEM images, Figure IV.12). The reduction of the GO by ascorbic acid, led to a greater restoration of the aromatic structure compared with the hydrazine dihydrochloride, since the amount of oxygenated groups after the process was much lower (high C/O ratio), Figure IV.13b. According to Guo *et al.*, L-ascorbic acid can significantly reduce the epoxy and hydroxylic groups, which are the most abundant groups in the GO (Figure IV.15). In addition, a high concentration of L-ascorbic acid, as in our case, can generate oxalic acid and guluronic acids (generated from the decomposition of dehydroascorbic acid) that are able to form hydrogen

bonds with residual oxygen groups and prevent π - π interactions of the graphene sheets, therefore there are no agglomerations, [63] (TEM images, Figure IV.12). The XPS spectrum of (GO)Rz-S (Figure IV.14f and Figure IV.15), show the few oxygenated groups that have been conserved after the functionalization process on the (GO)Rz.

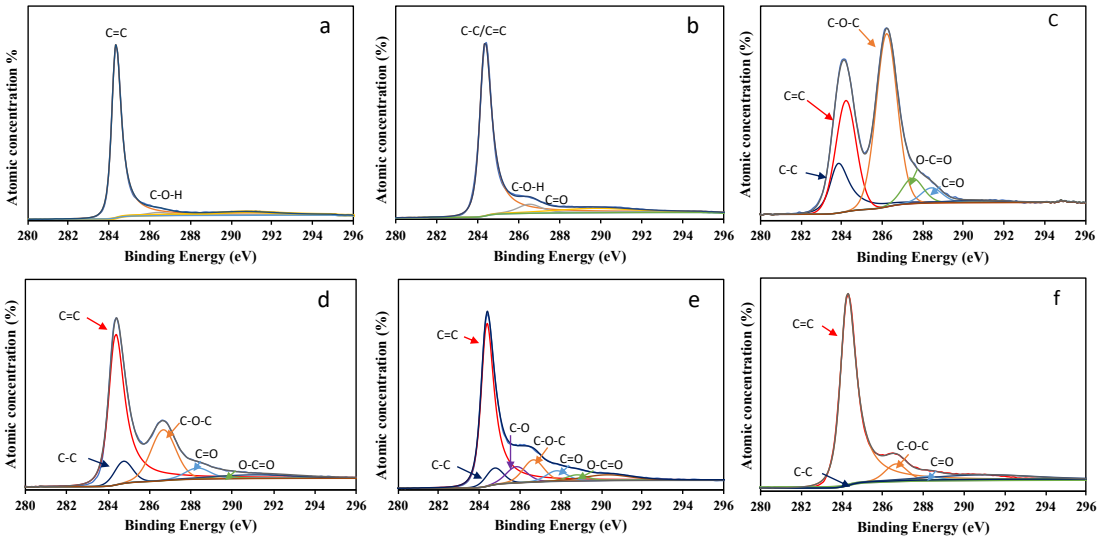


Figure IV. 14 XPS spectra for: a) graphite; b) pre-oxidized graphite; c) (GO); d) (GO)RH; e) (GO)RA; f) (GO)RZ-S.

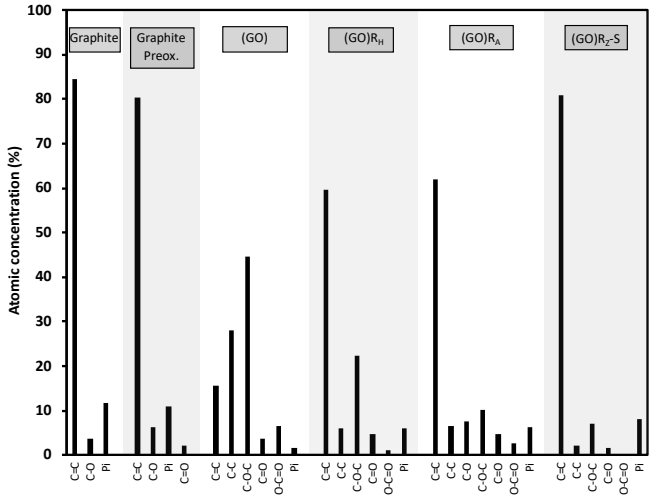


Figure IV. 15 Atomic concentration (%) determined by XPS of graphite, pre-oxidized graphite, (GO), (GO)RH, (GO)RA and (GO)RZ-S.

The quantitative energy dispersive X-ray spectroscopy (EDS) mapping of (GO)R_H-S and (GO)R_A-S, reveals a homogeneous distribution of -$PhSO_3H$ functionalities on the graphite oxide structure, suggesting that they are not exclusively located at the edges, [107] Figure IV.12. For the functionalization of the reduced graphene oxide with the aryl diazonium salt of the sulfanilic acid, it is necessary that a re-hybridization of the C atoms from sp^2 to sp^3, to form a covalent bond. It is also well known that a chemical reduction of graphene oxide generates a substantial amount of defects, including holes, in the basal plane, which are an advantage for the successful grafting of -$PhSO_3H$ groups. [105]

7.1.3. Acid properties

The acidity measurements of the samples were correlated with the number of sulfonic groups (sulfur content) present in the surface and corroborated by the Boehm titration, Table IV.4. This approach has been used in other studies that find concordance between the results for sulfonated reduced graphene oxide. [91, 108] For the activated carbon (AC), the total acidity comprises the sulfonic groups and the original oxygenated groups present in this type of material. According to Cordoba *et al.*[109] activated carbon G60 presents carboxylic acids, anhydrides and lactone groups, which give it surface acidity (0.71 mmol $[H^+]$ g^{-1}). After the sulfonation process, the activated carbon increases the total acidity to 1.76 mmol $[H^+]$ g^{-1}, of which 1.05 mmol $[H^+]$ g^{-1} corresponds to the sulfonated grafted groups. The acidity of the graphene oxide, in both cases, was influenced by the presence of sulfate groups remaining from the graphite oxidation processes: GO exhibited a total acidity of 0.51 mmol $[H^+]$ g^{-1}, of which 0.45 mmol $[H^+]$ g^{-1}corresponded to the sulfonated groups belong to the groups resulting from the functionalization. After the reduction of the graphene oxide, the disappearance of the remaining sulfate groups is evidenced and the acidity determined by the Boehm titration is almost null due to the few acidic oxygenated groups remaining on the surface of the reduced graphene oxide. Finally, the acid values obtained for the reduced sulfonated graphene oxides were the same through the Boehm titration and through elemental analysis.

Table IV. 4 Acidic properties of activated carbon, Amberlyst® 15 (A-15), graphene oxide and sulfonated reduced graphene oxide.

Catalyst	Acidity (mmol $[H^+]$ g^{-1})
(AC)	0.71
(AC)-S	1.05 (1.76)[c]
(AC)R_H	--
(AC)R_H-S	1.23
A-15	2.37[a]
Graphite	--
(GO)	0.45 (0.51)[a]
(GO)-S	0.74 (0.70)[a]
(GO)R_H	--
(GO)R_Z	--
(GO)R_A	--
(GO)R_H-S	1.03 (1.05)[a]
(GO)R_Z-S	1.48 (1.37)[a]
(GO)R_A-S	2.15 (2.12)[a]

[a] In parenthesis = acidity determined by Boehm titration.

7.2. Etherification of glycerol with *tert*-butyl alcohol

According to our previous work with zeolites [110] (chapter 3), we determine the thermodynamics of the etherification of glycerol with *tert*-butyl alcohol by the use of discontinuous reactors at 363 K under autogenous pressure. The etherification of glycerol and *tert*-butyl alcohol is a reaction limited by a thermodynamic equilibrium, and in our experimental conditions the maximum glycerol conversion expected is of 80%.

7.2.1. Kinetic model

The order of reaction for glycerol and *tert*-butyl alcohol were established on the (AS)-S and (GO)R_A-S catalysts at 363 K and estimated from the variation of the initial rate with the concentration of that reactant, using the natural logarithm of the rate equation: $\ln r_0 = lnk + \alpha \ln [\mathrm{Gly}]_0 + \beta \ln [\mathrm{TBA}]_0$. The initial rate are measured in a series of experiments at different initial concentration of Gly ranged from 2.0 $x10^{-4}$ to 1.0 $x10^{-3}$ mol cm^{-3} with a molar ratio TBA/Gly from 10 to 40. In these conditions, the concentration of the exceeding reactant can

be considered as almost invariant. The slope of the straight line in Fig. IV.16 of lnr_0 plot as a function of ln[Gly]$_0$ then corresponds to the partial order with respect to Gly. Similar experiments were carried out by maintaining the concentration of Gly constant and varying that of TBA concentration from 4.0 x10^{-4} to 2.0 x10^{-3} mol cm^{-3}. The partial kinetic orders for (AC) -S with respect to glycerol was 0.16, while the order for TBA was 0.84. For the catalyst (GO)R$_A$-S, the order obtained with respect to glycerol was 0.42, while for the TBA 1.60. These results agree with the results obtained by Frusteri *et al.* [111] where they evaluated the solid-acid resin Amberlyst® 15 in the etherification and the kinetic orders found were an order of 0.3 with respect to Gly and an order of 1.7 with respect to *tert*-butyl alcohol, suggesting that the etherification reaction occurs with a molecular mechanism wherein TBA is quickly protonated on the acid sites forming a tertiary carbocation able to react with the glycerol strongly adsorbed on the catalyst surface. These results are also confirmed by Kiatkittipong *et al*. [112] where they show that in Amberlyst® 15 the model based on the activity of Langmuir-Hinshelwood (LH) is the most suitable kinetic model to adjust to the experimental results.

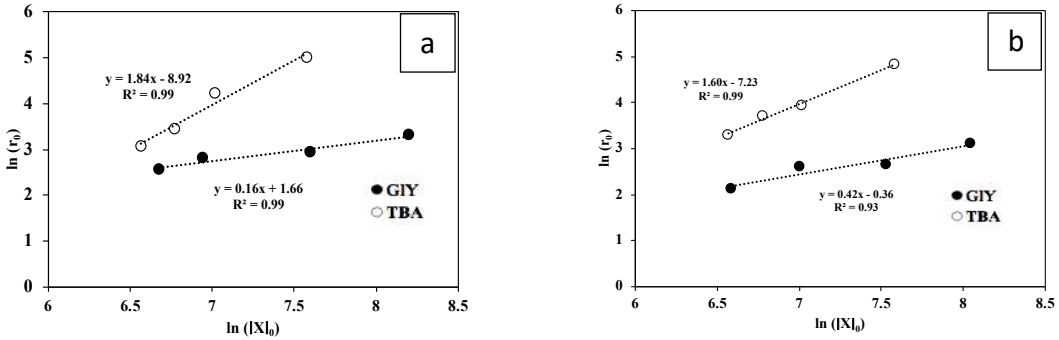


Figure IV. 16 Kinetical study of (AC)-S, a) and (GO)R$_A$-S, b).

7.2.2. Activity

In Figure IV.17, the glycerol conversion has been compared as a function of the reaction time for following catalysts, (AC)-S, (AC)R$_H$-S and Amberlyst® 15 (A-15, reference catalyst [113, 114]), (GO), (GO)-S, (GO)R$_H$-S, (GO)R$_Z$-S, (GO)R$_A$-S. By employing A-15 as the catalyst, the conversion increases rapidly and reaches a plateau at 64% within 1 h. The plateau is 16% lower than the predicted equilibrium value (80%), which means that conversion is

hampered by deactivation of the sulfonic resin, probably due to a product inhibition effect, *e.g*. by H_2O. As expected, the graphite does not present conversion to glycerol because practically the amount of acidic sites is zero in this material (Table IV.4). With the activated carbon (G60) was also used directly, no conversion of glycerol was observed either. This indicates that although this solid has oxygenated groups that can confer acidity, these are not strong enough to promote etherification. After sulfonation of the AC, a conversion of glycerol (35%) was observed, suggesting that the presence of sulfonated groups could promote the reaction (Table IV.5). Subsequently, it was evaluated graphene oxide obtained (GO). The nature of these materials causes them to contain oxygenated groups on the surface that give acidity, as determined by the Boehm titration. However, as evidenced by activated carbon, these groups do not by themselves promote the etherification reaction with glycerol. For the graphene oxides synthesized here, it was found by elemental analysis that they contain sulfate groups remaining from the preparation, which could confer the appropriate acid strength to carry out the reaction. Indeed, one way to functionalize with acid groups is graphene oxide with direct immersion in concentrated sulfuric acid. [87] The conversion of glycerol achieved with (GO) was 19%. A sulfonation of these graphene oxides demonstrates that not only is it possible to increase the conversion, but it also improves the selectivity. (GO)-S achieves 50% of conversion of glycerol. In this study we used three reduction methods to compare the final effects in the etherification of glycerol with *tert*-butyl alcohol, where it is observed that the results are very similar in terms of glycerol conversion. When using sulfonated reduced graphene oxides, an increase of between 23 and 27% conversion of glycerol with respect to the conversion achieved with sulfonated graphene oxide is possible, indicating that the reduction process, before the sulfonation, it is essential to achieve the best results. Table IV.5 summarizes the conversion and selectivity achieved after 10 hours of reaction. The activity of the catalysts also appears in the same Table.

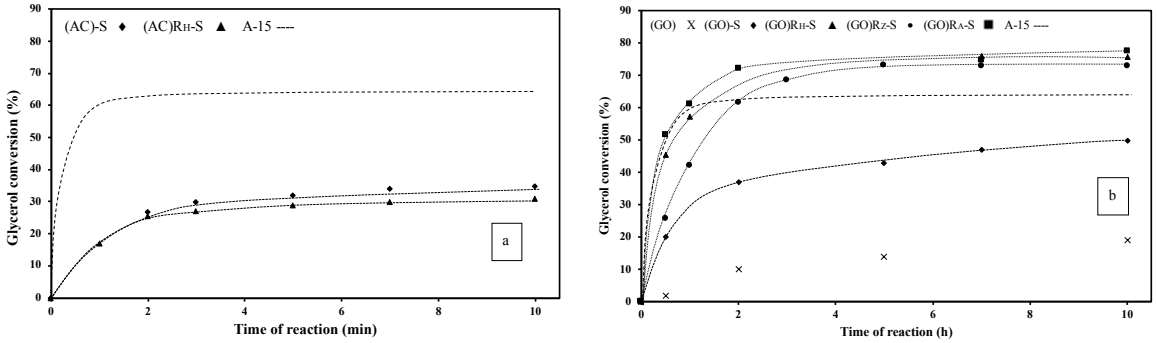


Figure IV. 17 Glycerol conversion as a function of reaction time. (AC)-S, (AC)R_H-S and Amberlyst®15, a); Catalysts based on (GO), b). Test carried out at 363 K, 1200 rpm, autogenous pressure, 7,5 % of catalyst (referred to glycerol mass) and glycerol/*tert*-butyl alcohol molar ratio of 0.25.

Table IV. 5 Glycerol etherification with *tert*-butyl alcohol: conversion and selectivity after 10 h, initial activity (A^0) and TOF obtained on Amberlyst-15, activated carbon, graphene oxide and sulfonated reduced graphene oxide.

Catalyst	Conv. (%)	Selectivity (%)		$A^0_{glycerol}$	TOF[a]
		MTBG	h-GTBE	(mol h^{-1} g^{-1}) **x 10^4**	(h^{-1}) **x 10^2**
(AC)	0	0	0	--	--
(AC)-S	35	80	20	1.45	14
(AC)R_H-S	31	86	14	1.28	10
A-15	64	75	25 (0.3)	15.00	63
Graphite	0	0	0	--	--
(GO)	19	100	0	5.00	111
(GO)-S	50	78	22 (0.2)	10.53	202
(GO)R_H-S	73	71	29 (0.7)	14.02	107
(GO)R_Z-S	76	88	12 (0.1)	12.71	194
(GO)R_A-S	77	73	27 (0.5)	15.89	74

Reaction conditions: 7.5 wt.% of catalyst (referred to glycerol mass), glycerol/*tert*-butyl alcohol molar ratio = 0.25, reaction temperature = 363 K, reaction time = 10 h, stirring = 1200 rpm. MTBG: glycerol monoethers; h-GTBE: glycerol diethers + glicerol triether. In parenthesis, selectivity to glycerol triether (%). [a] Turnover frequency per Brønsted acid sites probed by the pyridine at 423 K.

Results of the catalytic etherification of glycerol with *tert*-butyl alcohol further compared in terms of initial activity (A_0), where possible deactivation does not occur. A_0 was estimated

from the slope of the tangent at zero time fitted to the curves presented in Figure IV.17. The initial activity of the catalyst based on sulfonated reduced graphene oxide is very close to the activity of the sulfonic resin A-15, which indicates that the amount of acidity of these catalysts is sufficient to promote the etherification of glycerol with *tert*-butyl alcohol. The similarity of this activity could be related to the fact that both the Amberlyst® 15 and the graphene-based solids contain the same acidic groups on the surface (-$PhSO_3H$) and there is no microporosity in these catalysts.

7.2.3. Selectivity

The etherification of glycerol with *tert*-butyl alcohol (TBA) proceeds via a consecutive path that yields the formation of water and five different alkyl glycerol ethers, which are MTBG (3-*tert*-butoxy-1,2 propanediol and 2-*tert*-butoxy-1,3 propanediol), DTBG (2,3-di-*tert*-butoxy-1-propanol and 1,3-di-*tert*-butoxy-2- propanol) and TTBG (tri-*tert*-butoxy-propane). Side reactions can occur such as the dehydration of TBA to isobutylene (IB) followed of its dimerization. Under the performed reaction conditions, no diisobutylene is detected and the isobutylene yield estimated from the autogenous pressure is negligible (<1%). Fig. IV.18 compares MTBG (primary product) and the h-GTBG (DTBG and TTBG) molar yields as function of the overall glycerol conversion employing Amberlyst® 15, and sulfonated reduced graphene oxide-based catalyst (GO). Table IV.5 reports conversion and product selectivity obtained after 10 h of reaction.

Using A-15, the yield of the primary product (MTBG) reaches a maximum at ca. 50% glycerol conversion (Table IV.5). The DTBG (secondary product) is starting to be formed at 30% glycerol conversion (extrapolated value at zero conversion). After 10 h of reaction, one quarter of the products are composed of DTBG, whereas the yield of TTBG (ternary product) is negligible (0.3%). For the catalyst (AC)-S, the formation of DTBG occurs at low conversion (~20%). This is related to the high microporosity of activated carbon, where a shape selective/confinement effect can occur. [110] In the case of the sulfonated reduced graphene

oxide- based catalysts, the selectivity toward DTBG is dependent of the method of synthesis: for the catalysts reduced with hydrazine dihydrochloride and ascorbic acid, values of 29 and 27% respectively were obtained (Table IV.5). These solids, which do not have porosity, reach the formation of DTBG before of 30% conversion of glycerol (Fig. IV.18). Although the conversion after 10 h of reaction is similar in the three cases ((GO)R_H-S, (GO)R_Z-S and (GO)R_A-S), the selectivity results obtained with (GO)R_Z-S differ significantly when obtaining a selectivity towards DTBG of 12% (Table IV.5). These results suggest that for these catalysts, it is also important to consider the hydrophobic/hydrophilic balance. While this character has been previously discussed for zeolites in the etherification of glycerol with *tert*-butyl alcohol, [110, 115, 116] this character can also be related to catalysts based on graphene oxide; there is a synergy between the active sites (sulphonic groups) and the oxygen groups, where the latter can act as adsorption sites for reagents and products, particularly glycerol and MTBG, promoting the consecutive reaction MTBG → DTBG → TTBG.

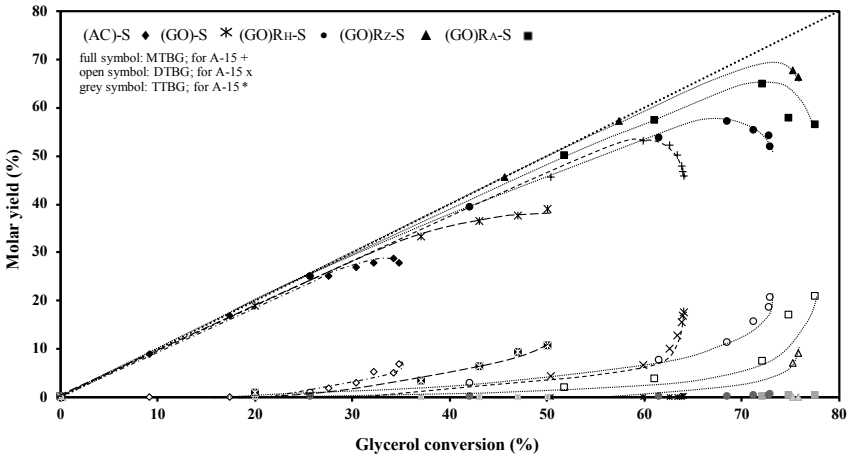


Figure IV. 18 Molar yields into MTBG, DTBG and TTBG as a function of glycerol conversion for catalyst based on sulfonated reduced (GO), compared to A-15 and (AC)-S.

7.2.4. Stability

The recyclability of (AC)-S and (GO)R_A-S has been investigated comparing the percent yield toward DTBG. After being recycled 3 times, the conversion of glycerol using (GO)R_A-S, decreases 11% and the Yield towards h-GTBE decreases more than 50% (going from 22 to

10%), Fig. IV.19. The same effect is observed with (AC)-S, although in this case the conversion decreases only 1%. When the catalysts are subjected to washes with ethanol by means of Soxhlet, it is possible to recover the initial conversion and yield. This suggests the adsorption of reagents and products in the active sites, which are evidenced when analyzing extracts of washing with solvents by gas chromatography, where the main peaks are glycerol and MTBG. These results show that it is possible to recover the initial activity by means of solvent washes, converting the catalysts based on sulfonated reduced graphene oxide, into serious candidates to effectively carry out the etherification reaction between glycerol and *tert*-butyl alcohol.

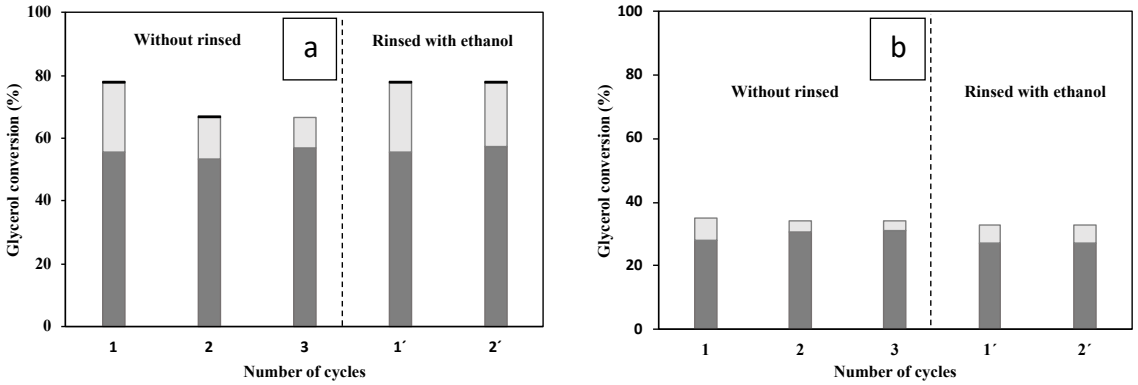


Figure IV. 19 Results of recycling experiments for (GO)R_A-S, a) and (CA)-S, b).

Additionally, a thermal stability study was carried out. Figure IV.20, compares the TGA curves of Amberlyst® 15, (GO) and (GO)R_A-S.

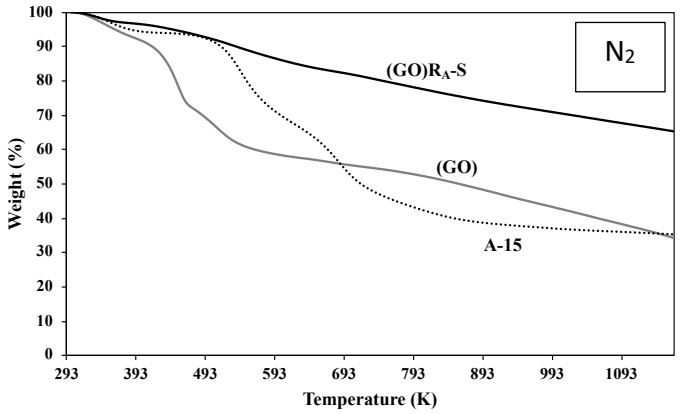


Figure IV. 20 TGA pattern of (GO)R_A-S, (GO) and A-15.

The overall weight loss of 64.5 % for GO occurs in three successive steps. The first one is a steady weight loss of 7.7 % attributed to the vaporization of adsorbed water molecules and occurs at around 393 K. Then a rapid loss of 20% due to the decomposition of the oxygen-containing functional groups such as hydroxyl, epoxy, carbonyl, and carboxyl groups in the temperature range of 393-473 K. Finally, a weight loss of 36.8 % that can be attributed to the combustion of the carbon skeleton is observed in the temperature range of 273–1163 K [117]. TGA curve for (GO)R_A-S show overall less than 35 % weight loss in the same temperature range. A first mass loss of 4.4 % at around 373 K was attributed to volatiles desorption, mainly moisture. A second weight loss of 11.8 % at around 648 K that can be attributed to the decomposition of remnants oxygen groups (hydroxyl, epoxy, carbonyl, and carboxyl). The weight loss in the temperature range 648-1163 K can be attributed to decomposition of sulfonated groups. [117] The degradation of Amberlyst®15 proceeds in three steps: dehydration at 403 K, desulfonation at 508–603 K and oxidation of polymer at 603–828 K, representing a weight loss of 60.7 % at 873 K. These results suggest that the (GO)R_A-S is more thermally stable than the reference catalyst Amberlyst® 15, which allows its use in acid reactions at temperatures in which the A-15 can not be used.

8. Conclusion

The graphene oxide was obtained by the modified Hummers method and, subsequently, a chemical reduction was carried out by means of three different routes: i) reduction with hydrazine, ii) with Zn/HCl and iii) reduction with L-ascorbic acid. The results of these processes showed different C/O ratio on the graphene oxide surface. Finally, the reduced graphene oxides were subjected to functionalization. The sulfonation using diazotization is an easy and effective route to functionalize the reduced graphene oxide, since it generates a homogeneous dispersion in the carbon skeleton. The three solids obtained were evaluated in the etherification with glycerol with *tert*-butyl alcohol, finding very similar conversions of glycerol between these catalysts and that were higher than those obtained with Amberlyst® 15, which is the reference catalyst. In the same way, the catalysts showed a different selectivity at the end of the reaction, depending on the amount of oxygen groups that remain on the surface of the graphene oxide. This led us to conclude that the hydrophobic/hydrophilic balance is very important to achieve the best results with this type of catalyst. Regarding recyclability, these catalysts have been shown to be stable and easily regenerable, converting them into efficient solids in acid reactions where they involve the formation of water as a by-product, such as the etherification of glycerol with *tert*-butyl alcohol.

References

1. Pierson, H. O., 2 - The Element Carbon. In *Handbook of Carbon, Graphite, Diamonds and Fullerenes*, Pierson, H. O., Ed. William Andrew Publishing: Oxford, 1993; pp 11-42.

2. Carter, C. B.; Norton, M. G., *Ceramic Materials*. Springer-Verlag New York: 2013; p XXXIII, 766.

3. Hirsch, A., The era of carbon allotropes. *Nature Materials* **2010,** *9*, 868.

4. Kroto, H. W.; Heath, J. R.; O'Brien, S. C.; Curl, R. F.; Smalley, R. E., C60: Buckminsterfullerene. *Nature* **1985,** *318*, 162.

5. Iijima, S., Helical microtubules of graphitic carbon. *Nature* **1991,** *354*, 56.

6. Novoselov, K. S.; Geim, A. K.; Morozov, S. V.; Jiang, D.; Katsnelson, M. I.; Grigorieva, I. V.; Dubonos, S. V.; Firsov, A. A., Two-dimensional gas of massless Dirac fermions in graphene. *Nature* **2005,** *438*, 197.

7. Shi, D.; Guo, Z.; Bedford, N., 3 - Carbon Nanotubes. In *Nanomaterials and Devices*, Shi, D.; Guo, Z.; Bedford, N., Eds. William Andrew Publishing: Oxford, 2015; pp 49-82.

8. Castro Neto, A. H.; Guinea, F.; Peres, N. M. R.; Novoselov, K. S.; Geim, A. K., The electronic properties of graphene. *Rev. Mod. Phys.* **2009,** *81* (1), 109-162.

9. Yan, R.; Qiu, S.; Tong, L.; Qian, Y., Review of progresses on clinical applications of ion selective electrodes for electrolytic ion tests: from conventional ISEs to graphene-based ISEs. *Chem. Speciation Bioavailability* **2016,** *28* (1-4), 72-77.

10. Tiwari, S. K.; Kumar, V.; Huczko, A.; Oraon, R.; Adhikari, A. D.; Nayak, G. C., Magical Allotropes of Carbon: Prospects and Applications. *Crit. Rev. Solid State Mater. Sci.* **2016,** *41* (4), 257-317.

11. Mas-Ballesté, R.; Gómez-Navarro, C.; Gómez-Herrero, J.; Zamora, F., 2D materials: to graphene and beyond. *Nanoscale* **2011,** *3* (1), 20-30.

12. Wallace, P. R., The Band Theory of Graphite. *Phys. Rev.* **1947,** *71* (9), 622-634.

13. McClure, J. W., Diamagnetism of Graphite. *Phys. Rev.* **1956,** *104* (3), 666-671.

14. Semenoff, G. W., Condensed-Matter Simulation of a Three-Dimensional Anomaly. *Phys. Rev. Lett.* **1984,** *53* (26), 2449-2452.

15. Peierls, R., Bemerkungen über umwandlungstemperaturen. *J Helv. Phys. Acta* **1934,** *7* (81-83), 158.

16. Peierls, R., Quelques proprietes typiques des corpses solides. *J Ann. IH Poincare* **1935,** *5*, 177-222.

17. Landau, L. D.; Lifshitz, E. M.; Pitaevskii, L., Statistical physics, part I. pergamon, Oxford: 1980.

18. Born, M.; Huang, K., *Dynamical theory of crystal lattices*. Clarendon press: 1954.

19. Mermin, N. D.; Wagner, H., Absence of Ferromagnetism or Antiferromagnetism in One- or Two-Dimensional Isotropic Heisenberg Models. *Phys. Rev. Lett.* **1966,** *17* (22), 1133-1136.

20. Lee, G.-H.; Yu, Y.-J.; Cui, X.; Petrone, N.; Lee, C.-H.; Choi, M. S.; Lee, D.-Y.; Lee, C.; Yoo, W. J.; Watanabe, K.; Taniguchi, T.; Nuckolls, C.; Kim, P.; Hone, J., Flexible and Transparent MoS2 Field-Effect Transistors on Hexagonal Boron Nitride-Graphene Heterostructures. *ACS Nano* **2013,** *7* (9), 7931-7936.

21. Novoselov, K. S.; Jiang, D.; Schedin, F.; Booth, T. J.; Khotkevich, V. V.; Morozov, S. V.; Geim, A. K., Two-dimensional atomic crystals. *Proc. Natl. Acad. Sci. U. S. A.* **2005,** *102* (30), 10451.

22. Zhang, Y.; Tan, Y.-W.; Stormer, H. L.; Kim, P., Experimental observation of the quantum Hall effect and Berry's phase in graphene. *Nature* **2005,** *438*, 201.

23. Stankovich, S.; Dikin, D. A.; Dommett, G. H. B.; Kohlhaas, K. M.; Zimney, E. J.; Stach, E. A.; Piner, R. D.; Nguyen, S. T.; Ruoff, R. S., Graphene-based composite materials. *Nature* **2006,** *442*, 282.

24. Geim, A. K.; Novoselov, K. S., The rise of graphene. In *Nanoscience and Technology*, Co-Published with Macmillan Publishers Ltd, UK: 2009; pp 11-19.

25. Mermin, N. D., Crystalline Order in Two Dimensions. *Phys. Rev.* **1968,** *176* (1), 250-254.

26. Meyer, J. C.; Geim, A. K.; Katsnelson, M. I.; Novoselov, K. S.; Booth, T. J.; Roth, S., The structure of suspended graphene sheets. *Nature* **2007,** *446*, 60.

27. David, N.; Tsvi, P.; Steven, W., *Statistical mechanics of membranes and surfaces*. World Scientific: 2004.

28. Schafhaeutl, C., Ueber die Verbindungen des Kohlenstoffes mit Silicium, Eisen und anderen Metallen, welche die verschiedenen Gallungen von Roheisen, Stahl und Schmiedeeisen bilden. *J. prakt. Chem.* **1840,** *21* (1), 129-157.

29. Brodie Benjamin, C., XIII. On the atomic weight of graphite. *Philos. Trans. R. Soc. Lond., B, Biol. Sci.* **1859,** *149*, 249-259.

30. Staudenmaier, L., Verfahren zur Darstellung der Graphitsäure. *Berichte der deutschen chemischen Gesellschaft* **1899,** *32* (2), 1394-1399.

31. Hummers, W. S.; Offeman, R. E., Preparation of Graphitic Oxide. *J. Am. Chem. Soc.* **1958,** *80* (6), 1339-1339.

32. Boehm, H. P.; Clauss, A.; Fischer, G. O.; Hofmann, U., Dünnste Kohlenstoff-Folien. In *Zeitschrift für Naturforschung B*, 1962; Vol. 17, p 150.

33. Boehm, H. P.; Clauss, A.; Fischer, G. O.; Hofmann, U., Das Adsorptionsverhalten sehr dünner Kohlenstoff-Folien. *Z. Anorg. Allg. Chem.* **1962,** *316* (3-4), 119-127.

34. Wick, P.; Louw-Gaume, A. E.; Kucki, M.; Krug, H. F.; Kostarelos, K.; Fadeel, B.; Dawson, K. A.; Salvati, A.; Vázquez, E.; Ballerini, L.; Tretiach, M.; Benfenati, F.; Flahaut, E.; Gauthier, L.; Prato, M.; Bianco, A., Classification Framework for Graphene-Based Materials. *Angew. Chem. Int. Ed.* **2014,** *53* (30), 7714-7718.

35. Novoselov, K. S., Graphene: Materials in the Flatland (Nobel Lecture). *Angew. Chem. Int. Ed.* **2011,** *50* (31), 6986-7002.

36. Palermo, V., Not a molecule, not a polymer, not a substrate… the many faces of graphene as a chemical platform. *Chem. Commun.* **2013,** *49* (28), 2848-2857.

37. Meric, I.; Han, M. Y.; Young, A. F.; Ozyilmaz, B.; Kim, P.; Shepard, K. L., Current saturation in zero-bandgap, top-gated graphene field-effect transistors. *Nat. Nanotech.* **2008,** *3*, 654.

38. Balandin, A. A.; Ghosh, S.; Bao, W.; Calizo, I.; Teweldebrhan, D.; Miao, F.; Lau, C. N., Superior Thermal Conductivity of Single-Layer Graphene. *Nano Lett.* **2008,** *8* (3), 902-907.

39. Loh, K. P.; Bao, Q.; Eda, G.; Chhowalla, M., Graphene oxide as a chemically tunable platform for optical applications. *Nat. Chem.* **2010,** *2*, 1015.

40. Sakhaee-Pour, A., Elastic properties of single-layered graphene sheet. *Solid State Commun.* **2009,** *149* (1), 91-95.

41. Lee, C.; Wei, X.; Kysar, J. W.; Hone, J., Measurement of the Elastic Properties and Intrinsic Strength of Monolayer Graphene. *Science* **2008,** *321* (5887), 385.

42. Bunch, J. S.; Verbridge, S. S.; Alden, J. S.; van der Zande, A. M.; Parpia, J. M.; Craighead, H. G.; McEuen, P. L., Impermeable Atomic Membranes from Graphene Sheets. *Nano Lett.* **2008,** *8* (8), 2458-2462.

43. Berry, V., Impermeability of graphene and its applications. *Carbon* **2013,** *62*, 1-10.

44. Reina, A.; Jia, X.; Ho, J.; Nezich, D.; Son, H.; Bulovic, V.; Dresselhaus, M. S.; Kong, J., Large Area, Few-Layer Graphene Films on Arbitrary Substrates by Chemical Vapor Deposition. *Nano Lett.* **2009,** *9* (1), 30-35.

45. Brydson, R. M.; Hammond, C., Generic Methodologies for Nanotechnology: Classification and Fabrication. In *Nanoscale Science and Technology*, Kelsall, R. W.; Hamley, I. W.; Geoghegan, M., Eds. John Wiley & Sons, Ltd: 2005.

46. Cao, G., *Nanostructures & nanomaterials: synthesis, properties & applications*. Imperial college press: 2004.

47. Kim, H.; Abdala, A. A.; Macosko, C. W., Graphene/Polymer Nanocomposites. *Macromolecules* **2010,** *43* (16), 6515-6530.

48. Li, D.; Kaner, R. B., Graphene-Based Materials. *Science* **2008,** *320* (5880), 1170.

49. Stankovich, S.; Piner, R. D.; Chen, X.; Wu, N.; Nguyen, S. T.; Ruoff, R. S., Stable aqueous dispersions of graphitic nanoplatelets via the reduction of exfoliated graphite oxide in the presence of poly(sodium 4-styrenesulfonate). *J. Mater. Chem.* **2006,** *16* (2), 155-158.

50. Stankovich, S.; Piner, R. D.; Nguyen, S. T.; Ruoff, R. S., Synthesis and exfoliation of isocyanate-treated graphene oxide nanoplatelets. *Carbon* **2006,** *44* (15), 3342-3347.

51. Stankovich, S.; Dikin, D. A.; Piner, R. D.; Kohlhaas, K. A.; Kleinhammes, A.; Jia, Y.; Wu, Y.; Nguyen, S. T.; Ruoff, R. S., Synthesis of graphene-based nanosheets via chemical reduction of exfoliated graphite oxide. *Carbon* **2007,** *45* (7), 1558-1565.

52. Paredes, J. I.; Villar-Rodil, S.; Martínez-Alonso, A.; Tascón, J. M. D., Graphene Oxide Dispersions in Organic Solvents. *Langmuir* **2008,** *24* (19), 10560-10564.

53. Li, D.; Müller, M. B.; Gilje, S.; Kaner, R. B.; Wallace, G. G., Processable aqueous dispersions of graphene nanosheets. *Nat. Nanotech.* **2008,** *3*, 101.

54. Li, J.; Zeng, X.; Ren, T.; van der Heide, E., The Preparation of Graphene Oxide and Its Derivatives and Their Application in Bio-Tribological Systems. *Lubricants* **2014,** *2* (3).

55. Szabó, T.; Berkesi, O.; Forgó, P.; Josepovits, K.; Sanakis, Y.; Petridis, D.; Dékány, I. J. C. o. m., Evolution of surface functional groups in a series of progressively oxidized graphite oxides. *Chem. Mater.* **2006,** *18* (11), 2740-2749.

56. He, H.; Klinowski, J.; Forster, M.; Lerf, A., A new structural model for graphite oxide. *Chem. Phys. Lett.* **1998,** *287* (1), 53-56.

57. Park, S.; Ruoff, R. S., Chemical methods for the production of graphenes. *Nat. Nanotech.* **2009,** *4*, 217.

58. Shin, H.-J.; Kim, K. K.; Benayad, A.; Yoon, S.-M.; Park, H. K.; Jung, I.-S.; Jin, M. H.; Jeong, H.-K.; Kim, J. M.; Choi, J.-Y.; Lee, Y. H., Efficient Reduction of Graphite Oxide by Sodium Borohydride and Its Effect on Electrical Conductance. *Adv. Funct. Mater.* **2009,** *19* (12), 1987-1992.

59. Gao, W.; Alemany, L. B.; Ci, L.; Ajayan, P. M., New insights into the structure and reduction of graphite oxide. *Nat. Chem.* **2009,** *1*, 403.

60. Park, S.; An, J.; Potts, J. R.; Velamakanni, A.; Murali, S.; Ruoff, R. S., Hydrazine-reduction of graphite- and graphene oxide. *Carbon* **2011,** *49* (9), 3019-3023.

61. Robinson, J. T.; Perkins, F. K.; Snow, E. S.; Wei, Z.; Sheehan, P. E., Reduced Graphene Oxide Molecular Sensors. *Nano Lett.* **2008,** *8* (10), 3137-3140.

62. Zhu, Y.; Murali, S.; Cai, W.; Li, X.; Suk, J. W.; Potts, J. R.; Ruoff, R. S., Graphene and Graphene Oxide: Synthesis, Properties, and Applications. *Adv. Mater.* **2010,** *22* (35), 3906-3924.

63. Zhang, J.; Yang, H.; Shen, G.; Cheng, P.; Zhang, J.; Guo, S., Reduction of graphene oxide vial-ascorbic acid. *Chem. Commun.* **2010,** *46* (7), 1112-1114.

64. Fernández-Merino, M. J.; Guardia, L.; Paredes, J. I.; Villar-Rodil, S.; Solís-Fernández, P.; Martínez-Alonso, A.; Tascón, J. M. D., Vitamin C Is an Ideal Substitute for Hydrazine in the Reduction of Graphene Oxide Suspensions. *J. Phys. Chem. C.* **2010,** *114* (14), 6426-6432.

65. Li, J.; Xiao, G.; Chen, C.; Li, R.; Yan, D., Superior dispersions of reduced graphene oxide synthesized by using gallic acid as a reductant and stabilizer. *J. Mater. Chem. A* **2013,** *1* (4), 1481-1487.

66. Some, S.; Kim, Y.; Yoon, Y.; Yoo, H.; Lee, S.; Park, Y.; Lee, H., High-Quality Reduced Graphene Oxide by a Dual-Function Chemical Reduction and Healing Process. *Sci Rep.* **2013,** *3*, 1929.

67. Liu, Y.; Li, Y.; Yang, Y.; Wen, Y.; Wang, M., Reduction of Graphene Oxide by Thiourea. *J. Nanosci. Nanotechnol.* **2011,** *11* (11), 10082-10086.

68. Bose, S.; Kuila, T.; Mishra, A. K.; Kim, N. H.; Lee, J. H., Dual role of glycine as a chemical functionalizer and a reducing agent in the preparation of graphene: an environmentally friendly method. *J. Mater. Chem.* **2012,** *22* (19), 9696-9703.

69. Dey, R. S.; Hajra, S.; Sahu, R. K.; Raj, C. R.; Panigrahi, M. K., A rapid room temperature chemical route for the synthesis of graphene: metal-mediated reduction of graphene oxide. *Chem. Commun.* **2012,** *48* (12), 1787-1789.

70. Mei, X.; Ouyang, J., Ultrasonication-assisted ultrafast reduction of graphene oxide by zinc powder at room temperature. *Carbon* **2011,** *49* (15), 5389-5397.

71. Pham, V. H.; Pham, H. D.; Dang, T. T.; Hur, S. H.; Kim, E. J.; Kong, B. S.; Kim, S.; Chung, J. S., Chemical reduction of an aqueous suspension of graphene oxide by nascent hydrogen. *J. Mater. Chem.* **2012,** *22* (21), 10530-10536.

72. Compton, O. C.; Nguyen, S. T., Graphene Oxide, Highly Reduced Graphene Oxide, and Graphene: Versatile Building Blocks for Carbon-Based Materials. *Small* **2010,** *6* (6), 711-723.

73. Yeh, T.-F.; Chan, F.-F.; Hsieh, C.-T.; Teng, H., Graphite Oxide with Different Oxygenated Levels for Hydrogen and Oxygen Production from Water under Illumination: The Band Positions of Graphite Oxide. *J. Phys. Chem. C.* **2011,** *115* (45), 22587-22597.

74. Mathkar, A.; Tozier, D.; Cox, P.; Ong, P.; Galande, C.; Balakrishnan, K.; Leela Mohana Reddy, A.; Ajayan, P. M., Controlled, Stepwise Reduction and Band Gap Manipulation of Graphene Oxide. *J. Phys. Chem. Lett.* **2012,** *3* (8), 986-991.

75. Xu, C.; Yuan, R.-s.; Wang, X., Selective reduction of graphene oxide. *New Carbon Mater.* **2014,** *29* (1), 61-66.

76. Bagri, A.; Mattevi, C.; Acik, M.; Chabal, Y. J.; Chhowalla, M.; Shenoy, V. B., Structural evolution during the reduction of chemically derived graphene oxide. *Nat. Chem.* **2010,** *2*, 581.

77. Wu, D.; Zhang, F.; Liu, P.; Feng, X., Two-Dimensional Nanocomposites Based on Chemically Modified Graphene. *Chem. Eur. J.* **2011,** *17* (39), 10804-10812.

78. Dreyer, D. R.; Park, S.; Bielawski, C. W.; Ruoff, R. S., The chemistry of graphene oxide. *Chem. Soc. Rev.* **2010,** *39* (1), 228-240.

79. Loh, K. P.; Bao, Q.; Ang, P. K.; Yang, J., The chemistry of graphene. *J. Mater. Chem.* **2010,** *20* (12), 2277-2289.

80. Pyun, J., Graphene Oxide as Catalyst: Application of Carbon Materials beyond Nanotechnology. *Angew. Chem. Int. Ed.* **2010,** *50* (1), 46-48.

81. Dreyer, D. R.; Jia, H.-P.; Bielawski, C. W., Graphene Oxide: A Convenient Carbocatalyst for Facilitating Oxidation and Hydration Reactions. *Angew. Chem. Int. Ed.* **2010,** *49* (38), 6813-6816.

82. Su, C.; Acik, M.; Takai, K.; Lu, J.; Hao, S.-j.; Zheng, Y.; Wu, P.; Bao, Q.; Enoki, T.; Chabal, Y. J.; Ping Loh, K., Probing the catalytic activity of porous graphene oxide and the origin of this behaviour. *Nat. Commun.* **2012,** *3*, 1298.

83. Dhakshinamoorthy, A.; Alvaro, M.; Puche, M.; Fornes, V.; Garcia, H., Graphene Oxide as Catalyst for the Acetalization of Aldehydes at Room Temperature. *ChemCatChem* **2012,** *4* (12), 2026-2030.

84. Dhakshinamoorthy, A.; Alvaro, M.; Concepción, P.; Fornés, V.; Garcia, H., Graphene oxide as an acid catalyst for the room temperature ring opening of epoxides. *Chem. Commun.* **2012,** *48* (44), 5443-5445.

85. Zhu, S.; Chen, C.; Xue, Y.; Wu, J.; Wang, J.; Fan, W., Graphene Oxide: An Efficient Acid Catalyst for Alcoholysis and Esterification Reactions. *ChemCatChem* **2014,** *6* (11), 3080-3083.

86. Gao, X.; Zhu, S.; Li, Y., Graphene oxide as a facile solid acid catalyst for the production of bioadditives from glycerol esterification. *Catal. Commun.* **2015,** *62*, 48-51.

87. Liu, F.; Sun, J.; Zhu, L.; Meng, X.; Qi, C.; Xiao, F.-S., Sulfated graphene as an efficient solid catalyst for acid-catalyzed liquid reactions. *J. Mater. Chem.* **2012,** *22* (12), 5495-5502.

88. Upare, P. P.; Yoon, J.-W.; Kim, M. Y.; Kang, H.-Y.; Hwang, D. W.; Hwang, Y. K.; Kung, H. H.; Chang, J.-S., Chemical conversion of biomass-derived hexose sugars to levulinic acid over sulfonic acid-functionalized graphene oxide catalysts. *Green Chem.* **2013,** *15* (10), 2935-2943.

89. Ji, J.; Zhang, G.; Chen, H.; Wang, S.; Zhang, G.; Zhang, F.; Fan, X., Sulfonated graphene as water-tolerant solid acid catalyst. *Chem. Sci.* **2011,** *2* (3), 484-487.

90. Kovtyukhova, N. I.; Ollivier, P. J.; Martin, B. R.; Mallouk, T. E.; Chizhik, S. A.; Buzaneva, E. V.; Gorchinskiy, A. D., Layer-by-Layer Assembly of Ultrathin Composite Films from Micron-Sized Graphite Oxide Sheets and Polycations. *Chem. Mater.* **1999,** *11* (3), 771-778.

91. Oger, N.; Lin, Y. F.; Labrugère, C.; Le Grognec, E.; Rataboul, F.; Felpin, F.-X., Practical and scalable synthesis of sulfonated graphene. *Carbon* **2016,** *96*, 342-350.

92. Quitain, A. T.; Sumigawa, Y.; Mission, E. G.; Sasaki, M.; Assabumrungrat, S.; Kida, T., Graphene Oxide and Microwave Synergism for Efficient Esterification of Fatty Acids. *Energy Fuels* **2018,** *32* (3), 3599-3607.

93. Nakajima, K.; Hara, M., Amorphous Carbon with SO3H Groups as a Solid Brønsted Acid Catalyst. *ACS Catal.* **2012,** *2* (7), 1296-1304.

94. Liu, X. Y.; Huang, M.; Ma, H. L.; Zhang, Z. Q.; Gao, J. M.; Zhu, Y. L.; Han, X. J.; Guo, X. Y., Preparation of a carbon-based solid acid catalyst by sulfonating activated carbon in a chemical reduction process. *Molecules* **2010,** *15* (10), 7188-96.

95. Kunin, R.; Meitzner, E. A.; Oline, J. A.; Fisher, S. A.; Frisch, N., Characterization of Amberlyst 15. Macroreticular Sulfonic Acid Cation Exchange Resin. *I&EC Product Research and Development* **1962,** *1* (2), 140-144.

96. Antunes, M. M.; Russo, P. A.; Wiper, P. V.; Veiga, J. M.; Pillinger, M.; Mafra, L.; Evtuguin, D. V.; Pinna, N.; Valente, A. A., Sulfonated graphene oxide as effective catalyst for conversion of 5-(hydroxymethyl)-2-furfural into biofuels. *ChemSusChem* **2014,** *7* (3), 804-12.

97. Whitby, R. L.; Gun'ko, V. M.; Korobeinyk, A.; Busquets, R.; Cundy, A. B.; Laszlo, K.; Skubiszewska-Zieba, J.; Leboda, R.; Tombacz, E.; Toth, I. Y.; Kovacs, K.; Mikhalovsky, S. V., Driving forces of conformational changes in single-layer graphene oxide. *ACS Nano* **2012,** *6* (5), 3967-73.

98. Manoj, B.; Kunjomana, A., Study of stacking structure of amorphous carbon by X-ray diffraction technique. *Int. J. Electrochem. Sci.* **2012,** *7* (4), 3127-3134.

99. Saito, R.; Hofmann, M.; Dresselhaus, G.; Jorio, A.; Dresselhaus, M. S., Raman spectroscopy of graphene and carbon nanotubes. *Advances in Physics* **2011,** *60* (3), 413-550.

100. Kudin, K. N.; Ozbas, B.; Schniepp, H. C.; Prud'homme, R. K.; Aksay, I. A.; Car, R., Raman Spectra of Graphite Oxide and Functionalized Graphene Sheets. *Nano Lett.* **2008,** *8* (1), 36-41.

101. Wilson, N. R.; Pandey, P. A.; Beanland, R.; Young, R. J.; Kinloch, I. A.; Gong, L.; Liu, Z.; Suenaga, K.; Rourke, J. P.; York, S. J.; Sloan, J., Graphene Oxide: Structural Analysis and Application as a Highly Transparent Support for Electron Microscopy. *ACS Nano* **2009,** *3* (9), 2547-2556.

102. Kang, H.; Kulkarni, A.; Stankovich, S.; Ruoff, R. S.; Baik, S., Restoring electrical conductivity of dielectrophoretically assembled graphite oxide sheets by thermal and chemical reduction techniques. *Carbon* **2009,** *47* (6), 1520-1525.

103. Ferrari, A. C.; Robertson, J., Interpretation of Raman spectra of disordered and amorphous carbon. *Physical Review B* **2000,** *61* (20), 14095-14107.

104. Wang, G.; Wang, B.; Park, J.; Yang, J.; Shen, X.; Yao, J., Synthesis of enhanced hydrophilic and hydrophobic graphene oxide nanosheets by a solvothermal method. *Carbon* **2009,** *47* (1), 68-72.

105. Eigler, S.; Hirsch, A., Chemistry with Graphene and Graphene Oxide—Challenges for Synthetic Chemists. *Angew. Chem. Int. Ed.* **2014,** *53* (30), 7720-7738.

106. Hontoria-Lucas, C.; López-Peinado, A. J.; López-González, J. d. D.; Rojas-Cervantes, M. L.; Martín-Aranda, R. M., Study of oxygen-containing groups in a series of graphite oxides: Physical and chemical characterization. *Carbon* **1995,** *33* (11), 1585-1592.

107. Ji, J.; Zhang, G.; Chen, H.; Wang, S.; Zhang, G.; Zhang, F.; Fan, X., Sulfonated graphene as water-tolerant solid acid catalyst. *Chem. Sci.* **2011,** *2* (3), 484-487.

108. Nakhate, A. V.; Yadav, G. D., Synthesis and Characterization of Sulfonated Carbon-Based Graphene Oxide Monolith by Solvothermal Carbonization for Esterification and Unsymmetrical Ether Formation. *ACS Sustainable Chem. Eng.* **2016,** *4* (4), 1963-1973.

109. Cordoba, M.; Miranda, C.; Lederhos, C.; Coloma-Pascual, F.; Ardila, A.; Fuentes, G.; Pouilloux, Y.; Ramírez, A., Catalytic Performance of Co3O4 on Different Activated Carbon Supports in the Benzyl Alcohol Oxidation. *Catalysts* **2017,** *7* (12), 384.

110. Miranda, C.; Urresta, J.; Cruchade, H.; Tran, A.; Benghalem, M.; Astafan, A.; Gaudin, P.; Daou, T. J.; Ramírez, A.; Pouilloux, Y.; Sachse, A.; Pinard, L., Exploring the impact of zeolite porous voids in liquid phase reactions: The case of glycerol etherification by tert-butyl alcohol. *J. Catal.* **2018,** *365*, 249-260.

111. Frusteri, F.; Arena, F.; Bonura, G.; Cannilla, C.; Spadaro, L.; Di Blasi, O., Catalytic etherification of glycerol by tert-butyl alcohol to produce oxygenated additives for diesel fuel. *Appl. Catal., A* **2009,** *367* (1-2), 77-83.

112. Kiatkittipong, W.; Intaracharoen, P.; Laosiripojana, N.; Chaisuk, C.; Praserthdam, P.; Assabumrungrat, S., Glycerol ethers synthesis from glycerol etherification with tert-butyl alcohol in reactive distillation. *Comput. Chem. Eng.* **2011,** *35* (10), 2034-2043.

113. Klepáčová, K.; Mravec, D.; Bajus, M., tert-Butylation of glycerol catalysed by ion-exchange resins. *Appl. Catal., A* **2005,** *294* (2), 141-147.

114. Xu, M.; Lunsford, J. H.; Goodman, D. W.; Bhattacharyya, A., Synthesis of dimethyl ether (DME) from methanol over solid-acid catalysts. *Appl. Catal., A* **1997,** *149* (2), 289-301.

115. Veiga, P. M.; Gomes, A. C. L.; Veloso, C. O.; Henriques, C. A., Acid zeolites for glycerol etherification with ethyl alcohol: Catalytic activity and catalyst properties. *Appl. Catal., A* **2017,** *548* (Supplement C), 2-15.

116. González, M. D.; Cesteros, Y.; Salagre, P., Establishing the role of Brønsted acidity and porosity for the catalytic etherification of glycerol with tert-butanol by modifying zeolites. *Appl. Catal., A* **2013,** *450*, 178-188.

117. Mirza-Aghayan, M.; Tavana, M. M.; Boukherroub, R., Sulfonated reduced graphene oxide as a highly efficient catalyst for direct amidation of carboxylic acids with amines using ultrasonic irradiation. *Ultrason. Sonochem.* **2016,** *29*, 371-9.

Chapter 5:

Acid catalysts in the etherification of glycerol with *iso*amyl alcohol

In this last chapter, we briefly describe the preliminary results obtained from the etherification of glycerol with isoamyl alcohol using acid catalysts that were previously evaluated in the etherification of glycerol with *tert*-butyl alcohol, such as Amberlyst® 15, sulfonated reduced graphene oxide and beta zeolite (CP-811-25L). Isoamyl alcohol was selected in this research, motivated by the search for new routes to take advantage of fusel oil, which are currently very limited in the local context, despite the fact that the bioethanol production industry in Colombia has had a strong growth in recent years.

1. Fusel oil

Within the process of obtaining bioethanol from the fermentation of first-generation raw materials such as sugar and starch or the second generation such as lignocellulosic biomass, it is possible to generate other light alcohols that remain as waste when the distillation is carried out and purification of bioethanol. This fraction, which consists of a mixture of alcohols from C2 to C5, is what is called fusel oil. The percentage of composition of alcohols present in the fraction can vary between 50 and 70% depending on the raw material used and the industry that carries out the distillation. [1] From this mixture of alcohols, isoamyl alcohol can be present up to 85%, becoming in the most abundant alcohol. [2] This alcohol has the molecular formula $C_5H_{12}O$, it is a colorless liquid and the main applications are in the field of photography and as a precursor of the esters and derivatives of isoamyl. [3]

2. Etherification of glycerol with *iso*amyl alcohol

According to a thorough review of the literature, there are no reports directly addressing the etherification of glycerol with *iso*amyl alcohol. With this panorama, it was decided to design an experimental development, where the best catalysts of the work done with etherification using *tert*-butyl alcohol were selected. Likewise, it started from previously optimized conditions, such as the molar ratio, temperature and agitation. The reaction was carried out in the same reactor in which the etherification was carried out with *tert*-butyl

alcohol (described in the previous chapters). When satisfactory results were not obtained after analyzing by gas chromatography, it was decided to vary the conditions to try to generate a glycerol conversion to ethers. In a preliminary way, Table V.1 shows qualitatively after each test, the identification of the product of interest that would be glycerol *iso*amyl ether (GIAE).

Table V. 1 Identification of GIAE in the reactions with Amberlyst® 15, sulfonated reduced graphene oxide and beta zeolite as catalysts

Catalyst	Temperature (K)	Time (h)	GIAE*
A-15	363	24	ND
	387	24	ND
	387	48	ND
	387	72	ND
	387	96	ND
(GO)R_A-S	387	72	ND
	413	72	ND
	453	72	ND
(*$BEA_{NC}^{12.5}$)	413	72	ND
	508	72	D

* ND: non-detected; D: detected

According to the results obtained under the conditions studied, it is possible to observe that only the etherification of glycerol with *iso*amyl alcohol occurs at high temperatures with zeolite beta, where in addition to this product, a cracking of the reactants was detected by gas chromatography mass, as well as the generation of the product di-*iso*amyl ether (DAE). This product was also detected in the reaction performed, at lower temperatures with the other catalysts. This observation allowed, in the first instance, also consider the possibility of investigating the etherification of isoamyl alcohol.

3. Etherification of *iso*amyl alcohol

Obtaining DAE of the etherification of the same *iso*amyl alcohol is a reaction that requires high temperatures to observe activity. [4] Tejero *et al*. studied the etherification of *n*-pentyl

alcohol to obtain di-*n*-pentyl ether (DNPE) using zeolites (beta, HY, HZSM-5 and MOR) as catalysts. The results showed that the best conversion (47.9%) was obtained at 453 K with the zeolite beta (SiO_2/Al_2O_3 = 25). Lower reaction temperatures lead to a lower conversion. In this work they also studied the reaction kinetics, finding that two molecules of alcohol adsorbed on a single centre react to give the ether and water, adsorbed each one on a single centre as well, and the surface reaction being the rate-limiting step. [5] However, it is possible to obtain DAE at lower temperatures, but from the etherification of *iso*amyl alcohol with olefins, which in turn contain a tertiary carbon in their structure. In this sense, Cataluña and co-workers, designed a system to obtain di-amyl ethers of the reaction between *iso*amyl alcohol and C5 alkenes. [6] The maximum conversion was 48% when they attributed this value to the equilibrium limit. In this work we also studied some properties of interest for the use of DAE as an additive for fuels, concluding that they can potentially be applied in aviation fuel formulations.

According to the results of our research, it is possible to generate DAE with Amberlyst® 15, in addition to the sulfonated reduced graphene oxide and the zeolite beta at 387 K and with a low catalyst load (8%). Table V.2 shows the conversion results.

Table V. 2 *Iso*amyl alcohol conversion using Amberlyst® 15, sulfonated reduced graphene oxide and beta zeolite as catalysts.

Catalyst	*Iso*amyl alcohol conversion (%)
A-15	17
(GO)R_A-S	14
(*$BEA^{12.5}_{NC}$)	8

Reaction time =72 h, catalyst load= 3%, stirring=1200 rpm, temperature reaction= 387 K

These preliminary results could serve as a basis for deepening this reaction, considering the great applicability of the product that is generated, likewise it could provide an opportunity for the valorization of fusel oil.

References

1. Urresta, J. D., Deshidratacion de los alcoholes presentes en el aceite fusel y su conversión en alquenos empleando una zeolita tipo HZSM-5 *Inycompe* **2014,** *16*, 79-90.

2. Ruiz, F. S., *Cultivo de la Caña de Azúcar*. Euned: 1995.

3. Engineers, N. B. C., *Industrial Alcohol Technology Handbook*. ASIA PACIFIC BUSINESS PRESS Inc.: 2010.

4. Nel, R. J. J.; de Klerk, A., Dehydration of C5−C12 Linear 1-Alcohols over η-Alumina to Fuel Ethers. *Ind. Eng. Chem. Res.* **2009,** *48* (11), 5230-5238.

5. Tejero, J.; Fité, C.; Iborra, M.; Izquierdo, J. F.; Cunill, F.; Bringué, R., Liquid-phase dehydrocondensation of 1-pentanol to di-n-pentyl ether (DNPE) over medium and large pore acidic zeolites. *Microporous Mesoporous Mater.* **2009,** *117* (3), 650-660.

6. Cataluña, R.; Shah, Z.; Venturi, V.; Caetano, N. R.; da Silva, B. P.; Azevedo, C. M. N.; da Silva, R.; Suarez, P. A. Z.; Oliveira, L. P., Production process of di-amyl ether and its use as an additive in the formulation of aviation fuels. *Fuel* **2018,** *228*, 226-233.

General Conclusions

The etherification of glycerol with *tert*-butyl alcohol is a reaction that can be promoted by Brønsted acid catalysts of heterogeneous type. In turn, the products of this reaction are generated by successive routes, where mono *tert*-butyl ether of glycerol is the most likely, followed by the di and finally the tri-*tert*-butyl ether of glycerol, which is not obtained in large quantities.

The study with zeolites showed that the catalytic activity depends on the size of the crystal and the size of the pores; sizes less than 100 nm - where there are no diffusion limitations-, zeolite Beta shows a dependence of the catalytic activity with the concentration of acid sites. While, with respect to the size of the pores, zeolites with large confinement voids favor successive etherification (such as Faujasite), although desorption of the products can be prevented.

The use of non-porous catalysts in this reaction, such as sulfonated reduced graphene oxide, also shows good catalytic results. For this type of catalysts, the glycerol conversions were higher than those obtained with Amberlyst® 15, which has been established as a reference catalyst for this reaction. The amount of sulphonic groups (acid concentration) and the remaining oxygenated groups on the surface after reduction, act synergistically; where the sulphonic groups are directly responsible for the etherification reaction and the oxygenated groups generate a suitable hydrophilic/hydrophobic equilibrium which allows successive etherification and helps to obtain di and tri-*tert*-butyl ethers of glycerol.

The reaction mechanism also depends on the catalyst used. The zeolites promote etherification by an Eley-Rideal mechanism and the sulfonated reduced graphene oxide does so by a Langmuir-Hinshelwood mechanism. The differences of these mechanisms in the same reaction are mainly between the probable distances of the adsorbates, where for

the zeolites it is greater, while for the sulfonated reduced graphene oxide, the adsorbates are closer thanks to the presence of oxygenated groups.

With respect to the etherification of glycerol using *iso*amyl alcohol, this is a more complex reaction than etherification with *tert*-butyl alcohol, because the primary alcohol is more difficult to activate. The preliminary results of this reaction showed that the self-esterification of *iso*amyl alcohol favors the etherification with glycerol. The results could be explained by the low solubility that occurs between these two alcohols. These results open a possibility for the valuation of fusel oil, where the product of self-etherification (*iso*amyl ether) is a potential candidate to be used in aviation fuel formulations.

Perspectives

The research that uses acid zeolites in the etherification of glycerol with *tert*-butyl alcohol, ratifies and complements some observations and statements previously made in the literature. The finding that the use of zeolites with large pore sizes and small glass sizes makes it possible to subsequently explore other mesoporous nanometric materials to improve catalytic activity.

On the other hand, the surprising results with reduced sulfonated graphene oxide in this reaction have opened the possibility that the use of carbocatalysts in the etherification of glycerol with *tert*-butyl alcohol could be extended. Recently it has been reported in the literature that it is possible to obtain 3D graphene, that is, it has a porous structure. The combination of pores, functionalization and an adequate hydrophilic/hydrophobic balance make these systems serious candidates for research.

With respect to the etherification of the *iso*amyl alcohol, subsequent studies can be carried out with suitable reaction sets that allow to generate a greater conversion of this alcohol and in this way provide a future use of the fusel oil.

Annex A

Synthesis of γ-Al_2O_3: γ-Al_2O_3 was prepared from aluminium nitrate nonahydrate ($Al(NO_3)_3 \cdot 9H_2O$). 7.36 g of $Al(NO_3)_3 \cdot 9H_2O$ were dissolved in 50 mL deionized water with continuous stirring at 333 K for 2 h. When the solution was heated to 373 K and 13.6 mL of ammonia solution (28%) was added dropwise. After the addition of the ammonia solution was completed stirring continued for a further 12 h at 303 K. The precipitate obtained was filtered, washed with distillated water, and dried at 393 K for 12 h. The solid was calcined at 823 K for 5 h.

Synthesis of SiO_2-Al_2O_3 [100]: Aluminosilicate was prepared by co-precipitation. Aluminium nitrate nonahydrate ($Al(NO_3)_3 \cdot 9H_2O$) and tetraethylorthosilicate (TEOS, Sigma-Aldrich) were used as the starting materials. 18 g of $Al(NO_3)_3 \cdot 9H_2O$ were first dissolved in absolute ethanol, then 0.5 g of TEOS were added and stirred vigorously for 3 h. After the solution was stirred, 25 wt% NH_4OH aqueous solution (100 ml) was added rapidly with vigorous stirring to obtain a precipitate. The precipitates were immediately dried using an evaporator at 333 K for 2 h, then at 373 K for 15 h in an oven. The resultant solid was calcined at 573 K for 4 h to obtain the aluminosilicate.

d(0.4/358)-a-$(\mathbf{MOR})_{\mathbf{SC}}^{\mathbf{10}}$ catalyst [37]: The zeolite used as a starting material was a commercial protonic mordenite (MOR, Süd chemie) with a molar ratio Si/Al of 10. Briefly, 10 g of MOR were stirred at 400 rpm in 300 ml alkaline solution (0.4 M) at 358 K for 2 h. Then, zeolite suspension was centrifuged (6000 rpm) after being cooled down in ice–water mixture. The decantation of the liquid was followed by re-suspension with demineralized water. This procedure was repeated until pH was 7. Samples were subsequently treated with 0.5 M of HCl under stirring at 303 K for 10 min using the proportion of 10 ml per gram of sample. All samples were converted into their correspondent protonic form by three consecutive exchanges with 2 M, NH_4NO_3 using the proportion: 20 cm^3/g of zeolite. The exchange was

carried out at 363 K for 4 h. After a careful wash up to pH 7, solid was calcined under air flow (100 ml min^{-1}/g of zeolite) at 823 K for 5 h.

Synthesis of *BEA-type zeolite micron-sized crystal [101]: The synthesis mixture was prepared by hydrolyzing tetraethylorthosilicate (TEOS) (98 wt%, Aldrich) in an aqueous solution of tetraethylammonium hydroxide (TEAOH) (35 wt% in aqueous solution, Aldrich). Then a solution made by dissolving metal aluminum (99.95%, Aldrich) in aqueous TEAOH was added and the mixture was kept under stirring until the complete evaporation of ethanol formed upon hydrolysis of TEOS. Finally, hydrofluoric acid (40 wt% in H_2O) was added. The obtained gel (composition in the Table II.3.), was hydrothermally treated at 443 K for 14 days in a Teflon lined stainless steel autoclave. After the required crystallization time, the autoclave was cooled down to room temperature. The pH of the mother liquor was in the range 8–9.5. The product was filtered and washed extensively with distilled water. Finally, the sample was calcined under air at 823 K during 5 h with a temperature ramp of 274 K per minute in order to remove the organic template.

Synthesis of *BEA-type zeolite submicron-sized crystal [101]: For the synthesis of the sub-micron-sized (SC) *BEA-type zeolite, aluminum (Al, Fluka, 99%) was mixed with tetraethylammonium hydroxide solution (TEAOH, Aldrich, 35 wt. % in H_2O) at room temperature. After, tetraethylorthosilicate (TEOS, Aldrich, 98%) was added to the initial solution and mixed until the complete evaporation of water and ethanol. To the dry gel obtained, water and hydrofluoric acid (HF, Aldrich, 40 wt. % in H_2O) were added and mixed during 4 h to room temperature. The resulting white gel (Table II.3) were transferred to an autoclave to 443 K during 14 days. Finally, the solid was filtered and washed with water, dried at 373 K during 12 h and calcined to 823 K during 5 h.

Synthesis of *BEA-type zeolite nanometer-sized crystal [102]: A precursor solution of molecular composition 0.014 Na_2O: 0.18 $(TEA)_2O$: 0.020 Al_2O_3: 1 SiO_2: 11.80 H_2O was hydrothermally treated at 368 K for 9 days in a polypropylene bottle. The chemical reagents used were aluminum isopropoxide (98 wt%, Aldrich), tetraethylammonium hydroxide

(TEAOH, 35 wt% in aqueous solution, Aldrich), sodium hydroxide (99.99 wt%, Riedel de Haën) and silica powder resulting from the lyophilization of colloidal silica (Ludox AS-40, Aldrich). The resulting milky solution of *BEA zeolite was purified by several centrifugation–dispersion cycles in distilled water (at 20 000 rpm for 30 min). In order to remove the template occluded in the porosity (tetraethylammonium), the final sample was calcined under air at 823 K during 5 h with a temperature ramp of 274 K per minute.

Synthesis of *BEA-type zeolite nano-sponge [103, 104]: The NSp sample was synthesized using a poly-quaternary ammonium surfactant denoted by $N_{4\text{-phe}}$, Figure II.14.

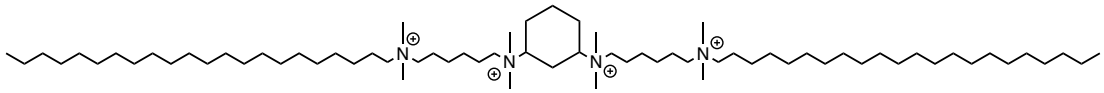


Figure II. 2 Molecular structure of gemini-type quaternary ammonium surfactant $N_{4\text{-Phe}}$ used as a structure-directing agent for the synthesis of nano-sponge (NSp) *BEA-type zeolite.

For the synthesis of poly-quaternary ammonium surfactant ($N_{4\text{-phe}}$), 8.6 g of N,N,N',N'-tetramethyle-1,6-diaminohexane (Sigma Aldrich) and 2 g of 1-bromodocosane (Sigma Aldrich) were dissolved in 100 ml acetonitrile/toluene solvent (1:1 v/v) and heated 333 K for 12 h under magnetic stirring. This solution was evaporated for a removal of solvent and then a white solid was precipitated. The solid obtained was washed with diethyl ether, filtered and dried in a vacuum oven at 323 K. Subsequently, 1.52 g of $C_{22\text{-}6\text{-}0}$ and 0.175 g of *αα*-dichloro-*p*-xylene (Sigma Aldrich) were dissolved in 13 mL chloroform and reflux over 12 h. This solution was evaporated for a removable of solvent and then the final product ($N_{4\text{-phe}}$) was precipitated. The solid was washed using diethyl ether, filtered and dried in a vacuum oven at 50 °C.

After of synthesis of surfactant, ethanol (99.9%), sodium hydroxide (99.99 wt%, Riedel de Haën), sodium aluminate (56.7 wt% Al_2O_3, 39.5 wt% Na_2O) and TEOS (98 wt%, Aldrich) were mixed to obtain a gel composition of 0.22 Na_2O: 0.05 $N_{4\text{-phe}}$: 0.025 Al_2O_3: 1 SiO_2: 4 $(ET)_2O$:

71 H_2O. The resulting gel mixture was maintained under magnetic stirring at 333 K for 6 h. The final gel was transferred to a Teflon-lined stainless-steel autoclave and heated at 413 K for 4 days under tumbling conditions at 60 rpm. After crystallization, the zeolite product was filtered, washed with distilled water and dried at 393 K. The products were calcined at 873 K for 4 h under air in order to remove the organic surfactant. The protonated form of MC, NC and NS zeolites was obtained by double ion exchange of the calcined zeolite with a 1 M NH_4NO_3 solution (liquid/solid ratio: 20 mL/g) at 353 K for 1 h and calcination in a static oven at 823 K for 5 h.

Table II. 2 Molar composition of the starting synthesis gels and thermal conditions for the preparation of micron-sized (MC), submicron-sized (SC), and nanometer-sized (NC) crystals and nanosponge (NSp)*BEA-type zeolites.

Reagents	**Catalyst**	$(*BEA)^{15}_{MC}$	$(*BEA)^{9}_{SC}$	$(*BEA)^{10}_{SC}$	$(*BEA)^{15}_{NC}$	$(*BEA)^{17}_{NSp}$
	Si	TEOS[d]	TEOS[d]	Aerosil 130	SiO_2[a]	TEOS[d]
	Al	$Al_{(s)}$	$Al_{(s)}$	$NaAlO_2$	Al(O-iPr)$_3$	$NaAlO_2$
Gel composition in molar ratio	HF	0.573	0.680	--	--	--
	Na_2O	--	--	0.020	0.014	0.220
	$(TEA)_2O$[b]	0.226	0.340	0.140	0.180	--
	$N_{4\text{-phe}}$[c]	--	--	--	--	0.050
	Al_2O_3	0.016	0.070	0.016	0.020	0.025
	SiO_2	1	1	1	1	1
	$(Et)_2O$	--	--	--	--	4.00
	H_2O	7.03	7.14	15.75	11.80	71.00
Temp.	(K)	443	443	423	368	413
Time	(days)	14	14	16	9	4

[a]Ludox AS(40) 40% in water lyophilized for 5 days. [b]TEA: $(CH_3–CH_2)N–$. [c]$N_{4\text{-Phe}}$: $C_{22}H_{45}N^+(CH_3)_2C_6H_{12}N^+(CH_3)_3(Br)^-$. [d]TEOS: $Si(OCH_2CH_3)_4$; Et: $CH_3–CH_2–OH$.

Synthesis of $(MFI)^{45}_{NSh}$ catalyst [105, 106]: The diquaternary ammonium-type surfactant used for the synthesis of MFI-type nanosheets, has as formula ($[C_{22}H_{45}\text{-}N^+(CH_3)_2\text{-}C_6H_{12}\text{-}N^+(CH_3)_2\text{-}C_6H_{13}]Br_2$), called diquat-$C_6$-$C_{22}$, Figure II.15.

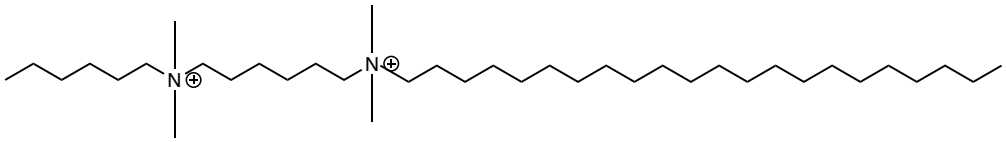


Figure II. 3 Bifunctional cationic surfactant ($C_{22\text{-}6\text{-}6}$)[106].

Diquat-C_6-C_{22} was synthesized as follows: 39.0 g of 1-bromodocosane and 172 g N,N,N′,N′-tetramethyl-1,6-diaminohexane (Sigma Aldrich) were dissolved in 1,000 ml acetonitrile/toluene mixture (1:1 vol/vol) and heated at 343 K for 10 h. After cooling to room temperature, the product was filtered, washed with diethyl ether, and dried in a vacuum oven at 323 K. 56.2 g of the product and 24.6 g of 1-bromohexane (Sigma Aldrich) were dissolved in 300 mL acetonitrile and refluxed for 10 h. After cooling to room temperature, the product was filtered, washed with diethyl ether, and dried in a vacuum oven at 323 K.

For the synthesis of the zeolite, initially, 0.24 g of sodium hydroxide (Riedel de Haen, 99%) was dissolved, at room temperature, in 7.17 g of distilled water in a 45 mL Teflon-lined stainless-steel autoclave. Subsequently, 0.73 g of diquat-C_6-C_{22} and 0.18 g of sulfuric acid (Aldrich) were then added. After homogenization, 2.13 g of TEOS was added, and a white gel with the following molar composition, 1 SiO_2: 0.3 Na_2O: 0.1 diquat-C_6–C_{22}: 0.18 H_2SO_4: 40 H_2O, was then obtained. The gel was stirred at 1000 rpm during 4 h at 333 K. Then, the mixture was heated at 383 K for 10 days under rotation (30 rpm). After synthesis, the product was recovered by filtration, washed with distilled water, and dried overnight at 373 K. The surfactant was finally removed by calcination in a muffle furnace at 823 K during 8 h in air.

Synthesis of $(\mathbf{MFI})^{\mathbf{20}}_{\mathbf{NSp}}$ catalyst [103]: MFI zeolite with nanosponge morphology was synthesized by using $C_{18}H_{37}{-}N^+(CH_3)_2{-}C_6H_{12}{-}N^+(CH_3)_2{-}C_6H_{12}{-}N^+(CH_3)_2{-}C_{18}H_{37}(Br^-)_3$ named $C_{18\text{–}6\text{–}6}C_{18}$ as organic structure-directing agent, Figure II.16.

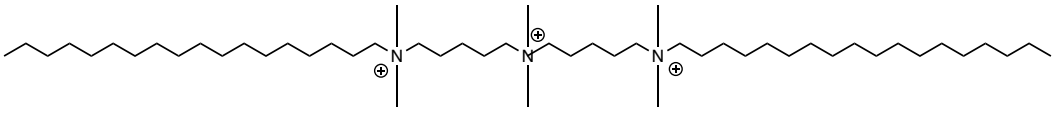
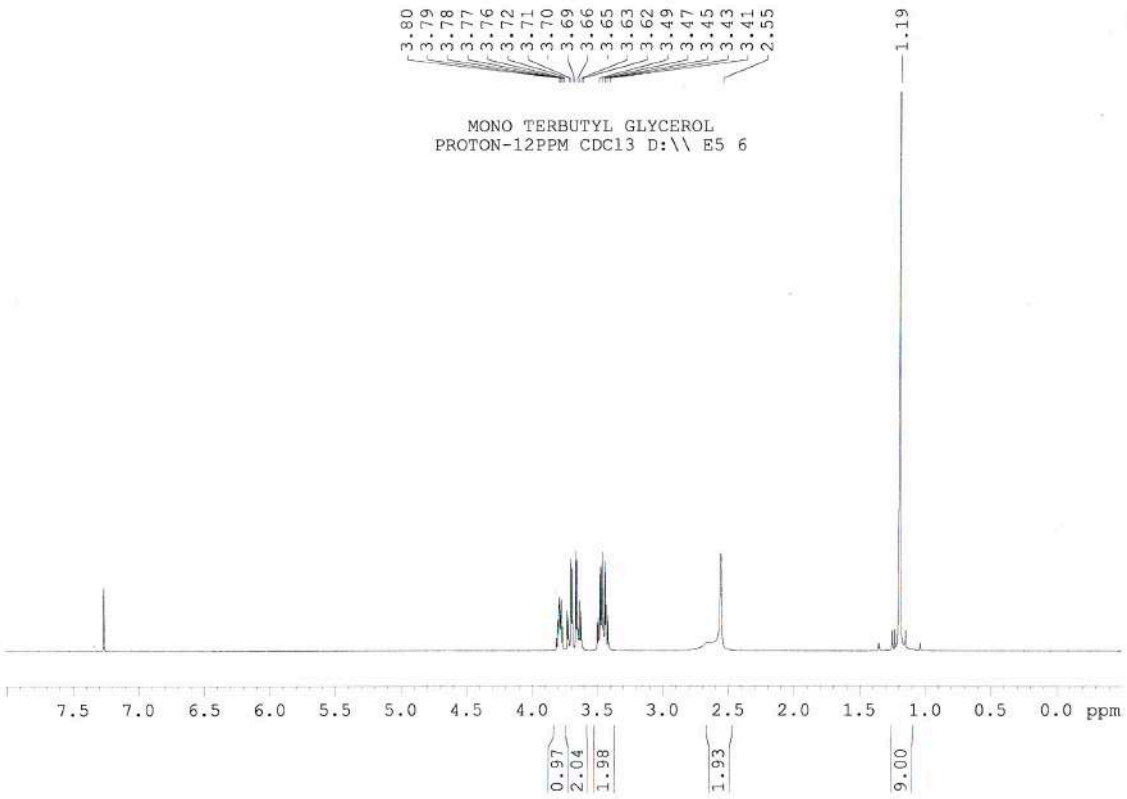


Figure II. 4 Bifunctional cationic surfactant ($C_{18-6-6}C_{18}$). Adapted from [103].

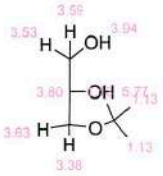
For the synthesis of $C_{18-6-6}C_{18}$ surfactant, $C_{18}H_{37}–N^{+}(CH_3)_2–C_6H_{12}–Br(Br^{-})$ and $C_{18}H_{37}–N^{+}(CH_3)_2–C_6H_{12}–N(CH_3)_2$ were prepared separately *via* organic reaction. First, 0.034 mol of N,N′–dimethyloctadecylamine (Sigma Aldrich)) and 0.34 mol of 1,6–dibromohexane (Sigma Aldrich) were dissolved in 1000 mL acetonitrile/toluene mixture (1000 wt% per total organic reactants, 1:1 v/v) and heated at 333 K for 12 h. After cooling to room temperature and solvent evaporation, solid product with the formula of $C_{18}H_{37}–N^{+}(CH_3)_2–C_6H_{12}–Br(Br^{-})$ was precipitated. This product was further filtered, washed with diethyl ether, and dried in a vacuum oven at 323 K for 2 h. Second, 0.030 mol of 1–bromooctadecane (Acros Organics) and 0.300 mol of N,N,N′,N′–tetramethyl–1,6–diaminohexane (Sigma Aldrich) were dissolved in 600 mL acetonitrile/toluene mixture (1:1 v/v) and heated at 333 K for 12 h. After quenching and purification, solid product with the formula of $C_{18}H_{37}–N^{+}(CH_3)_2–C_6H_{12}–N(CH_3)_2(Br^{-})$ was obtained. Finally, equimolar amounts of $C_{18}H_{37}–N^{+}(CH_3)_2–C_6H_{12}–Br(Br^{-})$ and $C_{18}H_{37}–N^{+}(CH_3)_2–C_6H_{12}–N(CH_3)_2(Br^{-})$ were dissolved in acetonitrile (200wt% per total organic reactants) and refluxed for 12 h. After solvent evaporation, the precipitated product was filtered and dried in a vacuum oven at 333 K to obtain the final product, the $C_{18-6-6}C_{18}$ surfactant.

For zeolite synthesis, sodium hydroxide (Riedel de Haen, 99%), sodium aluminate (56.7 wt % Al_2O_3, 39.5 wt % Na_2O), tetraethoxysilane (TEOS, Aldrich, 98%) and ethanol (99%) were dissolved in deionized water in a 45 mL Teflon-lined stainless-steel autoclave. After homogenization, $C_{18-6-6}C_{18}$ was added to set the molar composition of the gel to 100 SiO_2: 22 Na_2O: 2.5 Al_2O_3: 5 $C_{18-6-6}C_{18}$: 800 ETOH: 7100 H_2O. The gel was stirred at 1000 rpm for 6 h at 333 K, and then placed in a tumbling oven (30 rpm) at 413 K for 4 days. After synthesis, the product was recovered by filtration, washed with deionized water and dried overnight at 393 K. The $C_{18-6-6}C_{18}$ surfactant was removed by calcination at 823 K during 4 h in air.

Annex B



ChemNMR ^{1}H Estimation



Estimation quality is indicated by color: good, medium, rough

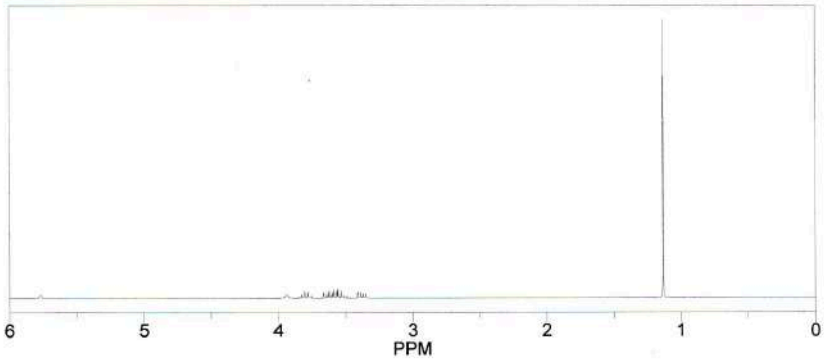
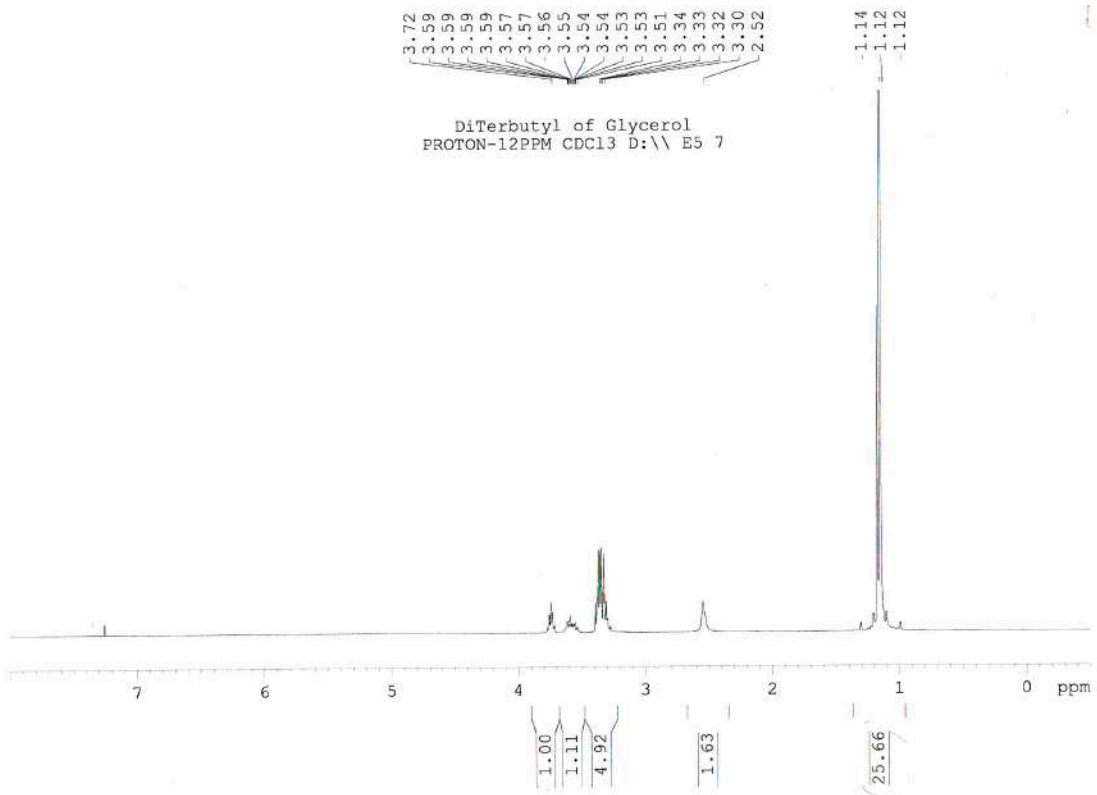


Figure B.1 3-*tert*-butoxy-1,2 propanediol NMR [1]H.



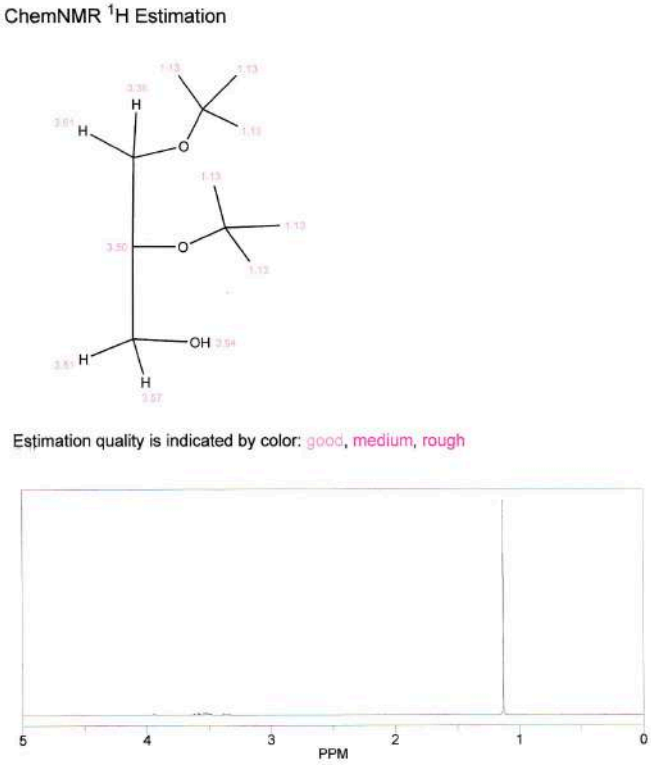
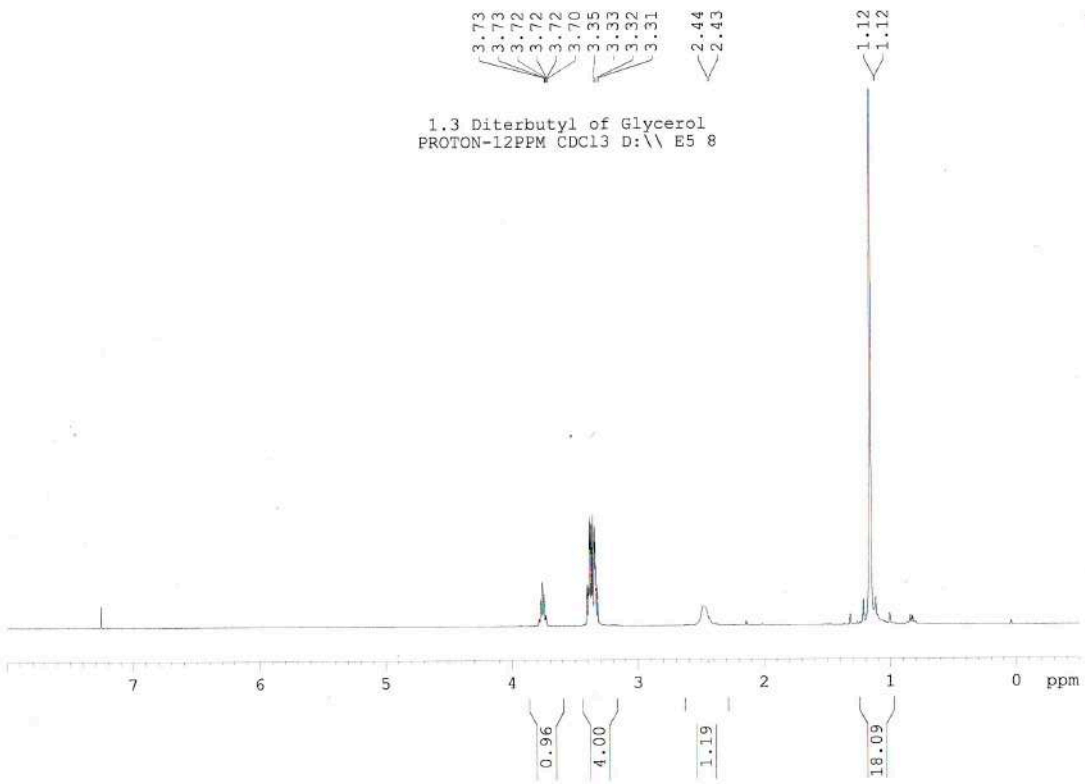
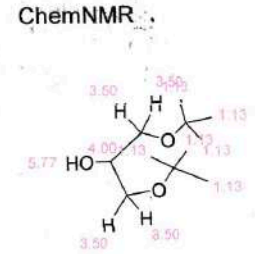


Figure B.2 2,3-di-*tert*-butoxy-1-propanol NMR [1]H.





Estimation quality is indicated by color: good, medium, rough

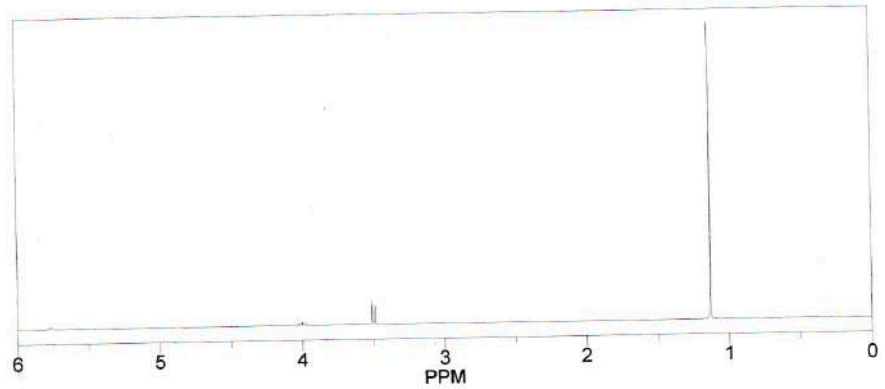


Figure B.3 1,3-di-*tert*-butoxy-2-propanol NMR ^{1}H.

Annex C

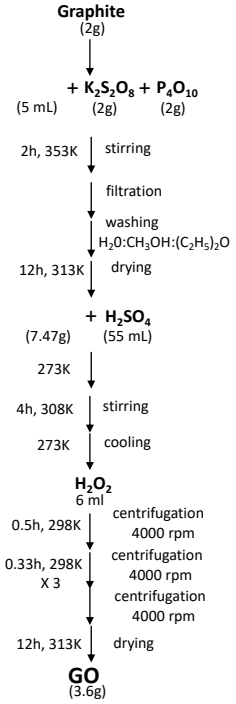


Figure C.1 Synthesis scheme of graphene oxide.

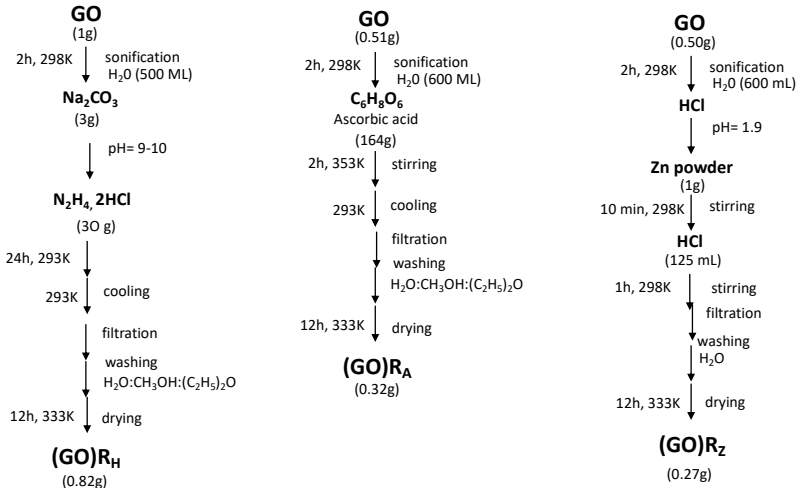


Figure C.2 Synthesis scheme of the reduction pathways.

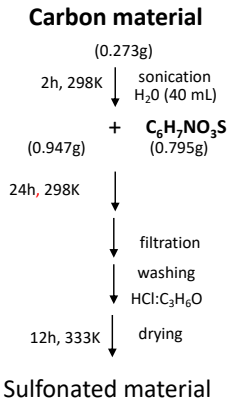


Figure C.3 Synthesis scheme of functionalized reduced graphene oxide or activated carbon.